

Department of Vascular Biology and Thrombosis Research
Medical University of Vienna

Institute of Physiology
(Head: Ao.Univ.-Prof. Dipl.-Ing. Dr. Johannes Schmid)

Precision Histology of Prostate Cancer and Pathologic Processes Implementation to Artificial Intelligence.

Master-Thesis

Master program: Biomedicine and Biotechnology
University of Veterinary Medicine Vienna

presented by
Viola Gleitsmann
(Matricula number: 1340063)

Vienna, June 2020

External Supervisor:

Ao.Univ.-Prof. Dipl.-Ing. Dr. Johannes Schmid
Medical University Vienna,
Institute of Physiology
Department of Vascular Biology and Thrombosis Research
Schwarzspanierstr.17, 1090 Vienna

Internal Supervisor:

Dr.med.vet. Sandra Högl
University of Veterinary Medicine Vienna,
Unit of Laboratory Animal Pathology, Department of Pathobiology
Veterinärplatz 1, 1210 Wien

Evaluator

Dr. Juraj Hlavaty
University of Veterinary Medicine Vienna,
Department of Pathobiology
Veterinärplatz 1, 1210 Wien

Gender explanation

In response to gender justice and for creating a more readable thesis, I will use only one form of personalized words. Which means every personalized word will stay for both females and males, avoiding the use of both sexes.

Acknowledgments

In advance I would like to thank my two PhD (soon Postdoc) supervisors Bernhard Moser and specially Bernhard Hochreiter for teaching me all methods and laboratory as well computer analyzing tricks. Without the support and help of the other group members work would have been half the fun. The mouse prostates where embedded by previous group members enable the usage of a high number of samples, thanks for that. Giving me the chance for practice and time to write, I also want to thank my family and friends. And at last a big thank you goes to Lilli Möslinger for correction reading and writing support.

[Hier eingeben]

List of abbreviations

Ab	Antibody
Rt	Room temperature
PCa	Prostate Cancer
csPCa	Clinically significant PCa
PAP	Prostate acid phosphatase
PSA	Prostate Specific Antigen
TRUS	Transrectal ultrasound guided biopsy
AUA	American Urological Association
NICE	National Institute for Health and Clinical Excellence
EAU	European Association of Urology
MRI	Magnetic Resonance Imaging
mpMRI	Multi parametric MRI
PI-RADS	Prostate Imaging Reporting and Data System
DRE	Digital Rectal Examination
TNF α	Tumor necrosis factor alpha
ADT	Androgen deprivation therapy
H&E	Hematoxylin & Eosin
IDC-P	Intraductal carcinoma
PIN	Prostatic intraepithelial neoplasia
HGPIN	High-grade PIN
AMACR	α -methylacyl-CoA racemase
CTK14	Cytokeratin 14
AR	Androgen receptor
PTEN	Phosphatase and Tensin homolog
ERG	erythroblast transformation-specific (ETS)-related gene
TF	Tissue factor
PSMA	Prostate Specific Membrane Antigen
IHC	Immunohistochemistry
IF	Immunofluorescence
AI	Artificial intelligence
CNN	Convolutional neural networks
ML, DL	Machine learning, Deep learning

[Hier eingeben]

CAD	Computer aided diagnosis
LSCM	Laser scanning confocal microscopy
PMT	Photomultiplier tube

[Hier eingeben]

List of Content

1	Introduction.....	1
1.1	Prostate Cancer.....	1
1.1.1	Prostate Cancer Incidence.....	1
1.1.2	Clinical Features.....	2
1.2	Histopathology.....	3
1.2.1	Gleason Grading.....	4
1.2.2	Application of the Gleason Grading system.....	4
1.2.3	Carcinoma subtypes.....	6
1.2.4	Phenotype and histology of human and mouse prostate.....	7
1.3	Diagnostic Immunohistochemistry.....	9
1.3.1	Inflammation, Atrophy and HGPIN.....	12
1.4	Microscopy.....	14
1.4.1	Fluorescence microscopy.....	15
1.4.2	Confocal Microscopy.....	16
1.4.3	Multispectral imaging.....	17
1.5	Artificial intelligence (AI) in prostate cancer.....	18
2	Hypothesis and Aims.....	21
3	Material and Methods.....	22
3.1	Chemicals and reagents.....	22
3.1.1	Cell culture reagents.....	22
3.1.2	Reagents for Immunohistochemistry and H&E Staining.....	23
3.1.3	Reagents for RNA Isolation and qPCR.....	24
3.2	Material.....	25
3.2.1	Cell culture material.....	25
3.2.2	Material for IHC.....	25
3.2.3	Material for qPCR.....	25

[Hier eingeben]

3.3	Methods.....	26
3.3.1	Mouse Models	26
3.3.2	Immunohistochemistry.....	27
3.3.3	Microscopy	27
3.3.4	Haematoxylin-Eosin staining (H&E staining), IKOSA®.....	28
3.3.5	Cell Culture Work	28
3.3.6	RNA Isolation and qPCR	29
4	Results	30
4.1	Optimization of Fluorescence Antibodies	30
4.2	Fluorescence Multi- staining Quantification.....	45
4.2.1	Image Analysis in ImageJ.....	47
4.2.2	Image quantification of Multistain 1	48
4.2.3	Image quantification of Multistain 2.....	52
4.3	H&E stain annotation for IKOSA®.....	54
4.4	qPCR Results	57
5	Discussion	58
6	Summary- English	61
7	Summary- German	63
8	References	65
9	List of Figures	72
10	List of Tables.....	75
11	Attachment.....	1

1 Introduction

For men, Prostate cancer is an important health problem, as it represents the most common cancer type in biological males with the second highest number of cancer-deaths (surpassed only by lung)(*STATISTIK AUSTRIA* , Last access 02.04.2020).

Prostate cancer manifests almost exclusively in advanced stage and is often accompanied with low symptoms for the patient. Clinically relevant early symptoms are rare and only if the tumor has penetrated the prostatic capsule, obstructive micturition symptoms and / or hematuria are evidence for a tumor disease. The age-corrected disease rate has been increasing since 1999. This is mostly due to the increasing use of screening tests and the upcoming precision medicine (Mistry and Cable 2003).

1.1 Prostate Cancer

PCa is a cancer evolving in the prostate, which is a gland in the male reproductive system found below the bladder and in front of the rectum. In adult men affected with PCa, the 5-year survival rates approach 100 %. The 10-year risk of death ranges between three to eight percent. When accompanied by comorbidities, the risk of dying due to PCa in 10-years increases to 33 %. The curative treatment of localized PCa such as surgery and radiation, affect the quality of life negatively by inducing several urinary syndromes and sexual dysfunction. Androgen deprivation therapy compared with chemotherapy seem to extend the survival of metastatic disease, but other strategies are needed to improve outcomes in men with PCa resistant to traditional hormonal therapy (Litwin and Tan 2017).

1.1.1 Prostate Cancer Incidence

The rapidly growing cancer incidence is reasonably associated with an aging and growing population as well as socioeconomic developments (Bray et al. 2018). Treatment breakthroughs, such as immunotherapies, targeted therapies and a reduced number of patients who smoke contribute to the continuous decline in cancer mortality (Siegel et al. 2020). Prostate Cancer is the fifth leading cause of death and the second most frequent malignancy in men worldwide (Bray et al. 2018). Prostate Cancer has the highest incidence rate in Austria followed by breast cancer (*STATISTIK AUSTRIA*, Last access 02.04.2020). The Number of new cases in 2018 was 5598 in Austria, which represent 23,2 % of all cancers (Albert 2019). The incidence rate varies across the countries and populations with highest in African American, with a higher aggressiveness in comparison to White men. These Differences are due

to social, environmental, genetic factors and especially less diagnostic testing. The likelihood of developing PCa increases with age, reflected by an incidence rate of nearly 60% in men over 65 years (Rawla 2019). Primary prevention of PCa can be reached by better understanding causative risks and developing up-to-date diagnostic tools.

1.1.2 Clinical Features

The progress in characterizing disease risk has been meaningfully changed since 2011. The emergence of several new diagnostic tools for men improved risk stratification and prognostic information (Litwin and Tan 2017).

Prostate specific antigen (PSA)

Beyond the standard clinical parameters, biomarkers such as proteins, metabolites, RNA transcripts and epigenetic modifications of DNA that are detectible in patient tissues and blood samples revolutionized the practice of oncologists. Prostate Cancer management has been using biomarkers longer than most cancers. Prostatic acid phosphatase (PAP) in the serum of patients was the first discovered clinical marker for illness development. The secreted serine protease PSA is produced only by epithelial cells of the prostate gland and replaced PAP as the commonly used biomarker in the 1980s (Hoogland et al. 2014). In healthy tissue, just small amounts of PSA leak into the circulation. An increased serum PSA is not only an indicator for prostate cancer, but can be caused by inflammation, prostatitis, acute urinary retention and benign prostatic hyperplasia, making it an insensitive and unspecific marker. The use of PSA for screening tests led to a misleadingly number of prostate cancer diagnosis with most having indolent disease. The American Urological Association (AUA) recommend screening for men aged 55-69 in biennial interval to reduce overdiagnosis (Ballentine Carter et al. 2013). The combination of PSA test with digital rectal examination (DRE) significantly enhances the screening results. Due to its anatomic position in the pelvis the prostate allows for easy access and enables clinical staging by digital rectal examination. Prostate size, nodules and lumps were characterized and set up the basis in the diagnosis for prostate cancer (Prensner et al. 2012, Ramon and Denis 2007).

Ultrasound-guided biopsy

The go-to diagnostic procedure to identify prostate tumor is the needle-biopsy, in which several thin, long cylinders of tissue are extracted from the prostate lesions. This is a generally painful

process that can itself have various side effects. There are three general indications that are required in the decision process for biopsy: abnormal DRE, elevated PSA levels (greater than 4 ng/ml, normally 0-3,5 ng/ml) and clinical suspicion (Streicher et al. 2019). But these traditional first hints lack in sensitivity and specificity leading to a high number of unnecessary biopsies (Streicher et al. 2019). Transrectal ultrasound guided biopsy (TRUS) was introduced in 1968 and enables the navigation of the biopsy needle to various locations in the prostate and is also used for volume measurements. In the 1990s the traditional sextant biopsy described by Hodge et al. which comprises six core biopsies from apex, mid and base of the right and left prostate was widely used but it became apparent that it had a false-negative range of 30%-35%. There were many different investigators studying on alternative extended biopsy schemes improving the diagnosis accuracy (Ramon & Denis, 2007). The extraction of at least two cores per lesion is recommended by the AUA and Society of Abdominal Radiology, but additional cores increase PCa detection at lower PCa risk (Leyh-Bannurah et al. 2020). However, around 70 % of transrectal or transperineal ultrasound guided biopsies show cancer but of these only 40% are clinically significant (csPCa). In Addition, they can cause urinary tract infections, sepsis or severe rectal bleeding (Waldron and Chowdhury 2020). Compared to systemic transrectal ultrasound biopsy multiparametric magnetic resonance imaging (mpMRI) and guided targeted biopsy (TB) demonstrate superior modes.

Magnetic resonance imaging (MRI)

Clinicians have turned to the adoption of multiparametric MRI (mpMRI) according to the guidelines of the European Association of Urologists (EAU) which enables the non-invasive determination of watchful areas of the prostate. With a sensitivity of 93% the mpMRI can save a quarter of affected from undergoing a prostate biopsy and demonstrate the highest diagnostic performance in the discovery of csPCa. Multicenter trials that compare accuracy of TRUS and mpMRI such as PROMIS and PRECISION (Ahmed et al. 2017, Kasivisvanathan et al. 2017) (Ahmed et al. 2017), suggest that MRI markedly outcompeted systemic biopsy and represents the favored diagnosis tool. According to the final results of these trails clinical practice will maybe change rapidly (Streicher et al. 2019).

1.2 Histopathology

Malignant neoplasms of the prostate indicate prostate cancer and are in the vast majority of epithelial origin. In surgical pathology, the most common tissue examination requires light

microscopic evaluation of haematoxylin and eosin (H&E) colored sections(Humphrey 2017). This staining facilitate the examination of the cellular and tissue structure details by staining basophilic components blue (haematoxylin - nuclei) and acidophilic structures pink (eosin - cytoplasm). The grade of differentiation presented by the altered Gleason grading system is the standard histopathological characterization of needle-biopsies(Hoogland et al. 2014, Humphrey 2017).

1.2.1 Gleason Grading

From 1960 to 1975, the Veterans Administration Cooperative Urological Research Group (VACURG) developed together with Donald F. Gleason five histological patterns in the order of increasing biological malignancy(Hoogland et al. 2014). Which means 1 is most similar to normal prostate and 5 represents the most differentiated one. Because the tissue can show a variety of different stages and PCa behaves more in proportion to its average histology, the two most abundant grades were added together creating a basic correlation with mortality rates (e.g. 3+4=7). With the help of a simple drawing seen in Figure 1A, pathologists could easily adapt and successfully implement the “Gleason” Grading system for improved standardization. But, due to substantial subjective variation and histologic grading, the Gleason score is not a verifiable scalar measurement and had a systemic bias toward low histologic scores. Follow up studies were needed to collect well-standardized data and improve PCa grading (Gleason 1992).

1.2.2 Application of the Gleason Grading system

In 2005, and 2014 urologic pathologists were invited to the “International Society of Urological Pathology (ISUP) Consensus Conference on Gleason Grading” to achieve consensus including several grading issues(Epstein et al. 2005, Hoogland et al. 2014).

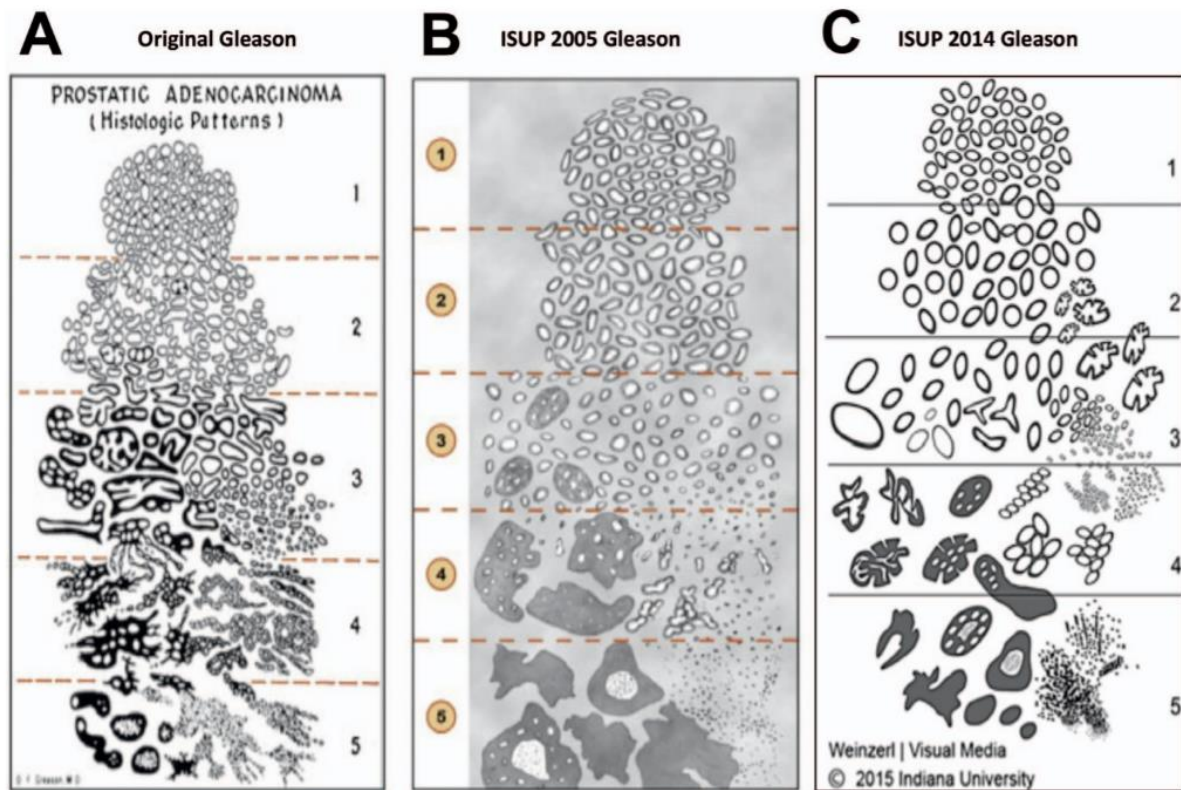


Figure 1: Evolution of the Gleason grading system (Paner et al. 2019).

Amongst other things Gleason 2 (1+1) should be avoided in diagnosis, today it would be referred as adenosis (atypical adenomatous hyperplasia). Also, Gleason grade 4 or 5 should also be reported even when they are existing on less than 5% of the tumor surface. Gleason grades should not be described as intraductal carcinoma (ICD-P described in chapter 1.1.3.) as it correlates with high-stage invasive adenocarcinoma (Epstein et al. 2005, Humphrey 2017).

At the ISUP in 2014 they reached 90% accordence for the adaption of the new grading system that shows five prognostically distinct grade groups presented in 2013 by the group of J.I. Epstein. With the assumption of having the same prognosis many classification systems have been arranged imprecisely (7: 4+3 had a significantly worse prognosis than 3+4). Through the simplification from Gleason scores 2 to 10 to Grade Groups 1 to 5 the new grading categories provide a more accurate stratification and also have been acknowledged by the World Health Organization for the 2016 edition of Pathology and Genetics. (Epstein et al. 2016).

1.2.3 Carcinoma subtypes

High-grade prostatic intraepithelial neoplasia (HGPIN)

HGPIN, which is a prostatic precursor lesion, have nuclear and cytoplasmic invasive adenocarcinoma featuring cells in pre-existing acini and ducts. The enlargement of nucleoli in at least 10% of the cells belong to the key diagnosis hallmark. Cellular crowding and nuclear pseudo stratification is shown by the four architectural subtypes (Figure 2), where tufting is the most common one. There is speculation of Myc being overexpressed and a critical driving force in most human HGPIN lesions, although the underlying mechanistic basis is not yet understood (Trabzonlu et al. 2019).

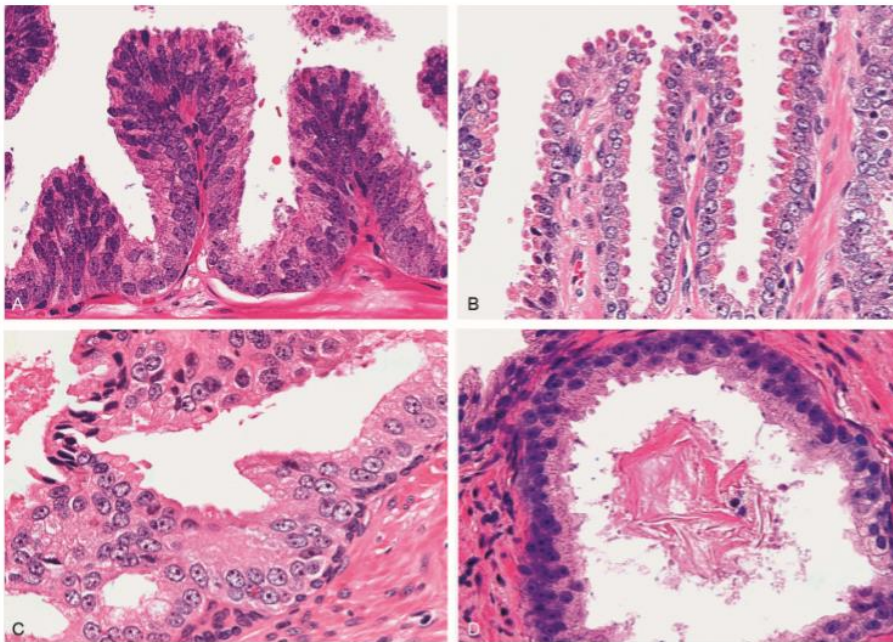


Figure 2: HGPIN patterns: (A) Tufting (B) Micropapillary (C) Cribriform (D) Flat pattern (Bostwick and Cheng 2014)

Intraductal carcinoma (IDC-P)

“Intra-acinar or intraductal neoplastic epithelial proliferation filling acini as well as prostatic ducts with preservation of basal cells and formation of either solid or dense cribriform patterns, or a loose micropapillary pattern with either marked atypia (nuclear size 6x normal or larger) or comedonecrosis”, belong to the criteria of Intraductal Carcinoma from Guo and Epstein 2006 S1 (Guo and Epstein 2006, Humphrey 2017). IDC-P is often associated with high-grade and high-stage invasive adenocarcinoma and is a prognosticator for aggressive disease that is seen in around 3% of needle core cases and 17% to 40% of radical prostatectomy. Immunohistochemistry enables the differentiation between high-grade prostatic intraepithelial neoplasia (PIN) and invasive high-grade prostatic acinar adenocarcinoma (Humphrey 2017).

In contrast to PIN, the cytoplasmic Phosphatase and Tensin homolog (PTEN) is lost in about 85% of IDC-P and erythroblast transformation-specific (ETS)-related gene (ERG) occurs in a higher frequency in IDC-P as seen in Figure 3.

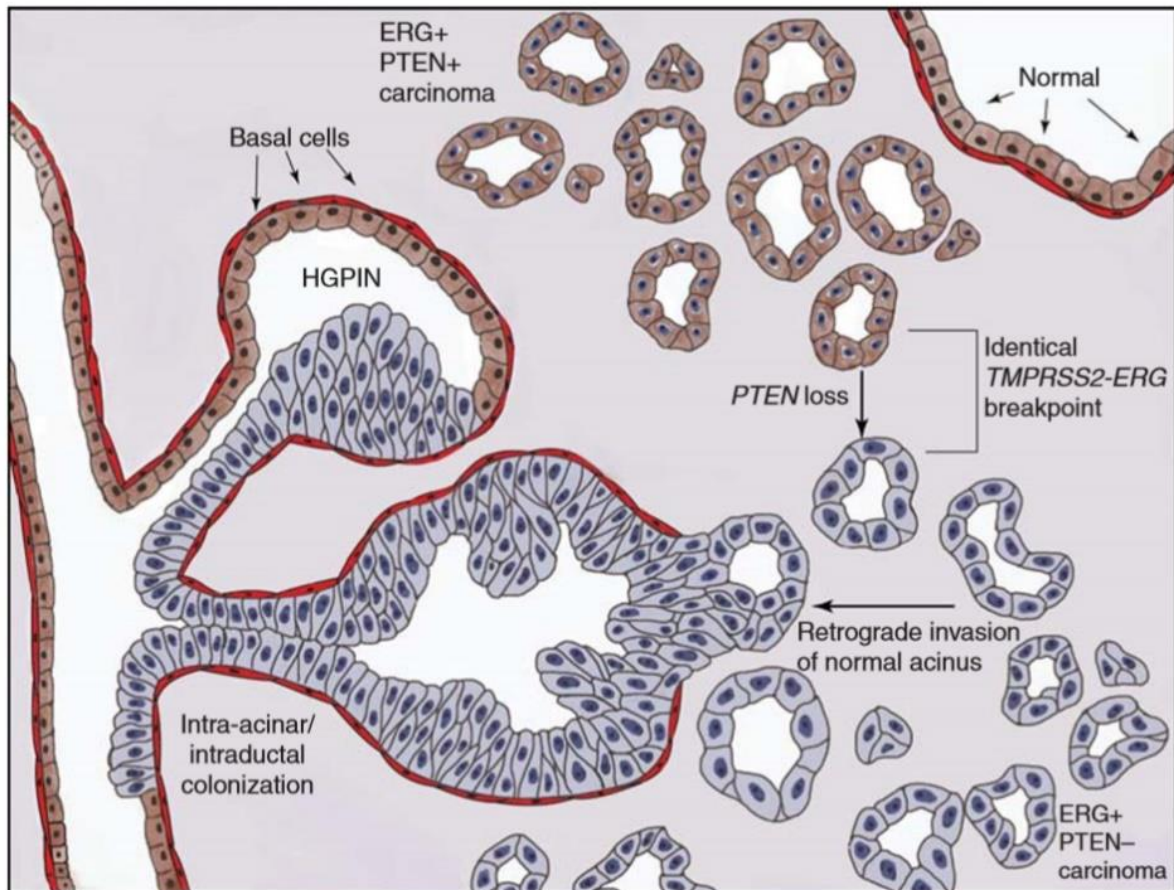


Figure 3: model of retrograde glandular colonization or post invasive intraepithelial carcinoma (Trabzonlu et al., 2019)

Invasive carcinoma is also characterized by the entire loss of basal cells rather than IDC (Humphrey 2017). IDC-P still remains difficult to diagnose in practical pathological or clinical use as well as further definition also of comedonecrosis is needed (Comp rat 2019).

1.2.4 Phenotype and histology of human and mouse prostate

The anatomy and morphology of prostates among mammals varies remarkable. While in dogs and humans the prostate is a compact solitary structure the rat and mouse prostate consist of four distinct lobes that are placed around the urethra. The dog is the only animal where spontaneous prostate cancer can metastasize to bone. Nevertheless, due to the many

advantages of using mice (quick breeding and maturation, easy housing, small size), they continue to be the most widely used animal model (Oliveira et al. 2016). Human as well as mouse accessory organs originate from Wolffian ducts and the urogenital sinuses. Both also have similar functions, androgen-sensitive organs consisting of lobular glands with distinct differentiated epithelial cells, but there are crucial differences, as shown in Figure 4. (Shappell et al. 2004). Using the dissecting microscope, the mouse prostate lobes can be distinguished after their spatial orientation. The jelly-like pink structure that wraps the urethra partially ventral is recognized as ventral prostate (VP). The lateral prostate (LP) flanks the VP with two lobes. At the base of the seminal vesicle, the butterfly-shaped dorsal prostate (DP) is bilaterally located which together with LP is referred as dorsolateral prostate (DLP). Closely attached to the seminal vesicle, along its entire curving length is the anterior prostate (AP) or “coagulating glands”. In contrast to mice, human prostates consist of distinct glandular regions. Anterior fibromuscular stroma, periurethral transition zone (TZ), peripheral zone (PZ) and central zone (CZ). The TZ has been associated with benign prostatic hyperplasia whereas CZ is rarely the site of origin PCa, but in the PZ that surrounds the proximal prostatic urethra adenocarcinoma occurs in 75-85% of patients(Shappell et al. 2004). Comparing the interspecies mRNA expression and anatomical homology of the mouse DL seem to be most representative of human PZ (Oliveira et al. 2016).

Both, mouse and human prostates consist of a tree-like network of glands (acini), ducts with columnar luminal secretory cells(Oliveira et al. 2016). These secretory cells are characterized by low molecular weight cytokeratin (CK 8, 18) and androgen receptor expression and are surrounded by basal cells that are less abundant in mice and expressing the high molecular weight CK5 and p63,

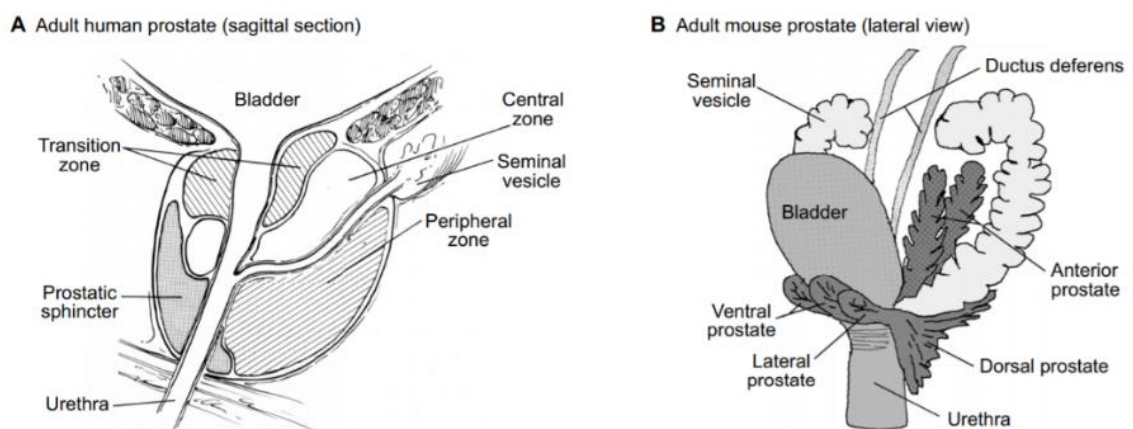


Figure 4: overview of human and mouse prostate anatomy (Toivanen & Shen, 2017)

and neuroendocrine cells. The most conspicuous difference however can be found in the stromal component: In mice it is sparse with minimal smooth muscle cells whereas in humans it is well developed as an engulfing fibromuscular region seen in Figure 5.

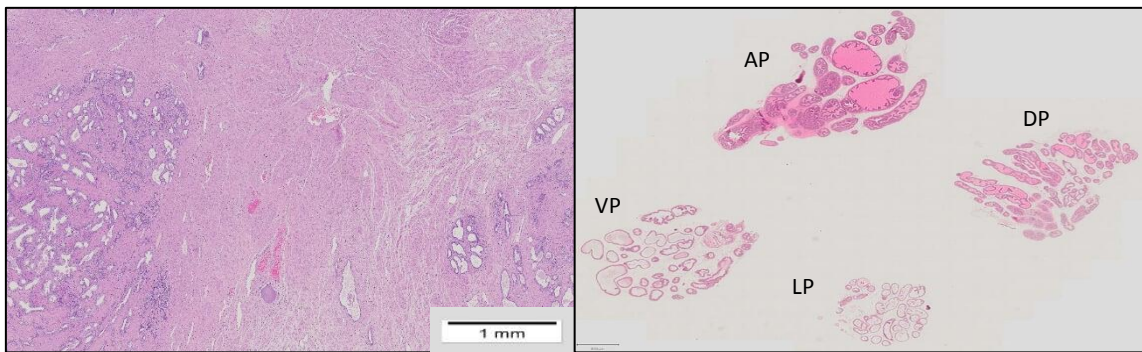


Figure 5: human vs mouse prostate histology: AP (Anterior Prostate), DP (Dorsal Prostate), VP (Ventral Prostate), LP (Lateral Prostate)

The distinctive histology of mouse prostate lobes enables their differentiation. Because of the complex acini characterized by typical papillary or cribriform patterns and high abundant eosinophilic secreting cuboidal to columnar epithelial cells, the AP is easy to distinguish. As well as the AP, the DP lobes also have homogenous and eosinophilic secretion of the lumen, but the lobes consist of smaller acini in diameter than the others surrounded by relatively dense stroma and epithelium with moderate infoldings and occasional tufting. The VP gland present the least amount of infoldings compared to the others, is lined by a flat mucosa, surrounded with a thin fibromuscular layer and contains homogenous pale serous secretions. The acini of VP are moderate to large comprised of columnar epithelial cells with small, basally located nuclei. Compared to the VP the LP lobes show different sizes of granular lumen from small to large containing eosinophilic secretion and the cuboidal to low columnar epithelial cells having small infoldings. This comprehensive understanding of mouse prostate histology provide decision making to present specific results made with this species (Oliveira et al. 2016).

1.3 Diagnostic Immunohistochemistry

Currently there are three antibodies that are used routinely in adenocarcinoma diagnosis via immunohistochemistry. The anti-keratin antibody 34 β E12 (high-molecular-weight keratin) is used as a general marker for the basal cell layer while anti-p63 stains the important tumor-

suppressor p63, also located in the basal cell layer. They are used to recognize intact or fragmented basal cell layers, indicating PIN instead of cancer. One must take in consideration that some benign glands can have an absent or discontinuous basal cell layer and 50% of adenosis (non-cancerous change in a gland) do not stain for basal cells. For the staining of dysplastic secretory cells and prostatic carcinoma α -methylacyl-CoA racemase (AMACR) and c-Myc are the most prominent markers (Humphrey 2017, Krzyzanowska et al. 2016). The simultaneous staining with 34 β E12, p63, racemase is described as triple cocktail and is added by c-Myc to the quadruple antibody cocktail. Various molecular markers in immunohistochemistry can sustain and improve pathologic diagnosis (Bostwick and Cheng 2014).

c-Myc

c-Myc is part of the MYC family of transcription factors, and is said to regulate up to 15% of all human genes (Chen et al. 2018). It is involved in many processes, including proliferation, cell cycle, cell growth, metabolism, protein synthesis, stem cell renewal and DNA replication, but is also described as a proto-oncogene, being altered in many human cancer types. In PCa, it is found overexpressed in about 70% of cases. In cases where AMACR staining is absent or just marginal, a stain for c-Myc can provide a lot more information. Unlike racemase, c-Myc amplification is linked to Gleason score and has a prognostic potential for tumour recurrence after radiotherapy. Immunohistochemistry of the c-Myc protein correlates with c-Myc amplification which leads to enlarged nucleoli and increased nucleolar number of luminal epithelial cells in vivo (Bostwick and Cheng 2014, Hoogland et al. 2014). There exists an antagonistic relationship between c-Myc and AR, which is thought to be a driving force in PCa (Barfeld et al. 2017). Despite the fact, that c-Myc is altered in >50 % of cancers, targeting still remains a big challenge due to its “undruggable” protein structure and deleterious side effects an inhibition might have on normal tissue. Additional approaches are made by interrupting Myc-Max complex or Myc transcription and or translation inhibition and Myc destabilization (Chen et al. 2018).

Cytokeratin 14 (CTK14), p63

The human prostate epithelium consists of luminal secretory cells and a basal cell layer, from where more committed exocrine or neuroendocrine cells mature. The immunohistochemistry staining of the complex gene family of intermediate filaments called Cytokeratins have widely been used to study subpopulations in the benign and cancerous prostate epithelial. While a

high K8 and K18 expression as well as the absence of K14 is typical for the luminal prostate epithelial, a high-molecular-weight keratin 5 and 14 and a weak expression of K8 and 18 are used for the characterisation of the basal cells. These cytokine expression patterns are altered during cancerogenesis. CTK14 show very low to no levels in PIN and carcinoma lesions and is specifically expressed in the normal basal cells of the prostate epithelium, making this Ab a vulnerable diagnostic tool for the discrimination of benign lesions and malignancies (Van Leenders et al. 2001, Yang et al. 1997).

In diagnostically challenging cases the combination of p63 with high-molecular-weight cytokeratin increases the sensitivity and specificity of the basal cell identification due to its role in epithelial differentiation and proliferation (Bostwick and Cheng 2014). The p53 family member is required for the embryonic development and tend to be underexpressed in adenocarcinomas compared with normal prostate. Changings in the nuclear-cytoplasmic shuttling contribute to initiation and development of PCa, reflecting the essential role of the nuclear localization of p63, which can be of prognostic significance (Dhillon et al. 2009).

Ki67

Proliferative activity can be detected immunohistochemically by a marker (MIB-1) directed against Ki67, which reflects the expression during the late G1,S,G2 and M phase of the cell cycle. A high Ki67 labeling index is associated with lower cancer-specific survival and distant metastasis. It is also used for the cancer-specific survival prediction after prostatectomy (Bostwick and Cheng 2014).

Prostate-specific membrane antigen (PSMA)

The transmembrane glycoprotein PSMA encoded by folate hydrolase 1, is histological detected marginally in benign prostate tissue, but accelerates (100 times greater than in most other tissues) its expression on prostate adenocarcinomas, which explains the interest since its discovery in 1986. A lot of investigation has been made in targeting PTEN by antibodies as well as small-molecule agents for the use in malignant castration resistant prostate cancer management (Donin and Reiter 2018). Its essential role in prostatic malignant tissues can serve as therapeutical target and PCa diagnosis tool (Situ et al. 2017).

Tissue Factor (TF)

Under normal conditions TF is not located within the blood circulation, but in case of injuries the transmembrane glycoprotein binds to its cofactor VII/VIIa, forming a complex and thereby

activating the extrinsic coagulation cascade. Due to its effects on angiogenesis, altered TF expression leading to blood clots is associated to tumour growth. Tumour cells that have access to factor VII in leaky vascular endothelium causing disseminated intravascular coagulation and enhance metastasis (Akashi et al. 2003). The evaluation of the TF expression status may indicate the tumor metastatic potential and can be used as diagnostic marker for tumor cells (Abdulkadir et al. 2000).

Androgen receptor (AR)

The ligand-activated transcription factor AR is involved in key cellular processes like anabolic metabolism and cell cycle control. Androgen receptor expression is critical to normal and malignant PCa development and has been linked to a diminished disease-free survival (Heinlein and Chang 2004, Krzyzanowska et al. 2016). The androgen-independent (CRPC) PCa mostly express AR although the expression is heterogeneous within tumour foci. Mutations may contribute to the failure of endocrine therapies suggesting altered AR signaling pathways (Heinlein and Chang 2004). Commonly, AR is dysregulated at advanced stages of PCa, but a reliable biomarker for AR expression has not been developed yet (Krzyzanowska et al. 2016). The immunostaining of Androgen receptor is positive in 95% of prostate adenocarcinomas maintaining an active AR signaling network (Bostwick and Cheng 2014). Treatment with AR antagonists over a long period typically achieve androgen signal deprivation, but cancer cells often evolve into an AR-independent cancer with androgen resistant cells showing elevated metastatic growth. Pro-inflammatory stimuli in combination with AR treatments confirm exclusive feedback in comparison to the stimulation of just one, showing specific transcriptional programs (Staal and Beyaert 2018).

1.3.1 Inflammation, Atrophy and HGPIN

As chronic Inflammation belongs to the progression of several forms of carcinoma, it is associated to atrophy and proliferative changes in epithelial malignancies. After androgen deprivation, diffuse atrophy lesions develop uniformly consisting of cuboidal luminal cells with a prominent basal cell layer above. Focal atrophy on the other hand develops heterogeneously in the presence of androgen and contains a non-prominent basal cell layer. This lesions tend to be proliferative and develop predominantly in the peripheral zone suggesting an association to PCa (Nakai and Nonomura 2013). The premalignant proliferative inflammatory atrophy is identified by cellular injury induced by the exposure of reactive oxygen species caused by

chemical, physical or bacterial factors. Additionally regenerating cells have an elevated risk of mutation as well as cancer initiation, promotion and progression (Bostwick and Cheng 2014).

Nuclear factor-kappa B (NF- κ B) signaling proteins

NF- κ B plays a major role in pro-inflammatory processes. Bacterial or viral antigens, cytokines and growth factors are recognized by members of the TNF receptor superfamily or toll-like receptors and are thereby activating NF- κ B and enhance the inflammatory response by the release of inflammatory cytokines (Nguyen et al. 2014). The expression of genes required for inflammation is activated by a group of transcriptional regulators comprised of five members. The NF- κ B family members possess the N-terminal Rel homology (RH) domain included in DNA binding and is divided in two classes. The class one can be identified via C-terminal transactivation domain including Rel (c-Rel) RelA (p65) and RelB. Whereas class two has a inhibitory C-terminal ankyrin repeats creating transcriptionally active p50 and p52 proteins via NF- κ B1(p50, precursor p105) and NF- κ B2 (p52, precursor p100) (Lessard et al. 2005). I κ B proteins mediate the association to NF- κ B dimers via ankyrin repeats. Under resting conditions, I κ B binds inactive NF- κ B homo- and heterodimers in the cytoplasm, thereby inhibiting its function as nuclear transcription factor. There exist two well described NF- κ B signaling pathways. The phosphorylation and following ubiquitination-dependent degradation of I κ Bs by the activation of the trimeric I κ B kinase complex (IKK1, β , γ) describes the canonical pathway. In contrast, in the non-canonical pathway, RelB/p52 dimers are released due to activation of IKK1 dimers by NIK (NF-kappa-B-inducing kinase) that selectively bind and phosphorylate p100 (precursor of p52 subunit). These dimers act as transcription factor by moving to the nucleus and regulating the transcription of several genes related to differentiation, cell growth, apoptosis and inflammatory responses. In prostate cancers, NF- κ B related proteins seem to be aberrantly active. The nuclear location of RelA in primary PCa is related to poor clinical outcomes described by Lessard et al, 2003. RelA also shows specific expression in PCa but was not correlated to Gleason Score in the study of Seo et al. (Seo et al. 2009). The validation of other NF- κ B subunits and combinations are needed to provide further evidence for a role as prognostic marker (Lessard et al. 2005).

IKK1

For the acquisition of invasive and metastatic capacities in PCa, the IKK/ NF- κ B pathway is suggested to be a key mediator. Preferentially IKK1 dimerises with IKK2 but may also be found as homodimer with IKK1. Via the repression of the putative suppressor of metastasis Maspin,

IKK1 functions pro-metastatically. By inhibiting IKK1, tumour growth is diminished due to its effects on NF- κ B and pathogenic conditions (improved invasion, metastasis), making IKK1 a potential target for advanced prostate cancer therapy (Mahato et al. 2011).

IKK2

IKK2 represents an essential mediator between extracellular signaling and NF- κ B being activated by viral or bacterial infections as well as the production of inflammatory cytokines and chemokines (Birbach et al. 2011). In some forms of PCa, IKK2 may play a role in regulating cancer stem-like cells (CSC), epithelial-mesenchymal transition (EMT) and elevated induction of apoptosis through NF- κ B dependent and independent mechanisms. IKK2 targeting is suggested to be a feasible approach against CRPC, where such pathways might be activated (Zhang et al. 2016).

Tumor necrosis factor alpha (TNF α)

Several different cell types including lymphoid cells produce TNF α , which is a member of the tumor necrosis factor superfamily. The inflammatory cytokine is involved in the induction of several biological processes like apoptosis and survival. Through receptor mediated signal transduction, the TNF α activation is leading to apoptosis via the death-signaling pathway. On the other hand, TNF α can activate NF- κ B signalling through a survival pathway, that is also receptor mediated. TNF α corresponds differently to normal and tumor cells, which may be beneficial in the specific targeting of tumor cells by not harming normal cells (Chopra et al. 2004). The inhibition of TNF α induced NF- κ B regulation by structural analogues of platelet-activating factor (PAF) antagonists is leading to apoptosis in tumor cells (Shi et al. 2013).

1.4 Microscopy

In the assessment of morphologic information as well as protein expression, immunohistochemistry (IHC) reflects an essential method (Rojo et al. 2009). In IHC, specific antibodies are used to stain targets of interest. The classical procedure of IHC, as it is employed in the clinical routine, involves the use of peroxidase bound antibodies leading to a visible color reaction and the use of classical brightfield microscopy. The advantage is that these stained samples are highly durable and can be stored and analyzed for decades. However, due to the use of these reaction based dyes, most stains can only include one or maximally two targets and allow no quantification due to the non-linear amplification of signal

during the color reaction. These problems can be overcome by using fluorescent dyes instead of biochemical reactions, which allows quantification of multiple dyes simultaneously within the same sample.

To improve reproducibility and standardization of IHC results in the clinic, the focus should be set on routine quantification and implementation of current digital imaging technology (Rojo et al. 2009).

1.4.1 Fluorescence microscopy

Fluorescence microscopy requires samples that are fluorescent. The underlying process of fluorescence involves the excitation of the fluorescent molecule (fluorophore) by absorption of light and a few nanoseconds later the relaxation of the excited state and a resulting emission of light. Some of the energy is lost in this process, which means the emitted photon has less energy and thereby a higher wavelength than the absorbed one. This difference is known as Stokes shift as seen in Figure 6. In a microscopy setup, special filters are used to separate excitation and emission light, resulting in a selective signal with a very high signal to noise ratio. (Lichtman and Conchello 2005, Sanderson, Michael et al. 2016).

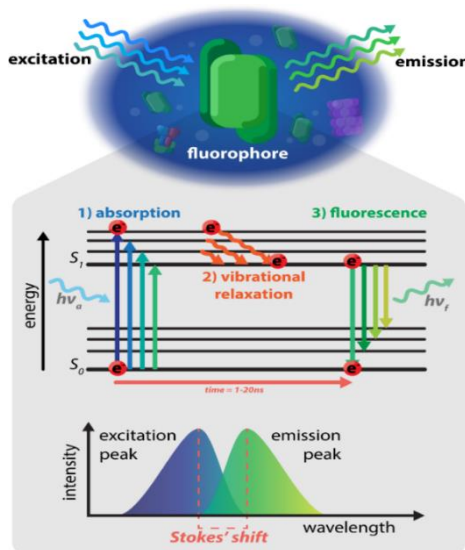


Figure 6: excitation emission principle (Bernhard Hochreiter)

Classical fluorophores such as Fluorescein were often very limited within their capabilities due to their low brightness and susceptibility to bright illumination. However, nowadays Fluorophores come in a large variety of colors, meaning that they can have widely different excitation and emission wavelengths, and modern dyes are bright and highly stable. The

combination of these allows them to be spectrally separated, meaning that each dye can be excited and measured individually, which is impossible in classical brightfield microscopy.

In samples with multiple fluorophores the overlapping emissions excited by the same wavelength lead to bleed-through between signals associated with different fluorophores. Therefore, organic synthesis realizes ever wider spectral ranges to choose fluorophores with little overlap in excitation and or emission spectra. That is why knowing the absorbance and emission specifics helps to choose the right filters, lasers in microscopes, without crosstalk from another.

The most common approach is epifluorescence, in which the same light path – and hence objective – is used to direct the excitation light onto the sample as well as to collect the fluorescence. To separate the excitation from the emission, dichroic beamsplitter mirrors are used enabling the reflection of lower wavelength from the light source and the transmission of longer wavelength of the emitted fluorescence. In fluorescence microscopy the so-called filter cube consists of an excitation filter, a dichroic mirror at 45°, and a barrier/emission filter. In order to determine what is the right cube the access to spectral filtering as well as the excitation and emission curves are essential. Traditionally, excitation light was provided by a mercury or xenon high pressure bulb, but LEDs are rapidly adopted due to their much higher lifetime and more constant illumination.

The advantages of wide-field microscopy include fast imaging, low costs, simplicity and flexibility. However, low image resolution, shading artefacts due to uneven illumination and problems with pixel registration are disadvantages. (Lichtman and Conchello 2005, Sanderson, Michael et al. 2016).

1.4.2 Confocal Microscopy

Images in wide-field microscopy consist of in and out-of-focus light due to the complete illumination of the specimen, decreasing the signal to noise ratio (St Croix et al. 2005). To overcome the drawback of point-by-point illumination, confocal microscopy rejects out of focus light by inserting a pinhole so that only focused light passes to the detector. The name “confocal” comes from the pinhole that is conjugated to the focal point of the lens. In the late 1950s Marvin Minsky already moved the stage under the illumination source and used a high intensity light source. Using laser (a bright point source) as light source is done by laser scanning confocal microscopy (LSCM). Lasers are important for the collection of enough light and provide a high intensity light source. The laser light is reflected by rapidly moving motorized

mirrors (galvano scanner) than direct the lightbeam onto specific points on the sample, creating a point-by-point image. This brings the big advantage of uniform illumination and a high excitation intensity at the cost of longer acquisition times (Denis Semwogerere 2005).

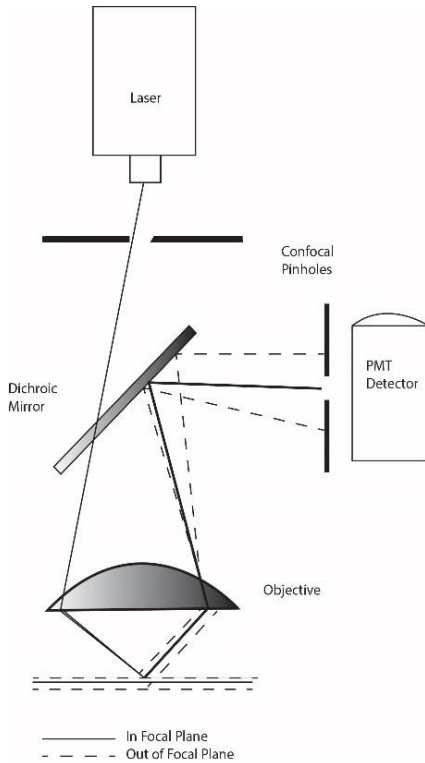


Figure 7: Optical configuration of a laser scanning microscope

The detection of emitted light in LSCM is done with a photomultiplier tube (PMT) which has a much higher sensitivity compared to camera chips used in widefield microscopy.

1.4.3 Multispectral imaging

Fluorescence microscopy is a continuously expanding method, which can be seen in the introduction of more and more variants of fluorescent labelled antibodies available as marker and new fluorophores. This enables the visualization of several cellular proteins on the same sample with the aim of specific fluorescent labels. Methods that accurately correct channel crosstalk via sequential imaging allow for reliable multiple fluorescent separation (Zimmermann 2005). The connection between the fluorophore concentration and the observed signal is linear. The so called “linear unmixing” is able to unmix each component if the fluorescent spectra of each dye is known (Haraguchi et al. 2002). The total detecting signal S

equals the combination of the amount of contribution by a specific fluorophore A and the reference emission spectra of the fluorophore seen in the following equation.

$$S = A * R$$

This linear equation can be solved with singular value decomposition creating clear representations of the separated fluorophores after weighing matrix A calculation. All fluorophores present have to be considered for the calculation and also background contribution has to be defined as additional spectra (Zimmermann 2005). The availability of tools is expanded by using the multi-fluorescence imaging technique, because unusable dyes that did not fit standard filters, overlapped spectrally, or had a small Stokes shift now can be used (Paddock 2001).

Using more than one target requires the use of multiple primary labelled antibodies (Abs) or primary Abs raised in different species to counteract cross-reactivity with secondary antibodies. However, there is no other technique enabling the simultaneous analysis within a single tissue section and thereby allow accurate cell discrimination and spatial information (Gorris et al. 2018). Automatic image analysis and qualifications of IHC provide more reliable and uniform results compared to manual evaluations (Rojo et al. 2009).

Commonly, cellular-markers are detected by immunohistochemistry (IHC), but results and interpretations are challenging to for the implementation into the in clinical setting due to the lack of regulated quantification methods (Krzyzanowska et al. 2016).

1.5 Artificial intelligence (AI) in prostate cancer

AI is defined by Goldenberg et al. as “ability of a machine (for example, a computer) to independently replicate intellectual processes typical of human cognition in deciding on an action in response to its perceived environment to achieve a predetermined goal” (Goldenberg et al. 2019,S391). For the execution of mathematically modelled algorithms supervised machine learning (ML) requires training samples (instances) mapped to input variables (features, predictors) belonging to several output variables (labels, targets). In the “training”, these algorithms were optimized to enable the prediction of labels by analyzing features for instance grade of histopathological images of prostate tissue where features are observed colour values and labels are the assigned Gleason grade. In contrast to supervised learning, unsupervised learning classifies the samples based on features without corresponding labels, predicting the risk of recurrence of IHC PCa samples independent of tumour stage parameters seen in Figure 8(Goldenberg et al., 2019).

Machine and deep learning technology based on Convolutional neural networks (CNN) are used to perform image interpretation and enable computer aided diagnosis (CAD). Today massive parallel processing capabilities are not expensive anymore, driving image understanding software. This allows for tissue pattern understanding of complex H&E images in a precise and automated way, which reflects the biggest diagnostic challenges for pathologist and the human visual cortex. To enhance diagnostic practice AI will provide some opportunities like distinction of benign and tumor, identification of micrometastases, grading of dysplasia and IHC scoring of multiple biomarkers. However, with opportunities also challenges will come, such as the translation of results to reliable, safe and robust predictions as well as meaningful diagnostic and prognostic opinions. Starting to integrate digital pathology in routine diagnostic practice will make the true impact of AI realizable (Salto-Tellez et al. 2018).

The increasing reliability, reproducibility and diagnostic accuracy enabling quantitative image analysis is realized by the whole slide imaging system for digital pathology and has recently been FDA approved. The adaption of deep learning in PCa pathology aiming to detect invasiveness in needle biopsies has been made serious efforts. Arvaniti et al. used 641 Tissue Micro Array (TMA) images to train an automated Gleason scoring CNN application. They achieved comparable inter-observer agreement between two ground truth pathologists and assignments significantly stratified in two disease-specific survival groups with superior prognostic potential. The cancer likelihood map of Litjens et al. achieved an Area under the curve (AUC) of 0.99 on slide-level detection (Acs et al. 2020).

Doyle et al. achieved a positive predictive value of 86% by a handcrafted feature-based approach of 214 patients, making the technique promising for future study. Providing adequate, properly labeled training sets and defined interaction of pathologists with the computer remains challenges that has to be tackled (Goldenberg et al. 2019). Artificial intelligence seems to be the next step towards precision pathology, therefore pathologists need to be equipped with more quantitative histopathologic diagnosis tools (Acs et al. 2020).

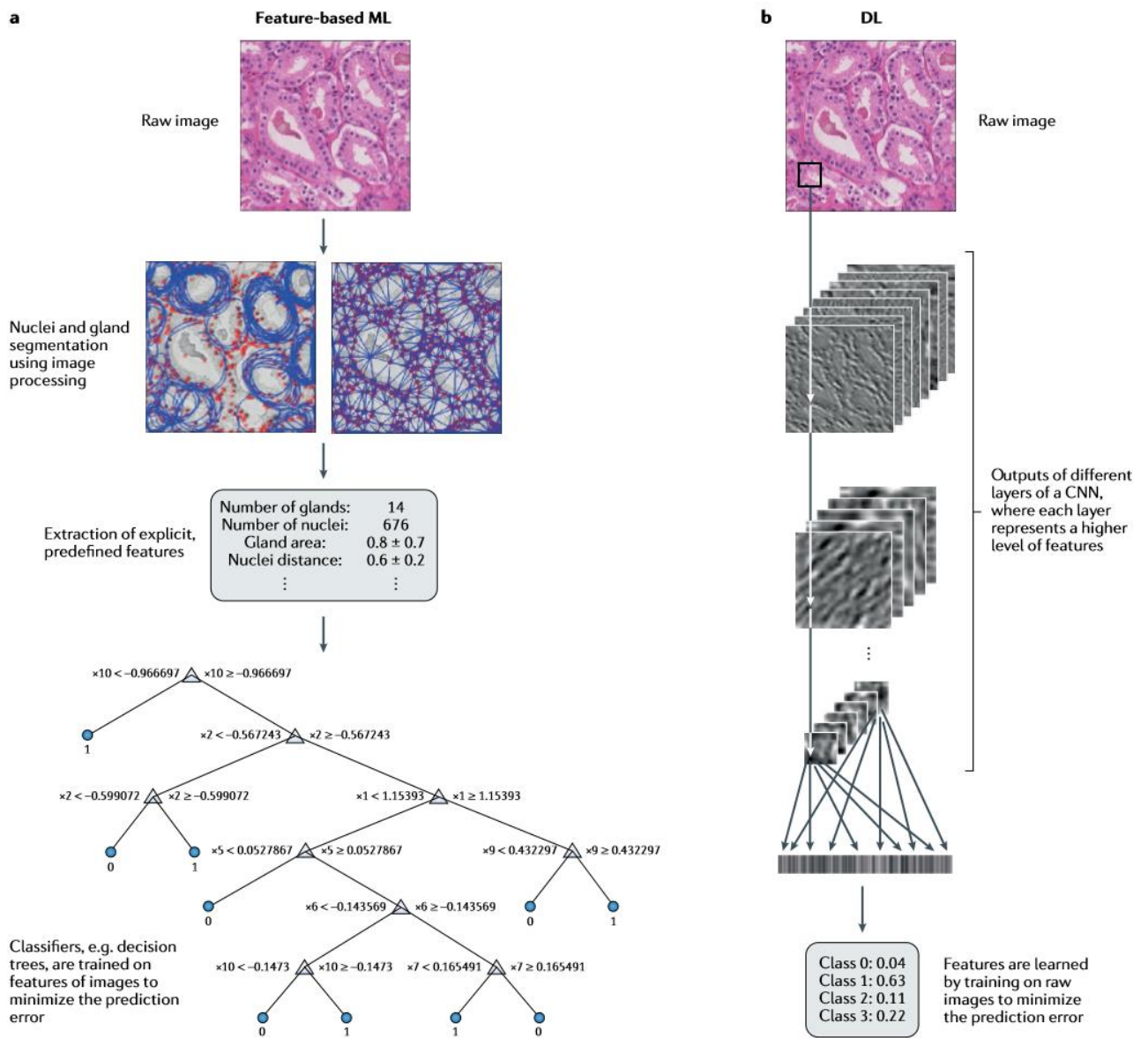


Figure 8: hand grafted feature-based ML versus DL (Goldenberg et al. 2019)

2 Hypothesis and Aims

To improve precision medicine and tailored prevention of prostate cancer, it is important to develop new ways of diagnosis. It is hypothesized that inflammatory processes change the cellular identities of epithelial or stroma cells, promoting prostate tumor development. Previous studies show that chronic inflammation of prostate-epithelial cells has a paracrine impact on stroma cells leading to a loss of smooth muscle cell function. We postulate that an advancement of histology can be achieved by integrating multispectral fluorescent-analysis to validate functional links between chronic inflammation and oncogene expression. The aim of this project is to establish new multifactorial image analyzing methods based on the expanded use of deep learning in collaboration with a company specialized on that (KML vision GmbH)

Until now it is not determined how the prostatic tissue architecture changes in response to inflammatory processes favoring tumor development. Or in addition, if inflammation is leading to cell identity changes in epithelial or stromal cells of the prostate.

Following Aims are formulated:

- Verify the differences regarding expression pattern of inflammatory and cancerous genotypes in the mouse prostate.
- Investigate the molecular correlation between inflammation and prostate cancer with the aid of multifactorial spectral scanning of several markers.
- Setup and optimization of multifactorial precision histology of prostate tissue samples based on fluorescence microscopy of multiple markers.
- Generating an image analysis tool for the quantitative evaluation of multispectral images.
- Development of advanced artificial intelligence algorithms by providing large images for automated genotype clustering and automated cell structure identity recognition.

3 Material and Methods

3.1 Chemicals and reagents

3.1.1 Cell culture reagents

- All prostate cancer-specific Cell-lines I used:
 - PC-3 (ATCC®CRL-1435™) → derived from metastatic site: bone, grade IV adenocarcinoma
 - LNCaP → derived from metastatic site: left supraclavicular lymph node, androgen-sensitive
 - V-Cap (ATCC®CRL-2876™) → vertebral metastasis, androgensensitive
 - DU-145 (ACC-261) → derived from metastatic site: brain
 - RWPE-1(ATCC®CRL-11609™) → not metastatic, infected with HPV-18

- Dulbecco's modified Eagle's medium (G418 500 µg/mL) -DMEM:
 - M199 (M5017, Sigma Aldrich, USA)
 - RPM1-1640 (R6504, Sigma Aldrich, USA)
 - DMEM/high glucose (D5648, Sigma Aldrich, USA)
 - HBS (CMFH-H2387, Sigma Aldrich, USA)
 - HBSS (H6136, Sigma Aldrich, USA)
 - DEMEM complete:
 - 10 % FBS (Fetal Bovine Serum, F7524, Sigma Aldrich, USA)
 - Pen/Strep/AmphB 100 µg/mL, (17-745E, Szabo-Scandic, Austria)
 - glutamine 2 mM (Lonza™ BioWhittaker™ L-Glutamine ,17-605F, Szabo-Scandic, Austria)
 - PBS: 8g NaCl(Sodium chloride, Roth, Germany), 1.44g Na₂HPO₄ (di-Sodium hydrogen phosphate, Sigma Aldrich, USA), 0.24g KH₂PO₄ (Kaliumdihydrogenphosphat, Merck, Germany), with AD to 1 L, pH adjustment with HCl (Titripur ®Hydrochloric acid, Merck, Germany) to pH 7.4
 - Trypsin/EDTA (Lonza™ BioWhittaker™ Trypsin Reagent, BE17-161E/12, Szabo-Scandic, Austria)

3.1.2 Reagents for Immunohistochemistry and H&E Staining

- Deparaffinization:
 - Xylol 100% (Xylol (Isomere), Roth, Germany)
 - Ethanol 99,9% (Ethanol Absolut 99,9% unvollständig vergällt, australco, Austria)
 - Ethanol 80%(Dilution with ddH₂O)
 - Ethanol 70%(Dilution with ddH₂O)
 - Ethanol 50% (Dilution with ddH₂O)
 - ddH₂O(MilliQ® Ultrapure Water Applications A10, Sigma Aldrich, USA)
- Antigen Retrieval:
 - pH6 citrate buffer: 200ml 27ml Solution A (0.1M citric acid Monohydrate, Sigma Aldrich, USA) 123ml Solution B (0.1M tri-Sodium citrate dihydrate, Merck, Germany) 1.5ml Tween 20 (TWEEN® 20, Sigma Aldrich, USA) add ddH₂O to 1.5 l, adjust to pH6
 - pH9 tris buffer (TRIS PUFFERAN® ≥99,9 %, p.a., Roth, Germany) adjust to pH9
- Permeabilization solution:

10xTBS: 60,50gTris+ 80g NaCl (Sodium chloride, Roth, Germany) add ddH₂O to 1l, adjust pH7,5

 - 1X TBS+ 0.1% Triton X-100 (Triton® X-100, serva, Germany)
- Washing solution:
 - 1X TBS + 0.1% Tween-20 (TBST)
- Blocking solution:
 - TBST + 1% BSA (Bovine Serum Albumin, PAN Biotech, Germany)
 - or + 10% FBS (Fetal Bovine Serum, Sigma Aldrich, USA)
- Eosin: 1:2 dillution of Eosin Y solution, Sigma Aldrich, USA
- Haematoxylin (Haematoxylin Solution, Harris Modified, Sigma Aldrich, USA)
- Mounting media for H&E: Organo/Limonene Mount™ (Sigma Aldrich, USA)
- Mounting Media: Mountant, PermaFluor, Thermo Scientific, USA

Following Ab were used

Inflammation marker:

- IKK2 (rabbit)
- IKK1(mouse, Alexa 546)
- RelA(mouse, Alexa 405)

- TNFa(mouse, Alexa 405)
- cancer marker:
- Myc(rabbit)P63(goat)
- PTEN (rabbit)PSMA (mouse, Alexa 594)
- AR (mouse, Alexa 488)
- CTK14 (mouse, Alexa 532)
- ERG(rabbit)
- Ki67 (mouse, DyLight 550)
- TF (mouse, Alexa 647)
- AMACR (mouse, Alexa 594)
- Secondary Ab:
- donkey anti rabbit 650
- chicken anti goat 488

All details including clonality, species, Tag, company can be found in the Attachment Table 3.

3.1.3 Reagents for RNA Isolation and qPCR

- PBS
- QIAzol ®Lysis Reagent (Qiagen, Netherlands)
- Chloroform (Chloroform, Sigma-Aldrich, USA)
- Isopropanol (2-Propanol, Sigma-Aldrich, USA)
- Ethanol 75 %
- nuclease free Water (Water, nuclease-free, Thermo Scientific, USA)
- RevertAid H Minus First Strand cDNA Synthesis Kit (Thermo Scientific, USA)
- SsoAdvanced Universal SYBR Green Supermix (Bio-Rad, USA)

Table 1: Primer list with Sequences and Size all primers are ordered from biomers.net

Target	Sequence FW	Sequence RV	Size [bp]
IKK1	GAAGGTGCAGTAACCCCTCA	ATTGCCCTGTTCTCATTG	
IKK2	GCTGCAACTGATGCTGATGT	TGTCACAGGGTAGGTGTGGA	
c-Myc	TCAAGAGGCGAACACACAAC	GGCCTTTTCATTGTTTTCCA	110
AR	GTGGAAGCTGCAAGGTCTTC	GGCGCACAGGTACTTCTGTT	62
RelA	GGCGAGAGGAGCACAGATAC	CCTGGTCCTGTGTAGCCATT	68
TF	CAGGAAAGAAAACAGCCAAA	GCCAGGATGATGACAAGGAT	
p53	ACCTATGGAACTACTTCTGAAAA	CCGGGGACAGCATCAAATCA	25
GAPDH	GTCTCCTCTGACTTCAACAGCG	ACCACCCTGTTGCTGTAGCCAA	

3.2 Material

3.2.1 Cell culture material

- 6-well plates (treated, non-treated)
- 12-well plates
- Pipette-boy
- Falcon tubes – 15 ml/50 ml (Sarstedt®)
- Thermo Scientific® Hood, MSc-Advantage
- Thermo Scientific® CO₂-Incubator (Heracell 150i)
- Eppendorf® 5424 Refrigerated Centrifuge
- Sigma® 4-16KS Centrifuge
- Light Microscope (TMS, Nikon)
- Smart fluorescent cell analyzer (JULI, Digital Bio)

3.2.2 Material for IHC

- Slides (Menzel-Gläser, Thermo Scientific, USA)
- Coverslip (24x50mm, Roth, Germany)
- 15µl Slide VI^{0.4} (Ibidi, Germany)
- Confocal Microscopy: Nikon A1 R+ laser scanning confocal system equipped with 12-bit detectors using a 20x plan objective (NA1.4). The donor channel was acquired with excitation at 405, 488, 561, and 640nm.
- Imaging Software (NIS-Elements, Nikon, Japan)

3.2.3 Material for qPCR

- PCR-Thermocycler (FlexCycler, Analytik Jena, Germany)
- StepOne™ Real-Time PCR System (Thermo Scientific, USA)

3.3 Methods

3.3.1 Mouse Models

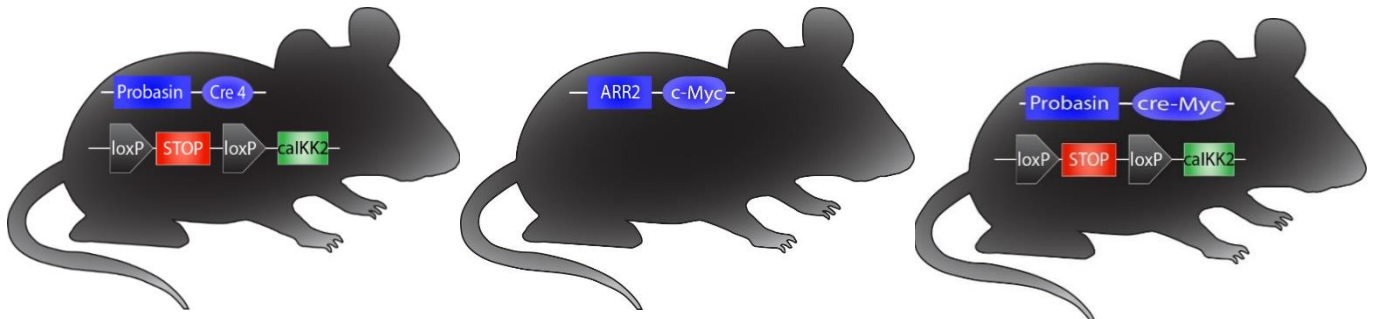


Figure 9: floxed calKK2 probasin cre, c-Myc and calKK2+c-Myc+ mouse model

To study gene function in vivo, gene knockout via the cre-loxP recombination system enables the conditional, cell type and tissue-specific gene deletion that is limited by the specificity and availability of the promoter (Wu et al. 2000). The PB-Cre4 line was generated to study tissue specific gene knockout in prostate epithelial cells. The ARR2PB consists of a proximal element rat Probasin (PB) promoter and is comprised with two androgen responsive regions (ARR) (Wu et al. 2000).

All mice were kept on a C57BL/6JHim background from the cohort of the Medical University of Vienna at Himberg, Austria (Birbach 2013).

Transgenic expression of constitutively active mutant IKK2 (calKK2) achieved via glutamic acid replacement of the two serine residues of the activation loop offers a powerful tool to activate NF- κ B in a cell-autonomous and stimulation-independent manner (Pasparakis et al. 2006). Human MYC gene expressed as a transgene is used as initiating event for the development of murine PIN followed by invasive adenocarcinoma in mouse prostates. These tumors share molecular similarities with human prostate cancer for preclinical studies (Ellwood-Yen et al. 2003).

We used cre+, myc+ and cre,myc+ mice for the evaluation of both transgenic modifications (calKK2 and c-Myc) as well as wild types for comparison.

3.3.2 Immunohistochemistry

Prepared paraffin embedded mouse prostates, that were sectioned via microtome slicing were already available. For deparaffinization, the slides were put in a dry heating oven at 80-90°C until the paraffin started melting. Afterwards, the slides were put two times for 5 min in xylene. Rehydration took place with following alcohol gradients: 100%, 96%, 70%, 50% and ddH₂O for 5min each. The slides were put for 5min under cold running tap water before they were cooked for 10 minutes in either pH6 citrate buffer or pH9 tris buffer to retrieve the antigen-epitopes. Then the beaker was taken off the cooking plate and slides were left to rest in the warm buffer for 30min. To permeabilize the cells, the slides were put in permeabilization solution for 10min at RT followed by three 5min wash cycles in washing solution. Then the tissue was circled with DAKO pen and blocking solution was carefully dropped onto the tissue and let incubate for 120 min at RT. After draining the slides, 150 µl of primary antibody diluted in blocking solution was applied and incubated over night at 4 °C. Different concentrations were tested, the final ones are listed in table 3. At day two, the slides were washed three times 5 minutes in washing solution and 150 µl of the conjugated secondary antibody diluted in blocking solution was incubated for 60 min at RT. After removing the antibody solution by washing the slides three times for 5 min, counterstaining with DAPI (1 µg/ml) was performed for 7 min. Again, the slides were washed three times for 5 min in washing solution. Then 1 drop of mounting medium was added and covered with a slip. The excess mounting medium was carefully removed with a tissue and sealed with nail polish for conservation.

Due to the lack of real negative controls, as IKK1,2 or Myc knockouts are not possible and positive controls are not available, we just make secondary Ab only controls to show the specificity to the primary Ab. Typically antibody specificity is also tested via western blot which is not shown in this thesis.

3.3.3 Microscopy

For imaging the NIS-Elements AR 5.02.01 Software from Nikon was used. Antibody Optimization large Images were acquired in Galvano mode with a scan size of 1024x1204 pixel, a scan speed of 0.5 frame/sec and a line averaging count of four.

To select three regions of interest for spectral scan, first a large image only with DAPI was performed. Then a spectral scan including all four lasers with a resolution of 10.0 and following channel numbers:

405 Channels 32, Wavelength 415-735

488 Channels 24 Wavelength 495-735

561 Channels 15 Wavelength 585-735

640 Channel 8 Wavelength 655-735

has been done with ND sequence acquisition capturing.

For the establishment of pure Spectra, pure Antibodies were diluted in PBS to their optimal concentration and transfer it in a 15 µl Slide. The focus was set on the transition between the liquid-tunnel and the slide and a spectral scan was done.

3.3.4 Haematoxylin-Eosin staining (H&E staining), IKOSA®

To remove the paraffin, slides were stored in an 80 °C dry oven for 5 min. Two changes of xylene, 10 min each were performed for deparaffinization. Xylene was washed out in two changes of absolute alcohol, 5 min each. Slides were then transferred to 95% and 70% alcohol and pure water for 2 minutes each to rehydrate the samples. After rehydration, the staining was performed for 5 minutes in Mayer Haematoxylin solution. The slides were rinsed in 95 % ethanol for 10 dips. They were counterstained with Eosin Y solution for 3 min and dehydrated 5 min in 95 % and in absolute ethanol. For clearing, the slides were put in xylene for 5 min. Finally, the slides were coverslipped with a xylene-based mounting medium.

The slides were imaged and uploaded to the IKOSA® platform. The IKOSA® platform is a website, that provide automated image analysis for illustrations of clinical relevance hosted by KML Vision. For genotype clustering and the distinction of all four mouse prostate lobes, we annotated our uploaded images according to the characteristics find in the results Table 2.

3.3.5 Cell Culture Work

After thawing the cells, they were transferred in a T175 flask with prewarmed media and incubated at 37°C. Media has been changed 2 times. To split the cells the medium was discarded, and the cells were washed with PBS. Trypsin was added and incubated for about 5 minutes. Then they were transfered in a tube with PBS and Media for 5min 300 x g centrifugation. In a last step the cells were split 1:1 and kept in Media in a T175 flask.

3.3.6 RNA Isolation and qPCR

Cells were split and expanded in a T175 cell culture flask. After sucking the media the cells were first washed with PBS and then diluted in 15 ml PBS. With the aid of a cell scraper, the adherent cells were removed and transferred in a tube for 5 min 2000 x g centrifugation. The pellet was dissolved in 1 ml PBS and divided in two 2 ml Eppendorf tubes 0,5 ml each. All Eppendorf tubes were centrifuged at 10.000 x g for 3 min. For RNA isolation the pellet in the 2 ml Epi was resuspended in 1 ml Qiazol. 100 µl Laemmli buffer was added to the cells in the 2 ml Epi and stored at -20 °C for western blotting a week later.

0,2 ml of Chloroform were added to the Qiazol nucleoprotein solution, which separated the mixture into a lower red phenol-chloroform, a interphase, and a colorless upper aqueous phase. The samples were centrifuged 15 min at 12.000 x g at 4 °C and the aqueous phase containing the RNA was transferred in a new Eppendorf tube. RNA precipitation was done by adding 0,5 ml Isopropanol to the aqueous phase and incubating it for 10 min at RT. The supernatant was discarded after 10 min 12.000 x g at 4°C centrifugation. The pellet was resuspended in 1 ml 75 % Ethanol vortexed and centrifuged 5 min 7500 x g at 4°C. After 10 min pellet air drying, it was resuspended in 20-50µl rnase free water and incubated for 10 min at 60 °C on a heat block.

The concentration of isolated RNA was measured with Nanodrop for equal cDNA synthesis. RNA was reverted to cDNA following the instruction of the RevertAid H Minus First Strand cDNA Synthesis Kit.

After diluting the Primers 1:10 qPCR was prepared according to SsoAdvanced Universal SYBR Green Supermix manual and measured with StepOne™ Real-Time PCR System.

4 Results

4.1 Optimization of Fluorescence Antibodies

We tested a group of candidate molecular markers related to various cell regulation pathways that are of prognostic interest in prostate cancer investigation in our calKK2+, myc+, calKK2+myc+ as well as wild type mice. Therefore, we started by optimizing the antibody concentrations in two different antigen retrieval buffers (Citrate buffer pH=6, Tris/EDTA Buffer pH=9). On the following pages the results of the tested antibodies are shown and compared to the proteinaatlas database www.proteinatlas.org (last access: 14th April between 1 to 3 pm).

Myc

Unlabelled Ab: c-Myc/N-Myc (D3N8F) Rabbit mAb #13987 recognizes endogenous levels of total c-Myc and N-Myc proteins in Human, Mouse, Rat and Monkey species.

Secondary AB: Donkey Anti-Rabbit IgG H&L (DyLight® 650) preadsorbed (ab96922)

In our mouse model c-Myc is overexpressed in basal cells of the prostate which leads to the increased expression of many genes involved in cell proliferation contributing to the formation of cancer.

The pH6 buffer was the buffer in which the stain worked out a little bit better. Because of the usage of a secondary antibody the concentration was chosen very high (1:1500) but with a dilution of (1:1000) the signal acquisition was better. We observed a cytoplasmic signal in the basal layer, which is in line with the expectations compared to proteinatlas. As typical cancer marker this Ab was used further in the multiplex staining.

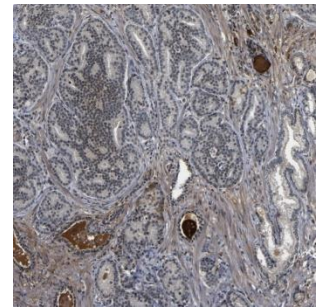
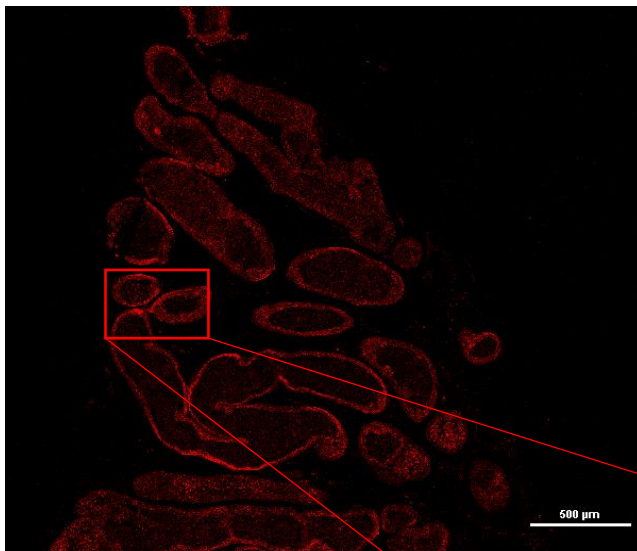


Figure10:
<https://www.proteinatlas.org/ENSG00000136997-MYC/pathology/prostate+cancer#img> shows the myc expression in the basal layer as well as in some ducts

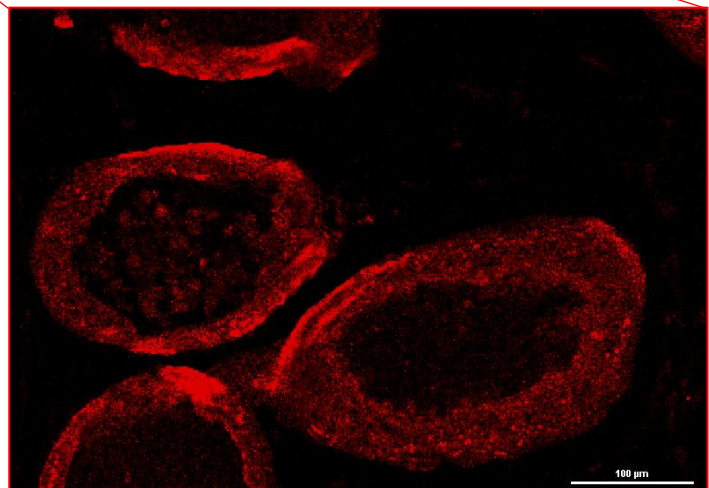


Figure 11: myc+, pH6, 1:1000 → we can see c-myc that is clearly expressed in the basal layer

IKK2

Unlabelled Ab: IKK2 (D30C6) Rabbit mAb #8943 recognized endogenous levels of total IKK2 and does not cross-react with other IKK family members.

Secondary AB: Donkey Anti-Rabbit IgG H&L (DyLight® 650) preadsorbed (ab96922)

As mentioned above our mouse model overexpresses IKK2 which is part of the IKK complex playing a central role in the NFκB-pathway.

As expected, we see the typical mosaic expression in the cytoplasm of epithelial cells in calKK2 positive mice. Despite to the Myc Ab the pH9 buffer functioned better and the Ab requires a smaller concentration. Confirmed with the proteintlas the expression can be seen in the cytoplasm of the epithelial cells, therefore this Ab was also used in the multiplexing staining.

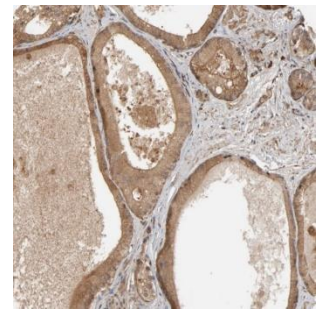
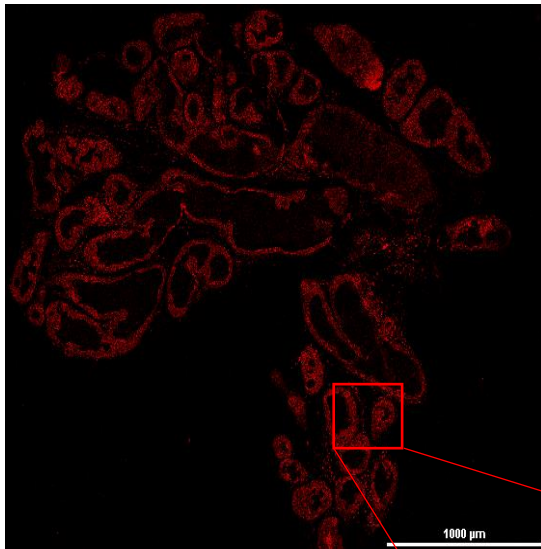


Figure12:
<https://www.proteinatlas.org/ENSG00000104365-IKBKB/pathology/prostate+cancer#img> show IKK2 expression in the epithelial cells, but also small amounts in the stroma

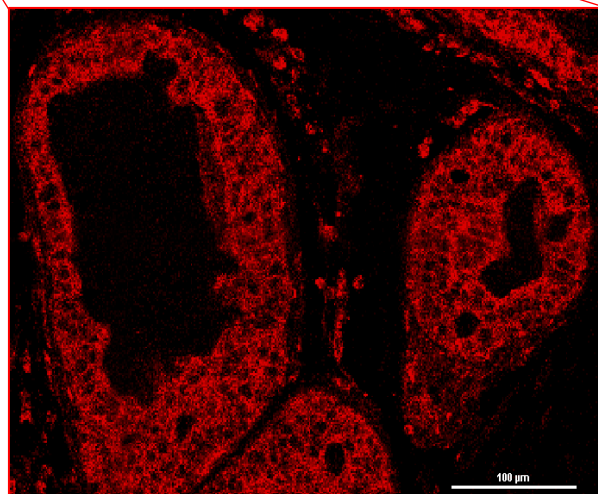
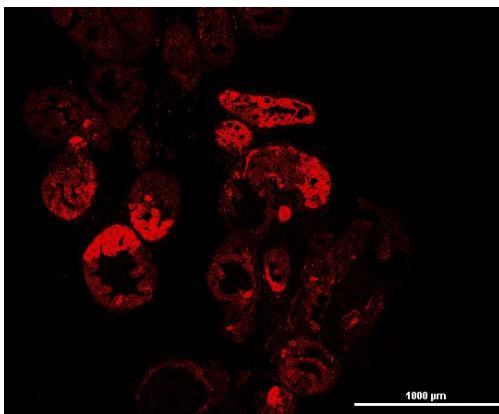


Figure 13: myc+, pH9, 1:500 → left you see the mosaic expression in calKK2+myc+ mice compared to myc+

IKK1

Labelled Ab: IKK alpha Antibody (B-8) [Alexa 546] monoclonal mouse Ab was raised against a His-tagged full-length human IKK1 protein.

IKK1 phosphorylates sites that trigger degradation via ubiquitination of transcription factor NFkB inhibitor, thereby activating the transcription factor.

This Ab which is clearly expressed in the epithelial cells seen in Figure 15, but as primary Ab it requires a high concentration. A dilution of 1:50 worked best with pH9 buffer. The IKK1 Ab has also qualified for the multiplexing staining.

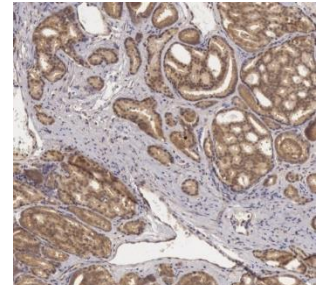
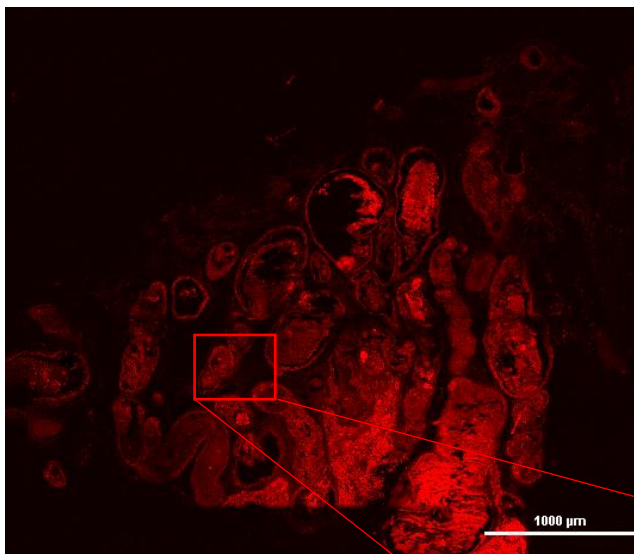


Figure14:
<https://www.proteinatlas.org/ENSG00000213341-CHUK/pathology/prostate+cancer#img> especially the epithelial cells are stained

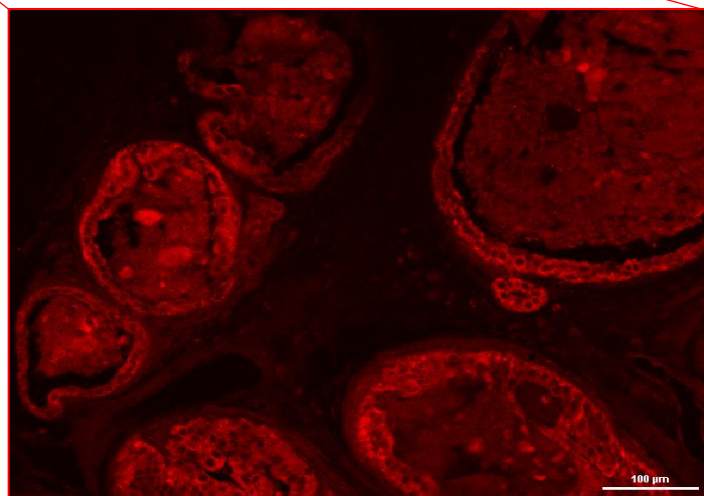


Figure 15: calKK2+myc+, pH9, 1:50 → we see the high abundance in the epithelial cells

CTK14

Labelled Ab: Cytokeratin 14 Antibody (KRT14/532) [Alexa Fluor® 532] mouse monoclonal Ab represents a squamous cell marker.

CTK14 belongs to the type 1 subfamily of low molecular weight keratins and is found in basal cells of squamous epithelia cells. CTK14 Ab is used to distinguish squamous cell carcinoma from poorly differentiated epithelial tumor or intraductal from invasive carcinoma or benign prostate from prostate cancer.

We observed the expected epithelial cytoplasmic signal, but also troubled with the background, which was better in pH9 and needed high concentrations. Because we had no typical invasive carcinoma mice, just Myc+, we lacked comparison. Therefore, we did not choose this Ab for the multistaining.

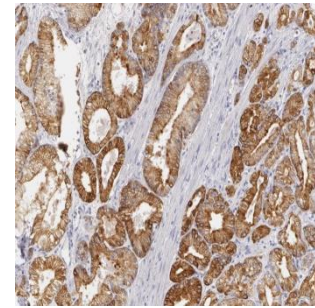
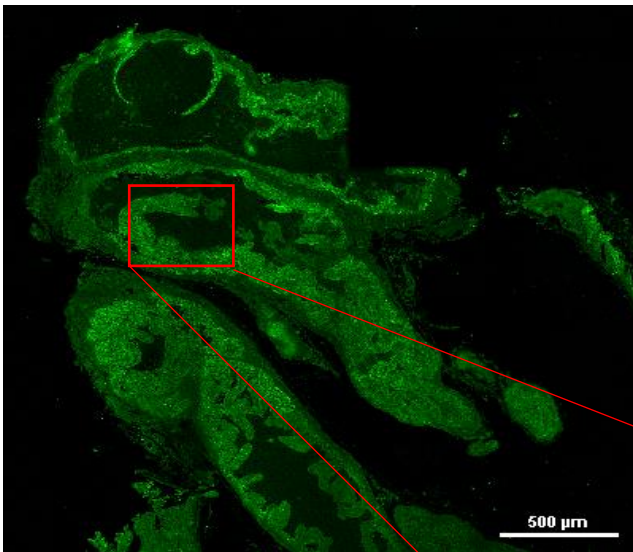


Figure16:
<https://www.proteinatlas.org/ENSG00000186847-KRT14/pathology/prostate+cancer#img> there is strong cytoplasmic immunoreactivity in squamous cell carcinomas compared to benign tissues

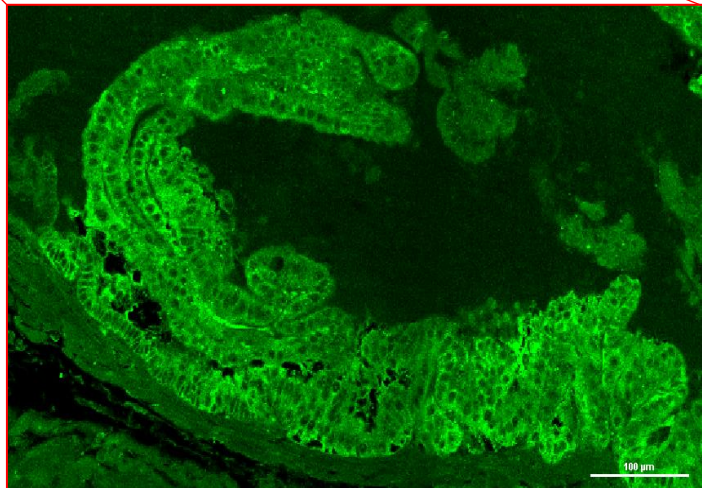


Figure 17: myc+, pH9, 1:50 → we see the green fluorescence of CTK14 in the epithelial cell layer

p63

Unlabelled Ab: p63/TP73L Antibody [Unconjugated] polyclonal goat Ab detects human p63 (TP63, p40, p51 or KET) is p53 homolog.

Secondary Ab: Chicken anti-Goat IgG (H+L) Cross-Adsorbed Secondary Antibody, Alexa Fluor 488. P63 is highly expressed in many epithelial tissues in the adult and play a role in epithelial cell maintenance and tumorigenesis. p63^{-/-} mice do not develop the prostate properly and p63 is not found in adenocarcinomas.

The p63 Ab stained not as expected. The typical nucleolar basal cell signals could not really be seen, only epithelial cytoplasm in both buffers, where pH6 was a little bit better. Despite of the tumorigenic functions of p63, we did not used it in our multistain.

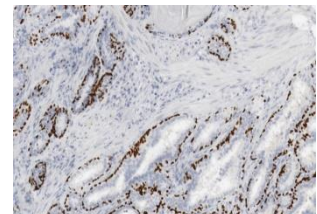
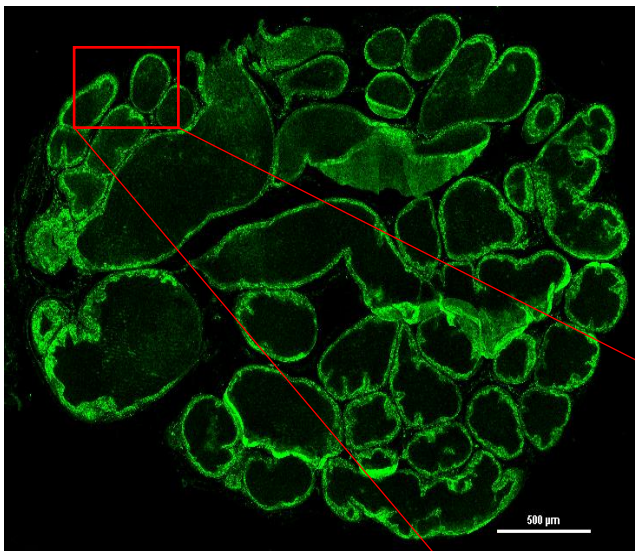


Figure 18:
<https://www.proteinatlas.org/ENSG00000073282-TP63/pathology/prostate+cancer#img> show the expression in the nuclei of basal regenerative cells of epithelial tissue

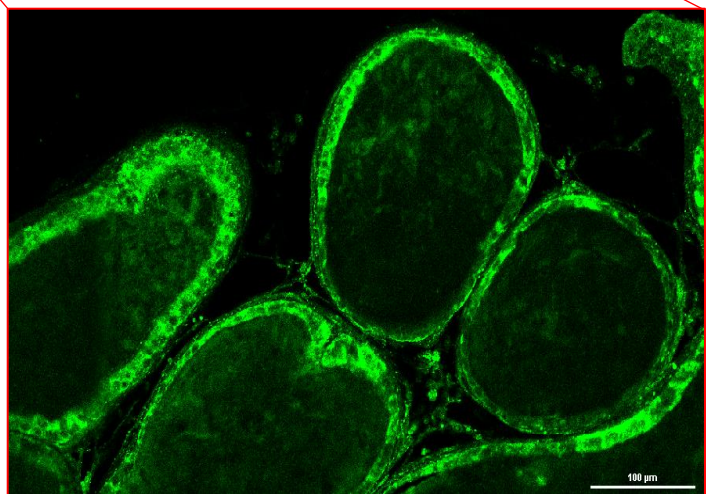


Figure 19: upper: myc+, pH6, 1:10 → we did not observe the nuclear staining in basal cells

PTEN

Unlabelled Ab: PTEN (138G6) Rabbit mAb #9559 detects endogenous levels of total PTEN protein in Human, Mouse, Rat and Monkey.

Secondary Ab: Donkey Anti-Rabbit IgG H&L (DyLight® 650) preadsorbed (ab96922)

Phosphatase and tensin homologue deleted on chromosome ten is a tumour suppressor implicated in a wide variety of human cancers (in 70% of prostate cancer PTEN is lost). It negatively regulates the PI3K/Akt signalling pathway as well as p53 protein levels and activity leading to increased cell proliferation and decreased cell death.

We observed the typical nuclei spacing in epithelial cells consistent with the proteinaatlas, better in the pH9 than pH6 buffer. Unfortunately we can use only one anti-rabbit secondary Ab, therefore PTEN was not used for the multistaining.

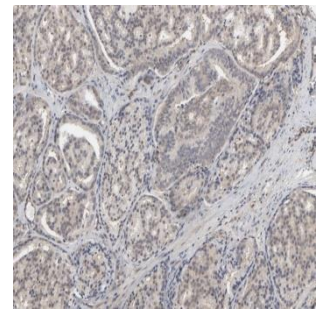
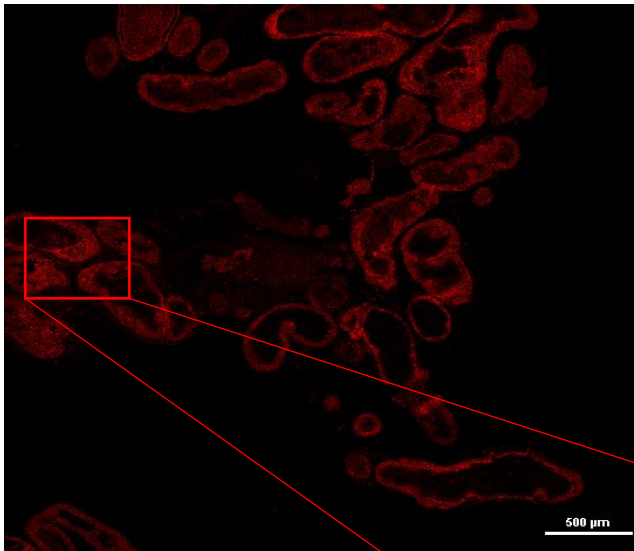


Figure21:
<https://www.proteinatlas.org/ENSG00000171862-PTEN/pathology/prostate+cancer#img> show low PTEN abundance in epithelial cells spacing the nuclei

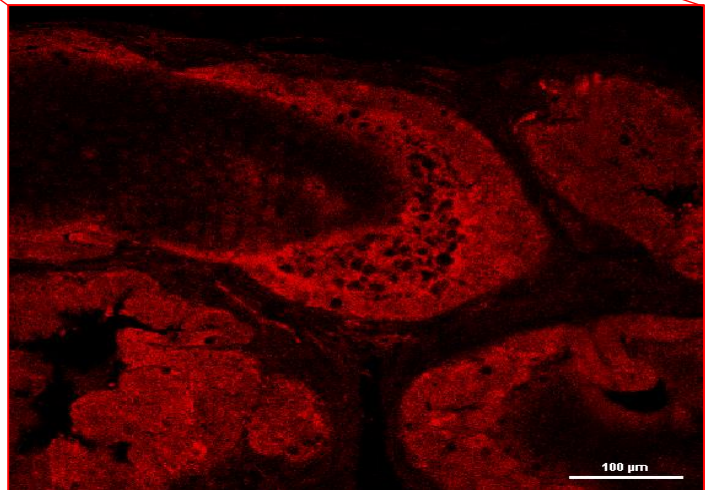


Figure 20: myc+ pH9, 1:200 → the PTEN expression is clearly seen around the epithelial nuclei

ERG

Unlabelled Ab: ERG (A7L1G) Rabbit mAb #97249 recognized endogenous levels of total ERG protein. It should detect isoforms (ERG1, ERG2 and ERG3) and do not cross react with Fil1.

Secondary Ab: Donkey Anti-Rabbit IgG H&L (DyLight® 650) preadsorbed (ab96922)

The ERG gene belongs to the transcription factor erythroblast transformation-specific (ETS) family playing a role in embryonic development, cell proliferation, hematopoiesis and many others. Proteins that are encoded by this gene are required for platelet adhesion to the sub endothelium mainly expressed in the nucleus. The TMPSSR2-ERG fusion gene product is associated with prostate cancer.

The heterogeneous expression seen in Figure 23 was not recognized or just in marginal amounts. But interestingly, the surrounding blood vessels can be seen very good. We did not use this Ab for multistaining experiments.

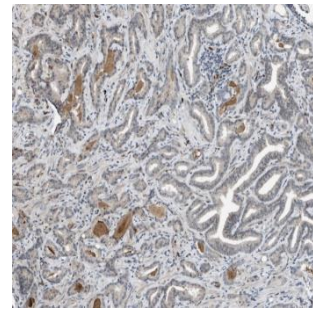
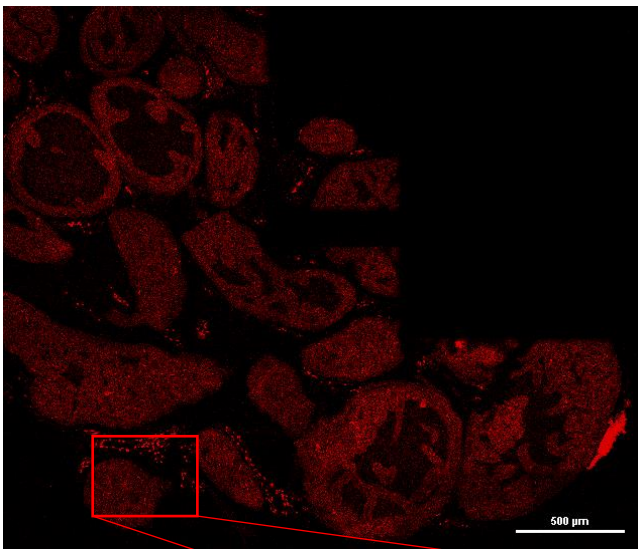


Figure23:
<https://www.proteinatlas.org/ENSG00000157554-ERG/pathology/prostate+cancer#img> show the heterogeneous expression of ERG through the tissue

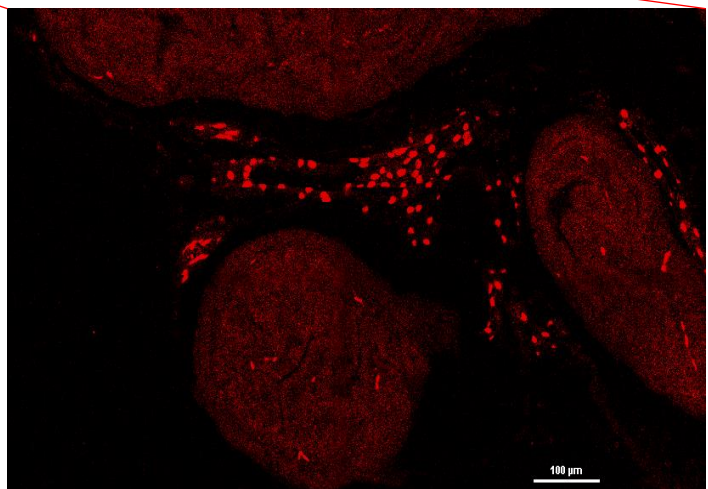


Figure 22: In ERG positive mice ERG seems to associate the blood vessel within the stroma seen in light red

AR

Labelled Ab: Anti-Androgen Receptor Antibody, (441) Mouse, monoclonal [Alexa 488] for detection of Androgen Receptor also known as Dihydrotestosterone Receptor. The DNA binding transcription factor, androgen receptor activated by steroid-hormones regulate gene expression and have additional functions independent of DNA binding. After binding the hormone, the receptor translocates in the nucleus, dimerizes and stimulates transcription of androgen responsive genes. Mutations of these genes are associated with complete androgen insensitivity.

In wild type as well as *calkk2+Myc+* mice, we did not observe the nuclear expression seen in Figure 25 in both buffers as well as with even higher concentrations. However, we decided to include the AR antibody in the multispectral staining, to see if these effects can also be seen in a large amount of all genotypes, because of its role in Pca and it fits in our spectral composition so it would not disturb the staining.

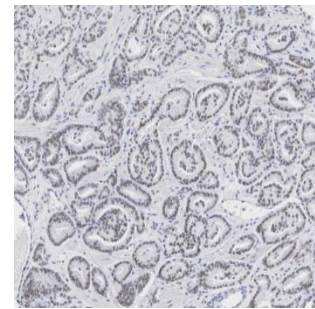
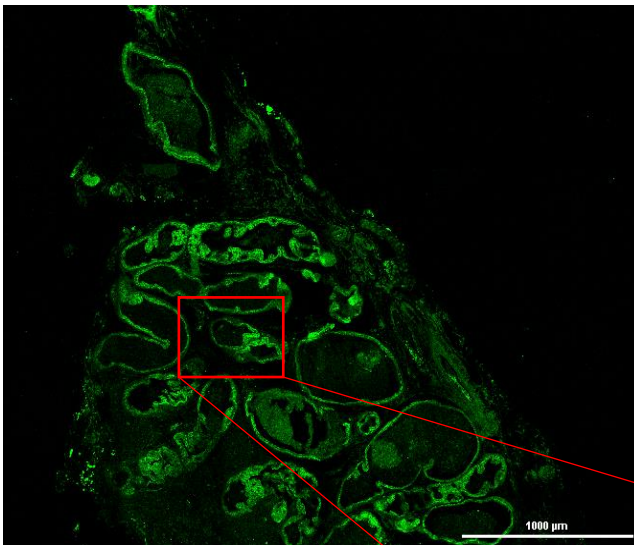


Figure25:
<https://www.proteinatlas.org/ENSG00000169083-AR/pathology/prostate+cancer#img> show clearly the AR expression in the nucleus

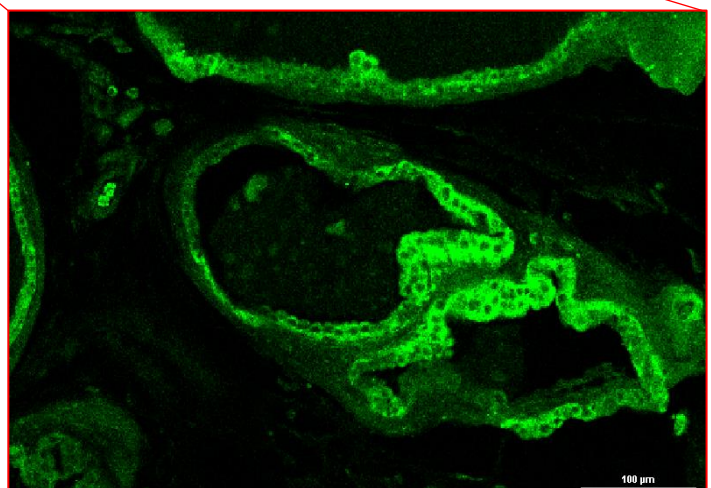


Figure 24: *calKK2+myc+*, pH6, 1:50 → the nuclear expression can not be seen

PSMA

Labelled Ab: PSMA/FOLH1/NAALADase I Antibody (GCP-04) [Alexa Fluor® 594] monoclonal mouse Ab recognizes amino acids 100-104 of extracellular domain of denatured glutamate carboxypeptidase II a transmembrane glycoprotein.

PSMA represents in some prostate cancers the second most upregulated gene product.

In pH6 the cytoplasmic epithelial cell expression was seen better than in pH9. We started with a high concentration (1:20) but had lower background with the 1:100 dilution. The PSMA Ab was not used in the multistaining.

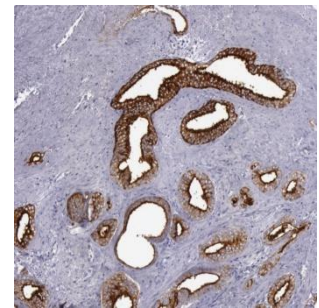
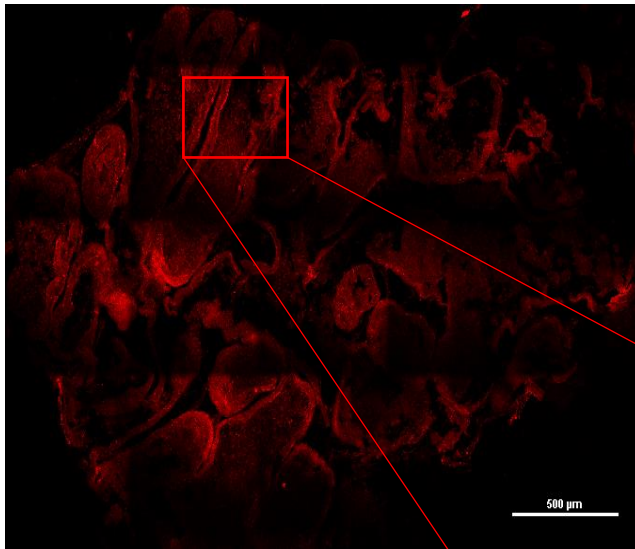


Figure26:
<https://www.proteinatlas.org/ENSG00000086205-FOLH1/pathology/prostate+cancer#img> show epithelial cell expression of PSMA

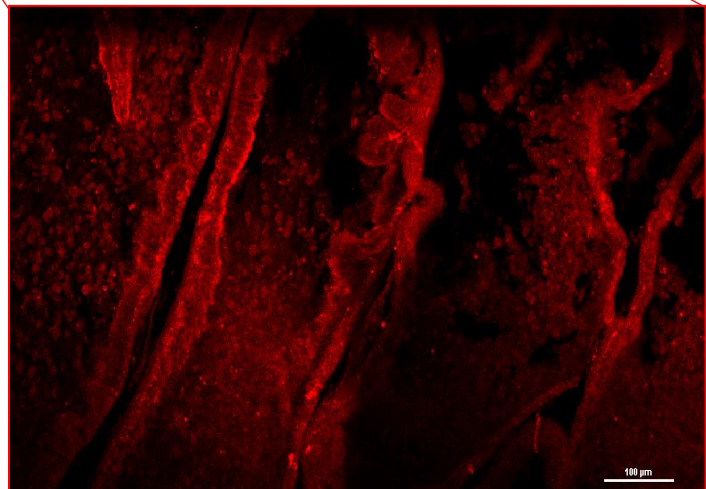


Figure 27: myc+, pH 6, 1:100 → the epithelial expression is clearly seen

Ki67

Labelled Ab: Ki67/MKI67 Antibody (8D5) [DyLight 550] monoclonal mouse Ab detection by immunostaining is commonly used as proliferation marker in solid tumours.

It specifically labels the nuclei and chromosomes of cells actively undergoing proliferation but is not detected in cells that are in resting G0-phase. In certain cancer types it is used to assess the proliferative activity, which may be a measure of aggressiveness.

Compared to Figure 29 we did not observe the proliferating nuclei in any tissue we tested, in both buffers and also not with a higher concentration. Because of its unspecificity we did not include Ki67 for the multistains.

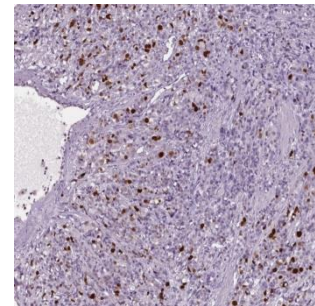


Figure28:

<https://www.proteinatlas.org/ENSG00000148773-MKI67/pathology/prostate+cancer#img> show the specifically labelled proliferating nuclei

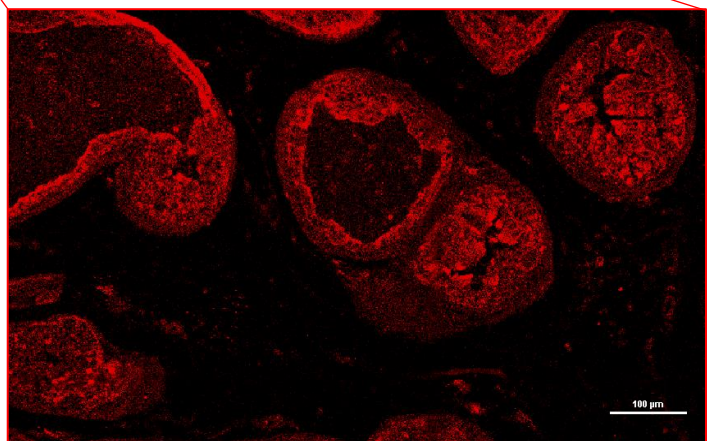


Figure 29: Myc+, pH9, 1:500 → the proliferating nuclei can not be seen maybe due to lack of cancerous tissue

RELA (p65)

Labelled Ab: RelA/NFkB p65 Antibody (112A1021) [Alexa Fluor® 405] monoclonal mouse Ab was raised against a synthetic peptide corresponding to amino acids 526-539 of human NF-kB protein.

There is association found between RELA nuclear localisation and prostate cancer aggressiveness and biochemical recurrence.

RelA worked out the way it was expected also compared to proteinatlas. We see the cytoplasmic expression in epithelial and stromal cells and could clearly discriminate between the DAPI and the RelA signal in both buffers and in low concentrations. Therefore, we included RelA to our multistaining.

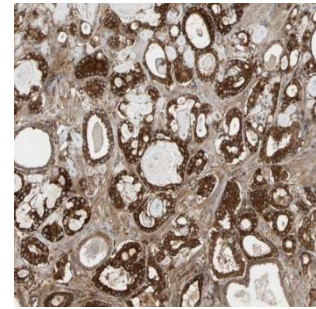
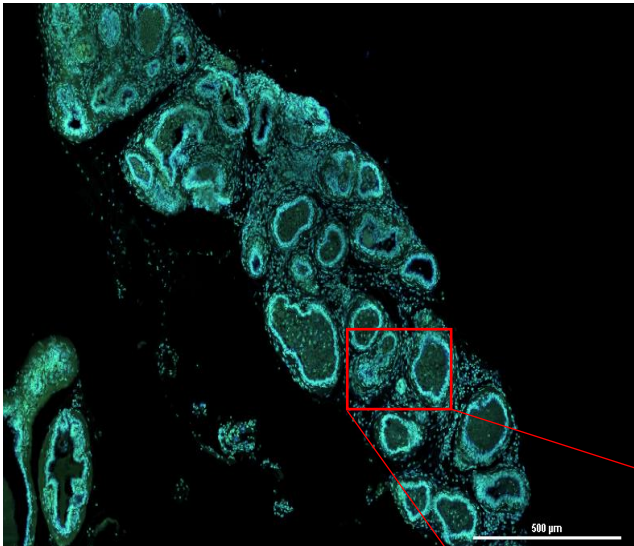


Figure30:
<https://www.proteinatlas.org/ENSG00000173039-RELA/pathology/prostate+cancer#img> show strong cytoplasmic immunoreactivity

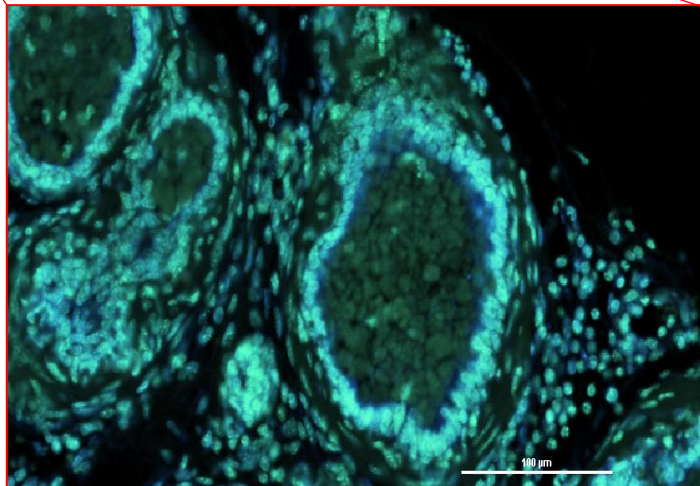


Figure 31: Myc+, pH9 1:1000 → The clearly seen difference between Dapi (dark blue) and RelA (light green), (this is a spectral scan to see the difference)

TF

Labelled Ab: Tissue Factor/CD142 (H-9) Mouse monoclonal [Alexa 647] Antibody recognizes endogenous levels of total Tissue Factor /CD142 protein. Tissue Factor (Coagulation factor III/Thromboplastin) is a type-I transmembrane glycoprotein that serves as the cell surface receptor and cofactor for blood coagulation factors VII and VIIa playing a key role in hemostasis and thrombosis. TF is implicated in pathologic conditions such as tumour growth, tumour angiogenesis, metastasis and associated with numerous types of solid cancers.

In pH6 this Ab stained better and required only low concentrations. In accordance with the proteinatlas we see the heterogeneous expression mostly in the epithelial cells.

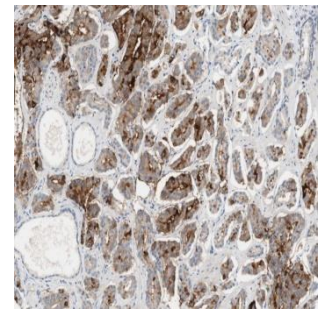
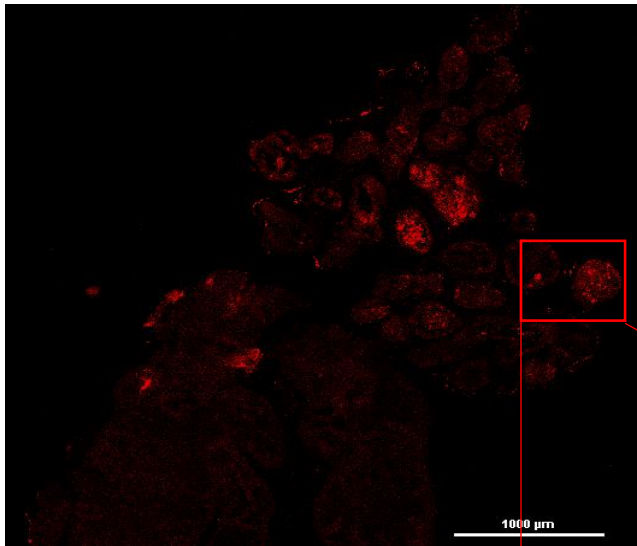


Figure32:
<https://www.proteinatlas.org/ENSG00000117525-F3/pathology/prostate+cancer#img> show highly heterogeneous expression through the tissue

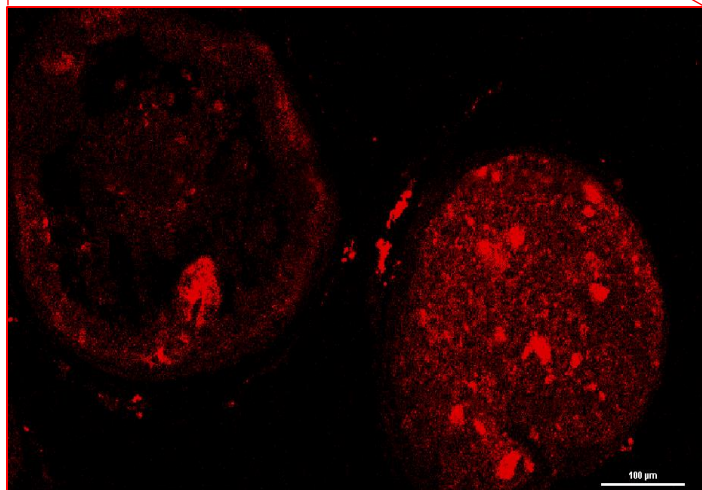


Figure 33: calKK2+myc+, pH6, 1:500 → we see the heterogeneous expression through the tissue

AMACR

Labelled Ab: alpha-Methylacyl-CoA Racemase/AMACR Antibody (OT15F10) [Alexa Fluor® 594] monoclonal mouse Ab.

Alpha-methylacyl- CoA reacebase(AMACR) converts (2R)-methylacyl-CoA esters to their (2S)-methylacyl-CoA epimers and known substrates. This enzyme is widely used as biomarker due to its increased protein concentration and activity in cancer biopsy tissues.

This Ab showed high background in every concentration and buffer. We got a small amount of signal but not high and specific enough, compared to proteinatlas. We did not include this Ab in the multistains also because of spectral interfering issues.

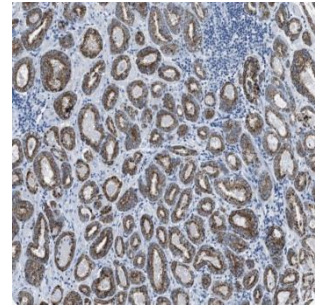
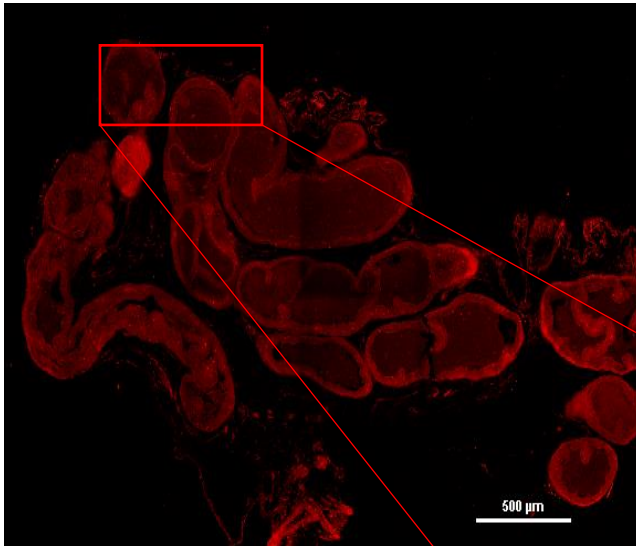


Figure34:
<https://www.proteinatlas.org/ENSG00000242110-AMACR/pathology/prostate+cancer#img> show the high abundance in carcinomas

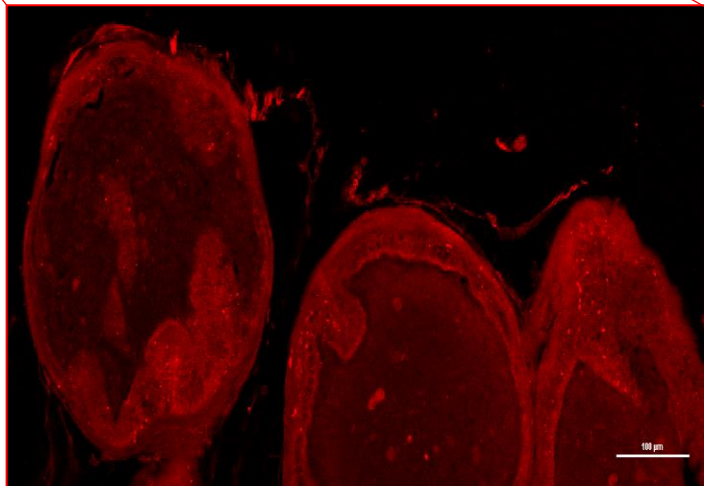


Figure 35: myc+, pH9, 1:20 → AMACR is expressed only in certain tumours, which makes it hard to get a positive control, we see high background

TNF α

Labelled Ab: TNF α (C-4) [Alexa Fluor® 594] monoclonal mouse Ab

TNF α is involved in the regulation of many biological processes including immune and inflammatory functions by binding to its receptors TNFRSF1A/TNFR1 and TNFRSF1B/TNFR2. A suggested neuroprotective function as well as the implication in a wide spectrum of diseases like autoimmune disease, insulin resistance and cancer make it an interesting cytokine.

For this Ab we needed higher concentrations but it showed the expected expression in epithelial and nuclear regions in both buffers. Because of its function in NF- κ B signaling we decided to include TNF α Ab to our multistain.

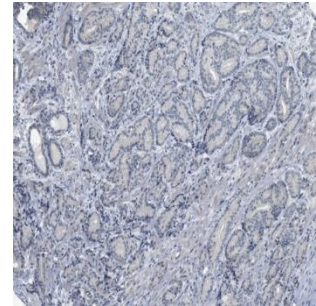
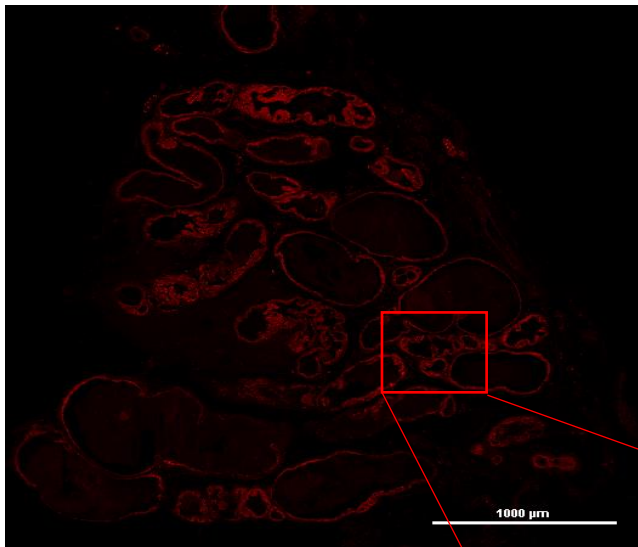


Figure36:
<https://www.proteinatlas.org/ENSG00000109079-TNFAIP1/pathology/prostate+cancer#img> show expression in cytoplasmic/ membranous tissue

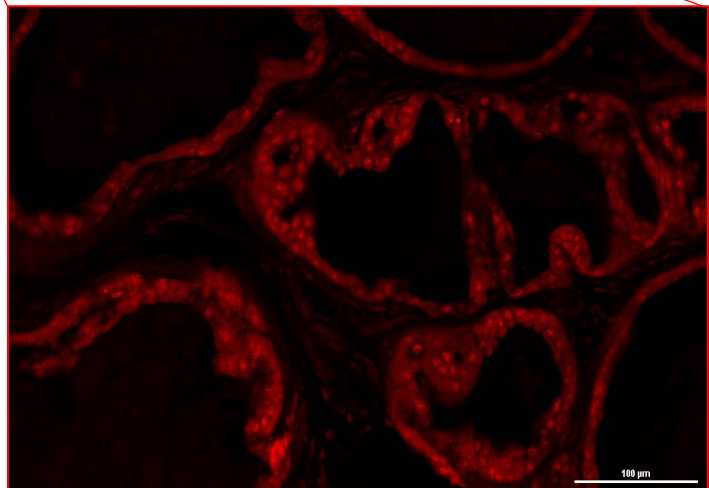


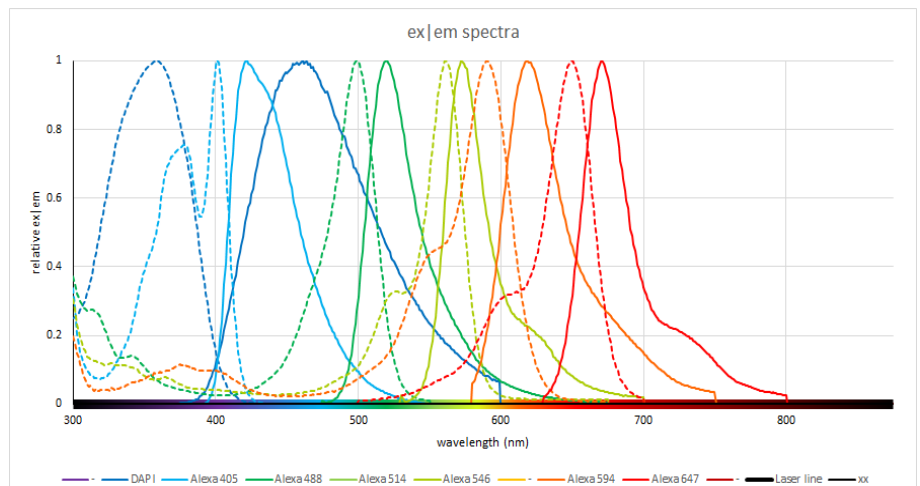
Figure 37: calKK2+myc+, pH6, 1:50 → we see the expression in epithelial cells as well as the nuclei

4.2 Fluorescence Multi- staining Quantification

We decided to primarily concentrate on the NF κ B pathway, therefore we chose targets that are relevant within this inflammatory pathway shown in Multistain 1. Additionally, we wanted to see the differences or correlations of cancer and inflammation by selecting the two most typical markers seen in Multistain 2. Earlier experiments already hinted at a correlation of IKK1 and c-Myc which we also wanted to investigate here. To distinguish between a cancerous and inflammatory phenotype we analyzed all four Genotypes with a sample size of five in two different multi-stains.

Multistain 1:

- DAPI(405)
- RelA(405)
- AR(488)
- IKK1(546)
- TNFa(594)
- IKK2(650)



Multistain 2:

- DAPI
- IKK1 (546 nm)
- c-Myc(650 nm)

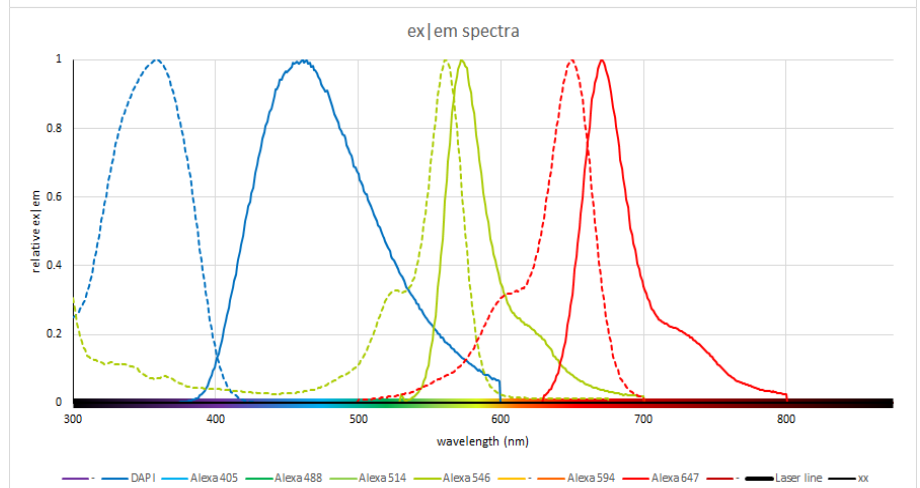


Figure 38: excitation and emission spectra of Multistain 1 and 2

Because of laser-pixel-shifting whole slide scans were not possible. Therefore, we decided to make a whole slide scan in bad resolution with DAPI only and capture three regions of interest.

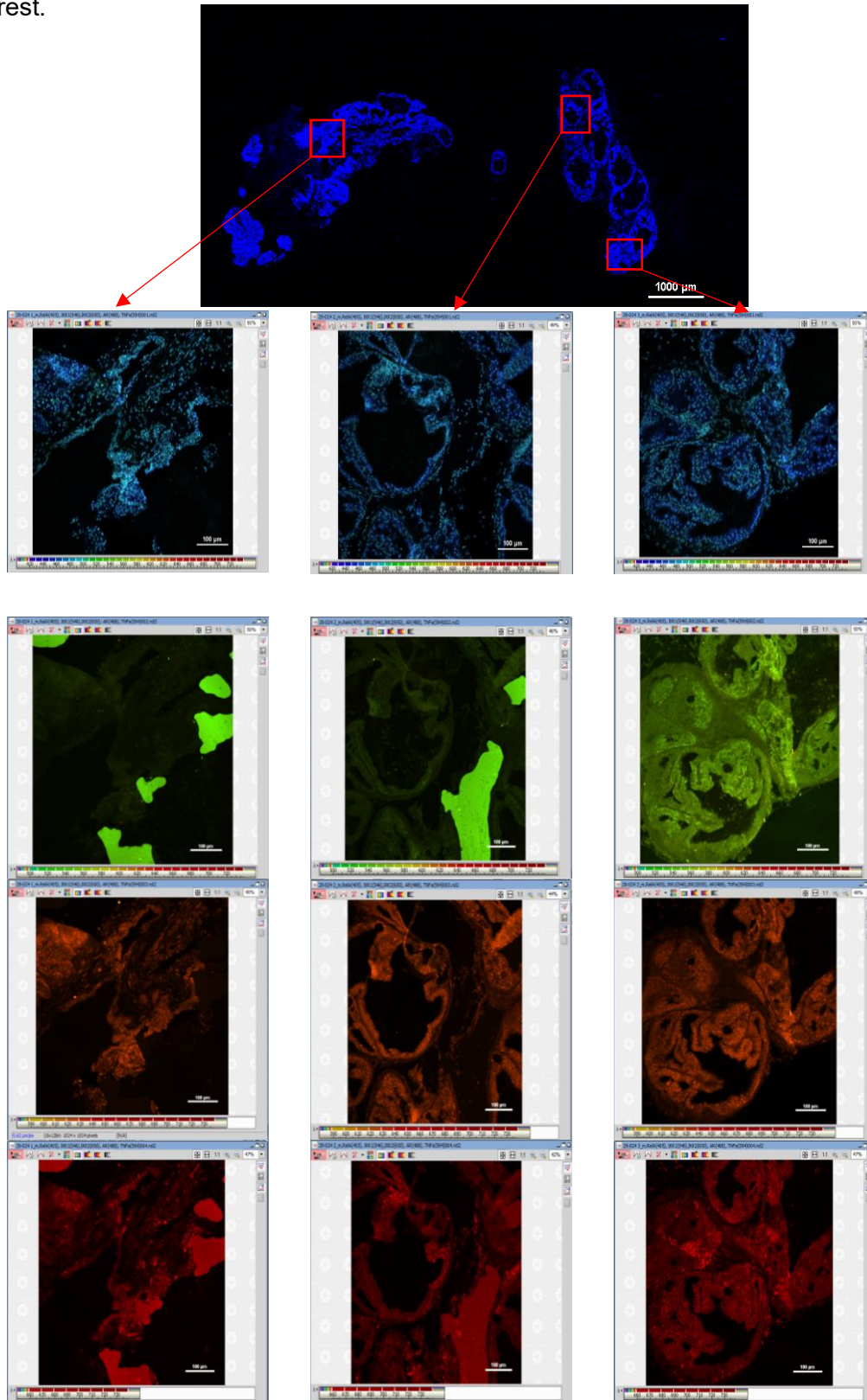


Figure 39: At the top you see the whole slide scan with the DAPI channel. Then a selection of three ROIs for spectral scan capturing of a myc+ sample. All four lasers give a lambda stack with different numbers of channels. Thereby we generate 12 spectral scans for one multistain on one slide.

4.2.1 Image Analysis in ImageJ

First the spectral scanned Images had to be combined (Macro: stack combiner). Therefore, the 4 different channel pictures were stacked together. To deconvolute our images composed of multiple fluorescent signals we used the Spectral_Unmixing ImageJ Plugin from Seth Gammon, which originally is used for simultaneous measuring of multiple bioluminescence reporters. Filtered images with individual components comprising a composite image were quantified and separated via a set of linear equations. This algorithm makes spectral unmixing amenable for a standard laboratory assay.

For quantification we developed specialized macros that detect nuclear and cytosolic regions of the prostate epithelium on the basis of threshold adjustment, followed by analyzing the intensities to measure signal of the whole region, nuclei and cytosol. All macros can be found in the attachment page 3-10.

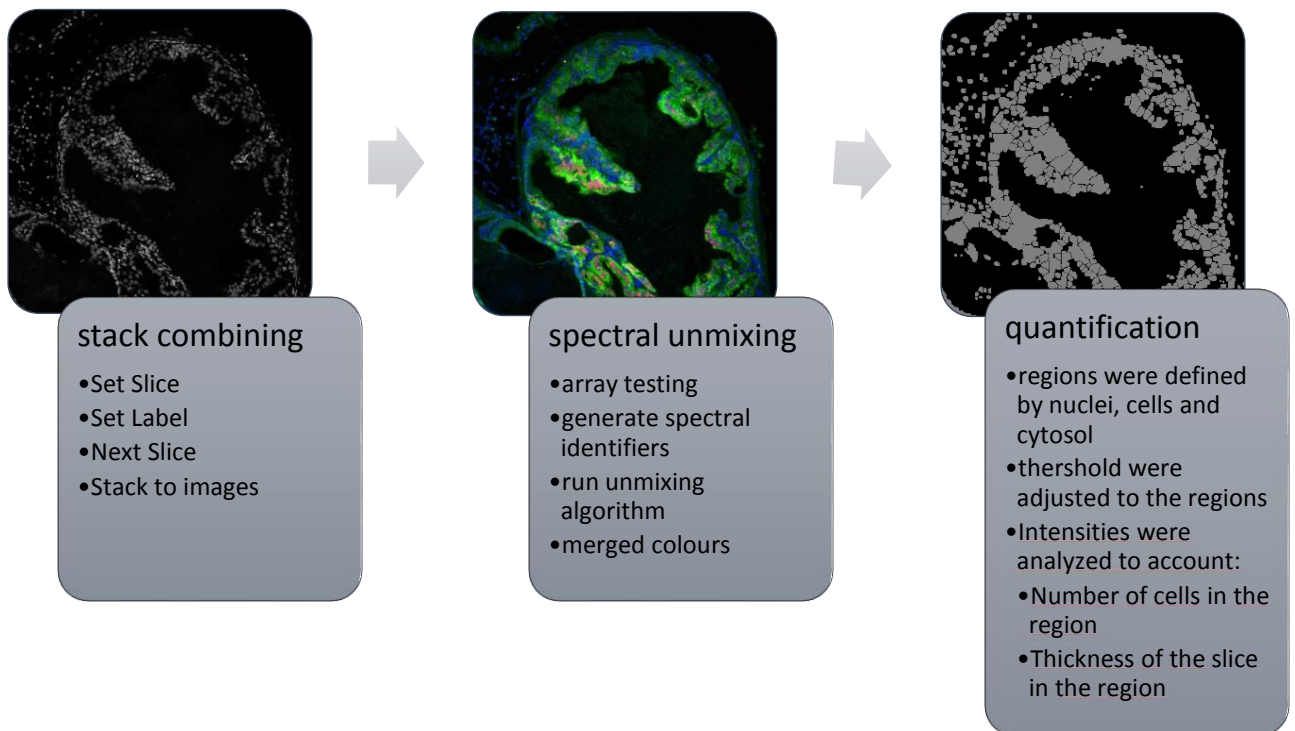


Figure 40: ImageJ Macro Workflow with a *myc+* genotype example

4.2.2 Image quantification of Multistain 1

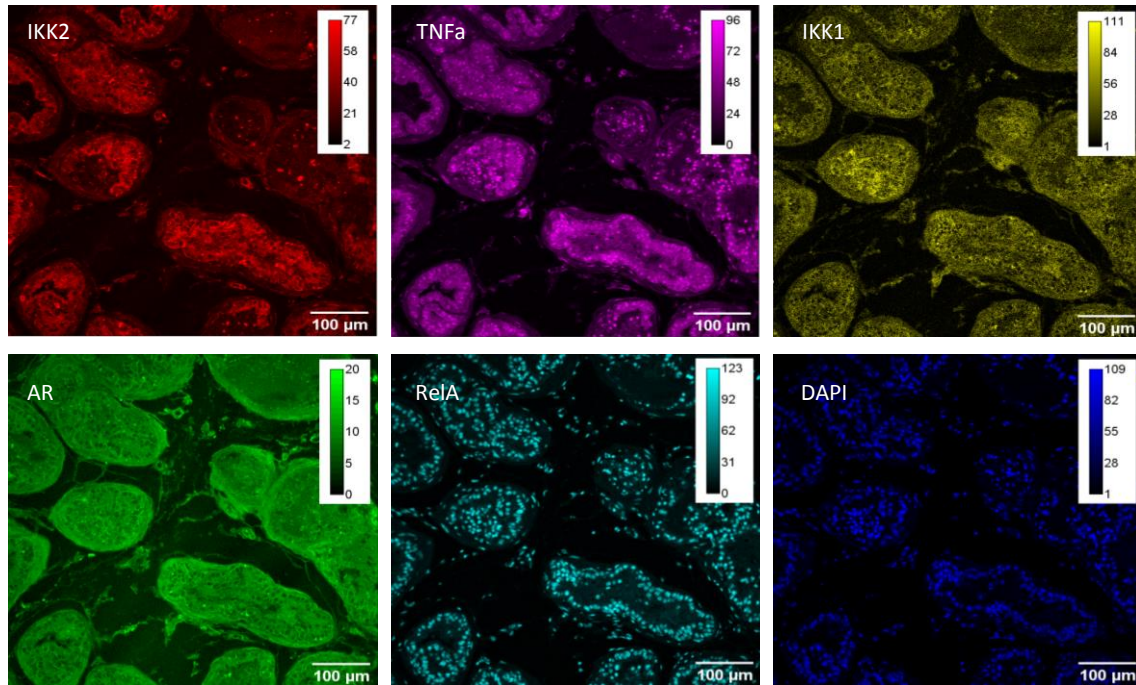


Figure 41: All 6 molecular markers spectrally differentiated with different intensity bars in a wild-type mouse

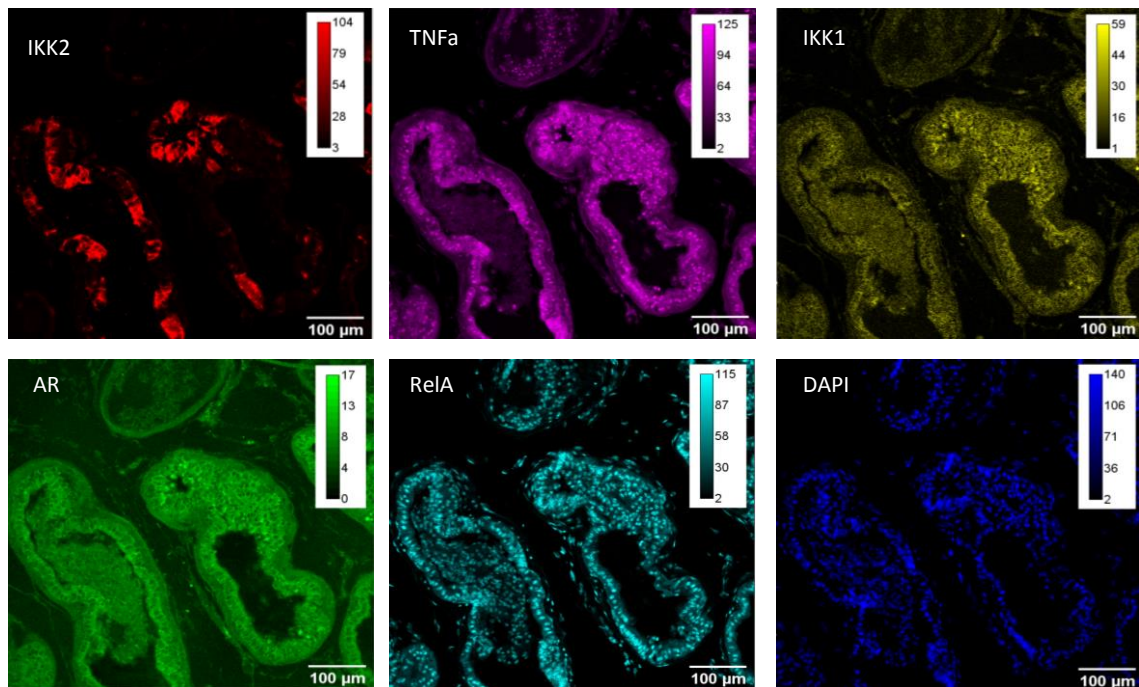


Figure 42: All 6 molecular markers spectrally differentiated with different intensity bars in a calKK2+ mouse

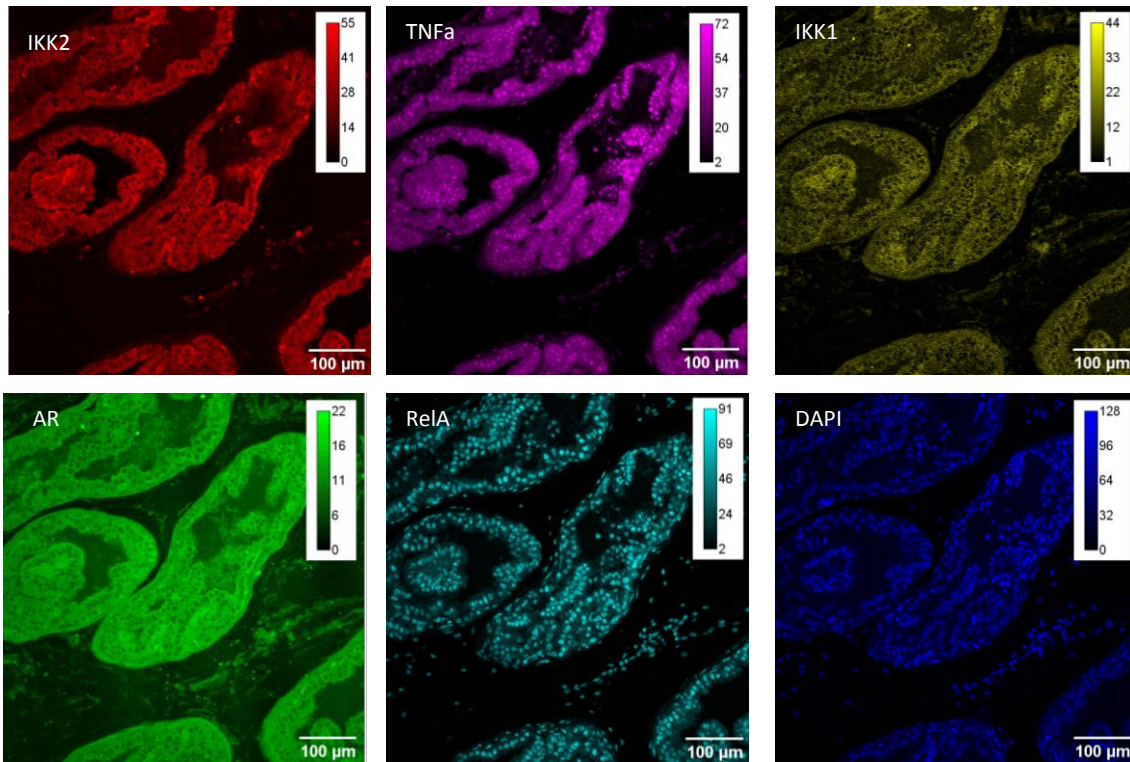


Figure 43: All 6 molecular markers spectrally differentiated with different intensity bars in a *myc*⁺ mouse

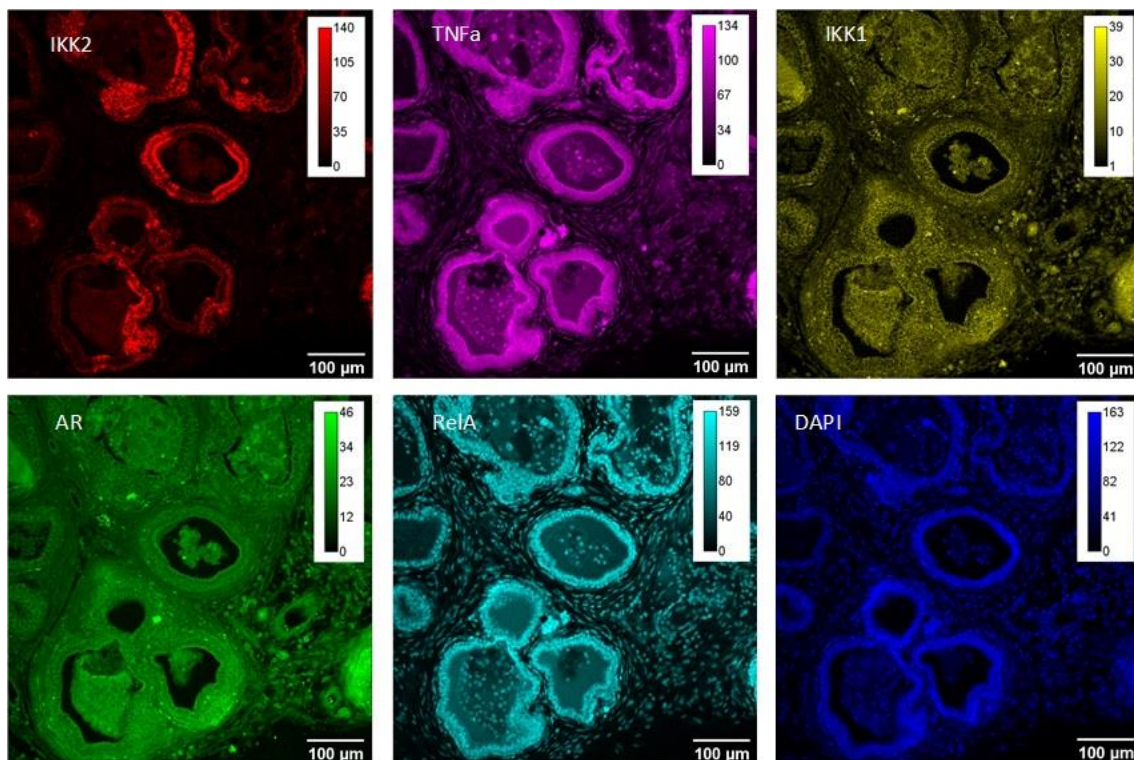


Figure 44: All 6 molecular marker spectrally differentiated with different intensity bars in a *calIKK2*⁺*myc*⁺ mouse

For result analysis we plotted median 1st and 3rd quartile and 0.95 interval of the signal intensities per region. We visualised the used sample size and show intensity distribution with the aid of the histogram. In addition, we show the different correlations patterns between the

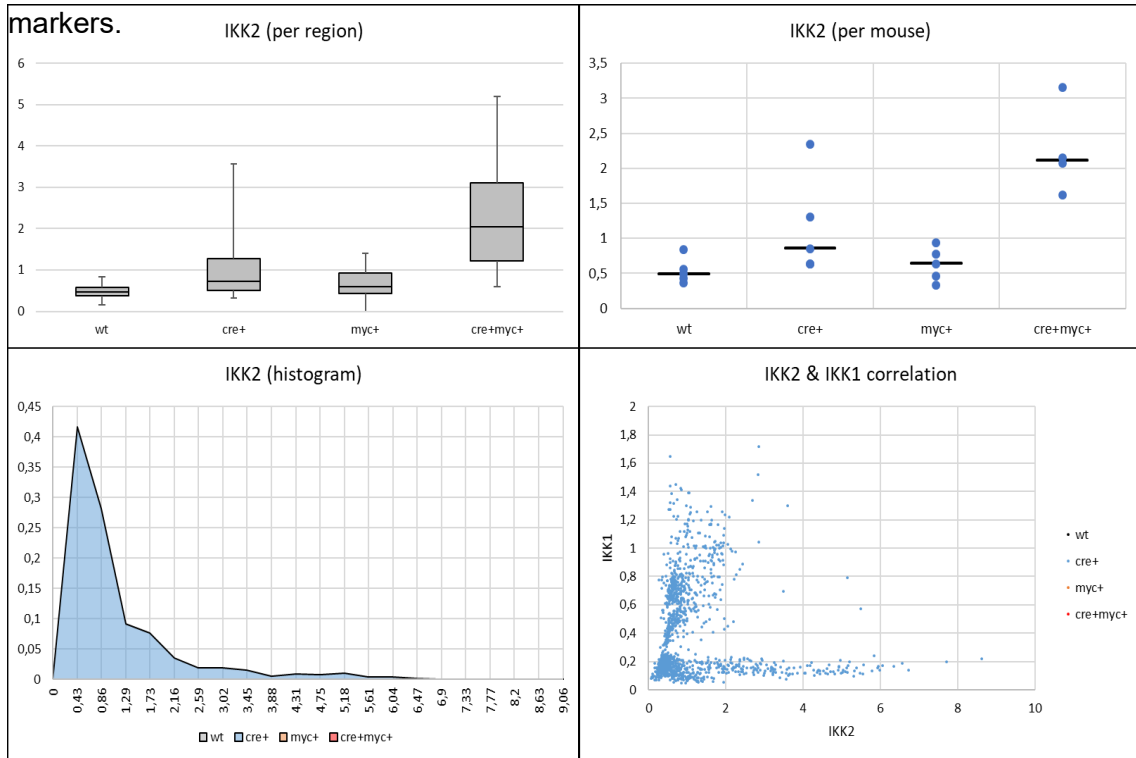


Figure 45: We see the expected higher expression of IKK2 in calKK2+ mice and the unpredictable strongly elevated expression in calKK2+myc+. Especially in calKK2+ mice we observed a strong negative correlation of IKK2 and IKK1, that can be better seen when only cre+ dots are blotted. Indicating that when IKK2 is highly expressed IKK1 expression is low and the other way around.

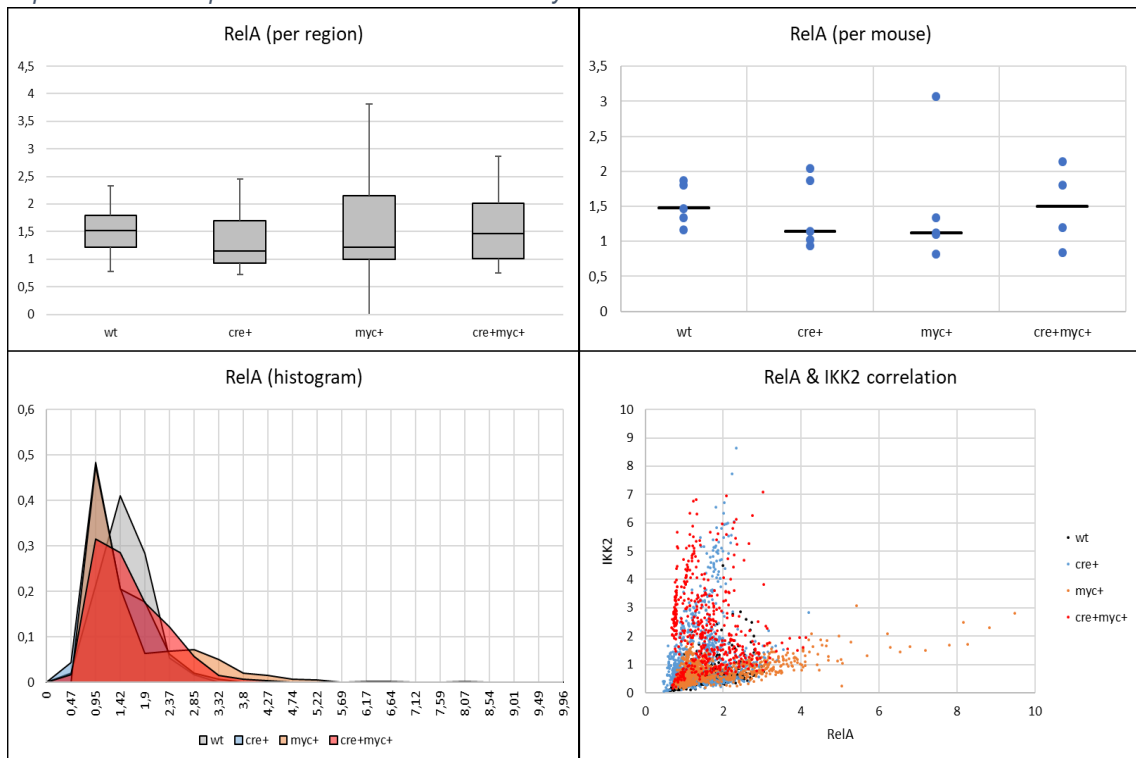


Figure 46: RelA expression did not vary much between the genotypes and show a low correlation with IKK2

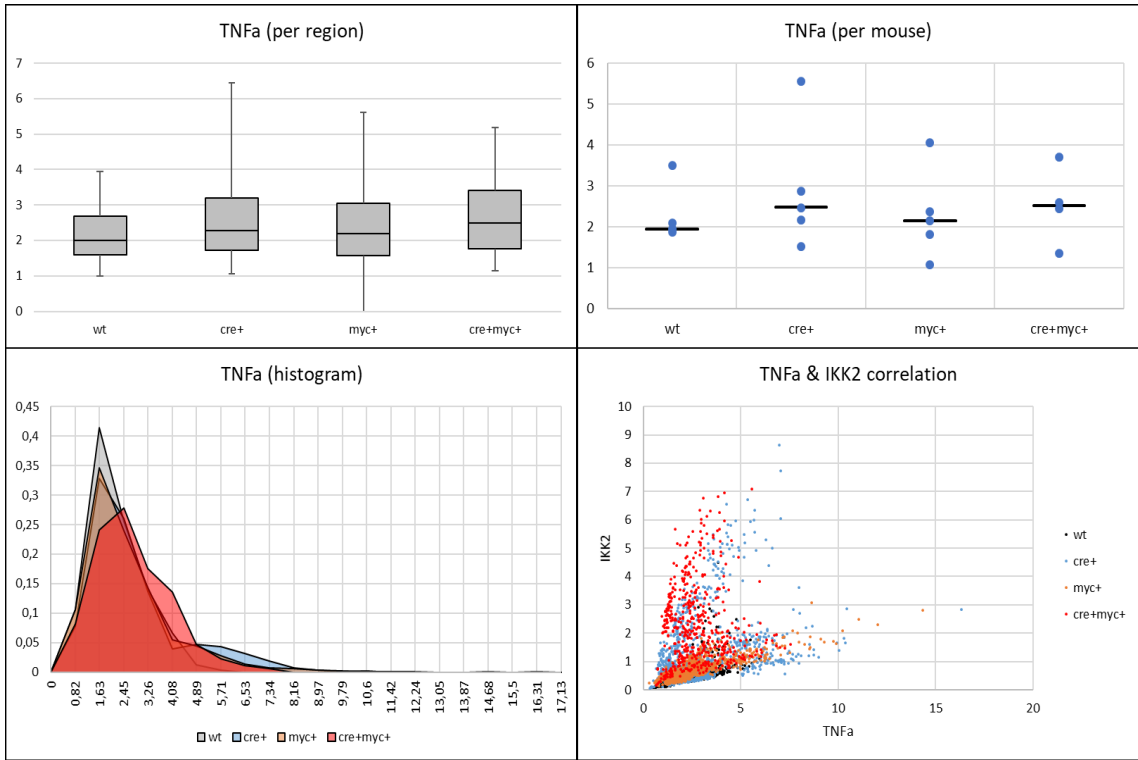


Figure 47: TNFa expression is evenly distributed through all genotypes. The highest expression is observed in calKK2+ confirming connections of TNFa to inflammation. We see the lighty L-shaped correlation with IKK2 in calKK2+ and calKK2+myc+ genotypes, revealing a moderate correlation of TNFa with inflammation and cancer.

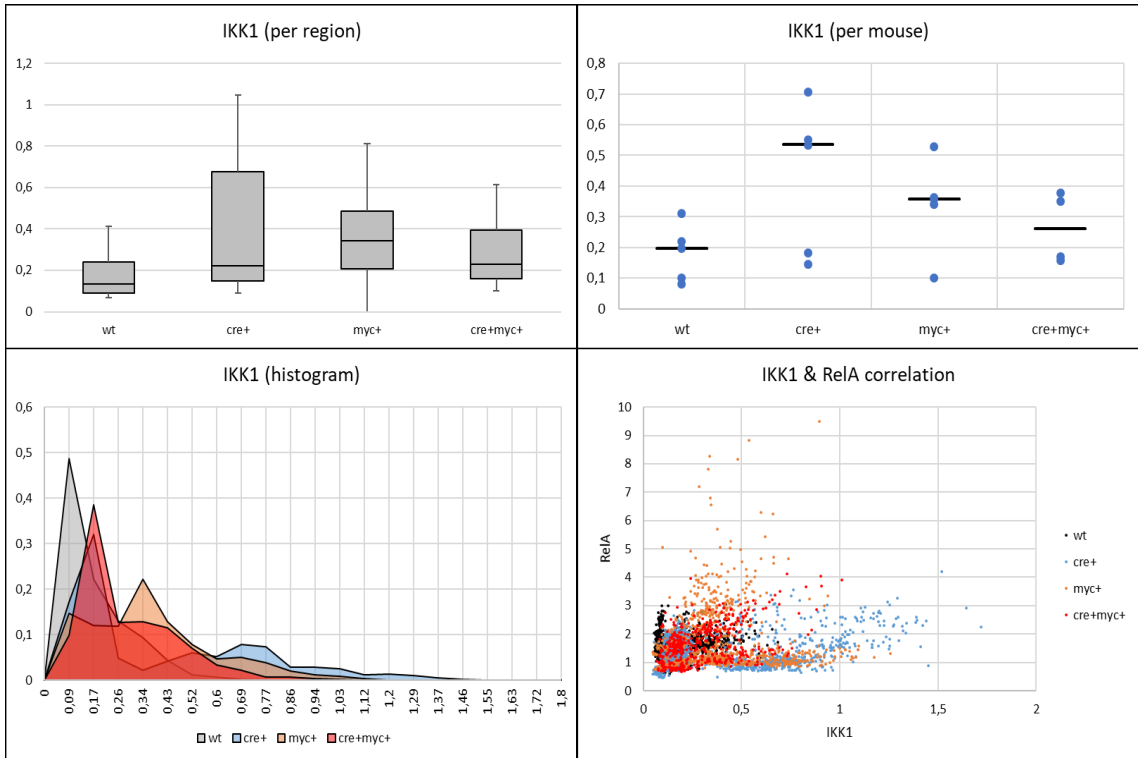


Figure 48: IKK1 expression is as expected upregulated in calKK2+ mice, but not as high as IKK2 in calKK2+myc+ genotypes. Contrary to expectation the expression of IKK1 is higher in myc+ mice than in calKK2+myc+. IKK1 seem to have low to no correlation with RelA.

4.2.3 Image quantification of Multistain 2

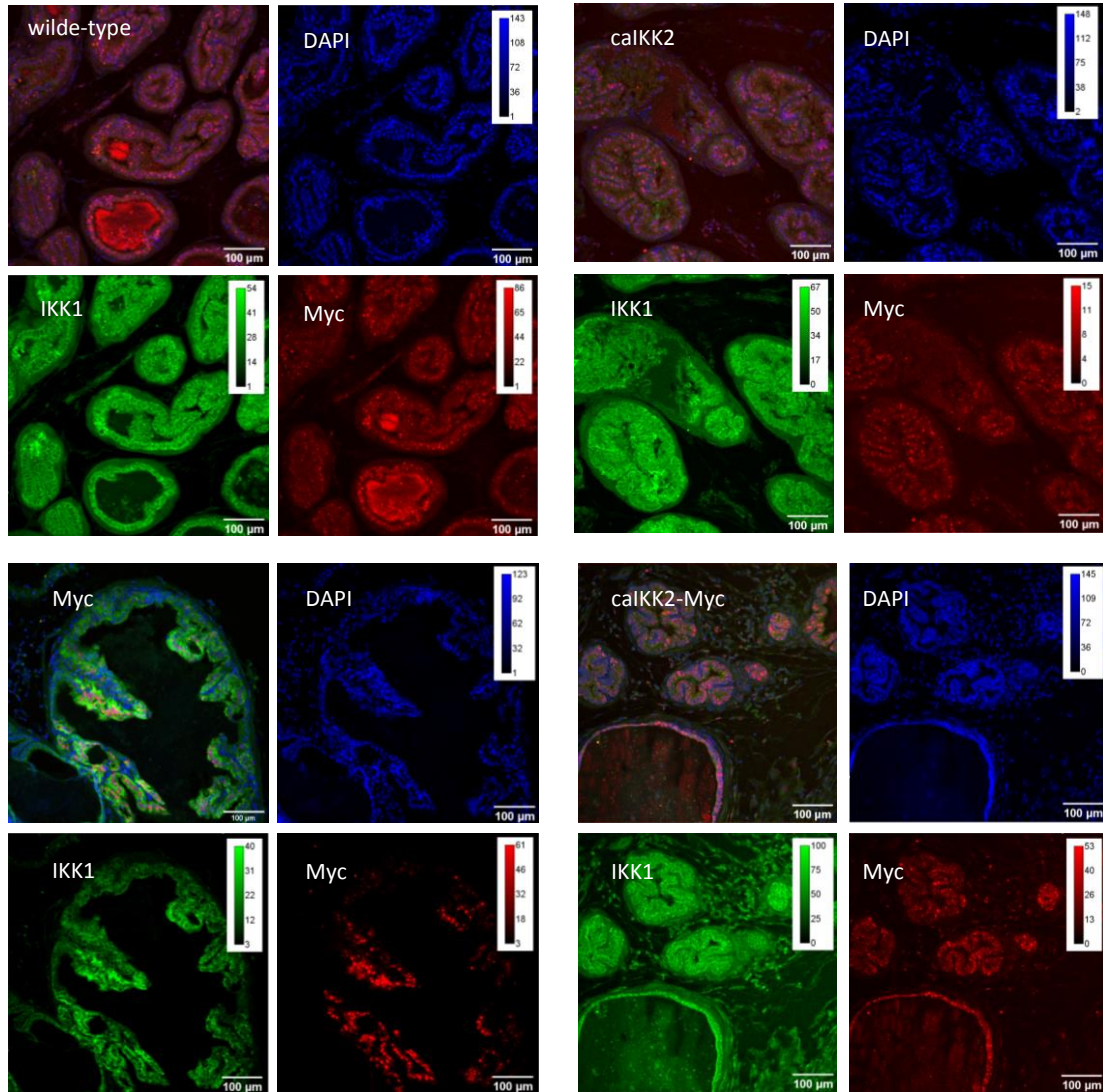


Figure 49: spectral unmixed fluorescence intensities of a wildtype vs. *calKK2*, *Myc* and *calKK2+myc+* genotype → as expected *myc+* mice have a clearly higher intensity bar for *IKK1* and *Myc*. Especially in the *myc+* mice we see the specific *Myc* stain in the nuclei compared to the others, where the fluorophore intensity is more evenly distributed. In *calKK2* mice the *Myc* intensity bar show lower expression than in wild-type mice. The high *IKK1* expression in *calKK2+myc+* mice is giving first hints for a positive correlation to cancer.

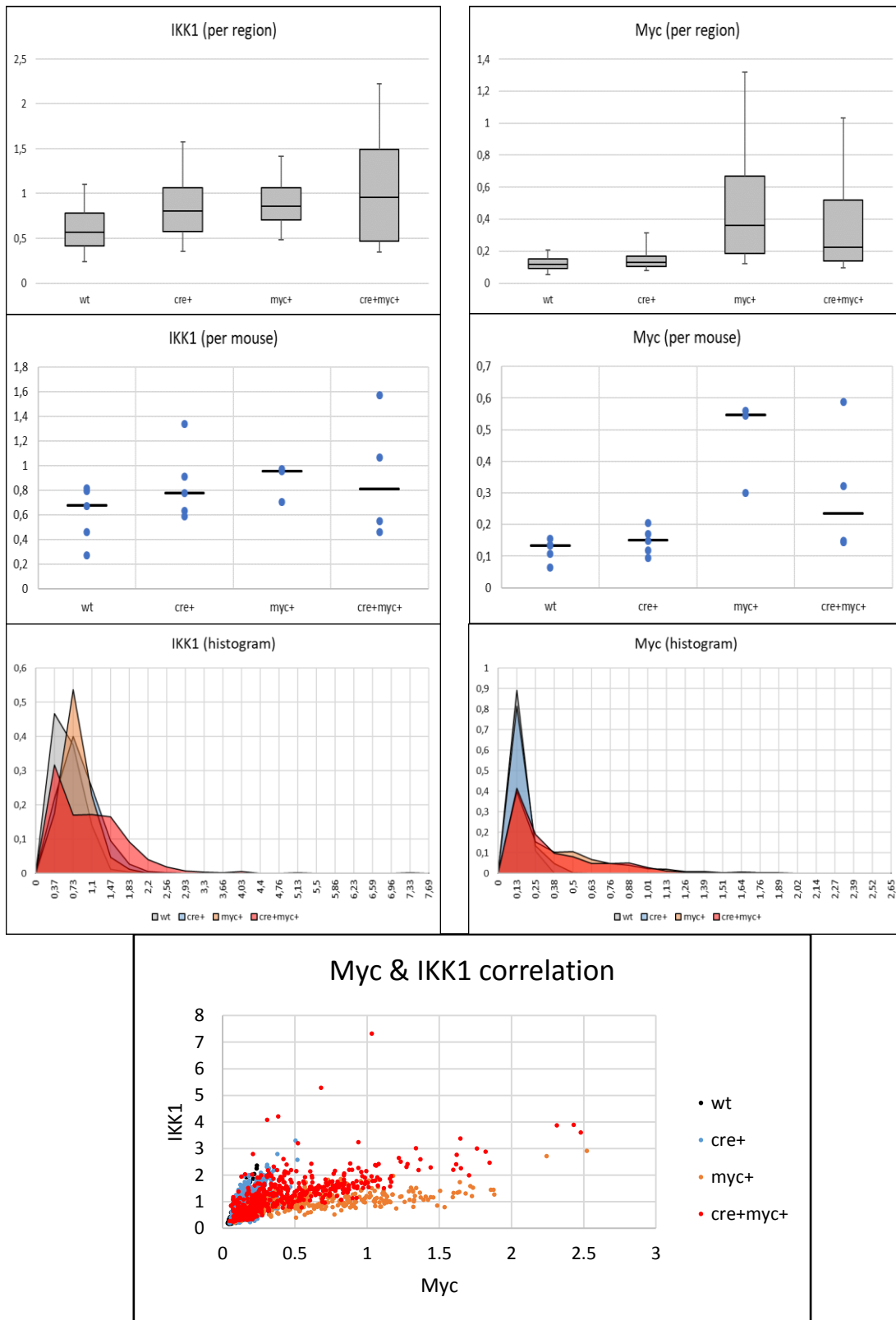


Figure 50: There are no tremendous differences of IKK1 expression between the genotypes. Confirming the mouse model Myc expression is clearly higher in myc+ mice compared to the other genotypes. Myc expression seems to be distributed more evenly than IKK1 seen in the histograms. The correlation between the Myc and IKK1 specially in myc+ and calKK2+myc+ samples show a positive trend. This is giving evidence for the role of inflammation in cancer.

4.3 H&E stain annotation for IKOSA®

Due to the lack of reliable mouse prostate anatomy sources, it is especially difficult to distinguish the four lobes. We could find eight past works in the literature which displayed the differences of the four prostate lobes in the mouse. Based on these we generated a categorization scheme (see table 2) and applied it to our samples, fully annotating five full slide scans per genotype. The presence of homogenous eosinophilic secretion in big acini, centrally located nuclei of the epithelial cells and the prominent fibromuscular layer of each of the glands are typical indicators for the anterior lobe Figure 51 A. In contrast to the ventral lobe Figure 51 B, which has only pale secretion, basally located nuclei and a thin fibromuscular layer as well as the least amount of infoldings compared to the others. The luminal secretion of the dorsal lobe Figure 51 C is homogeneous and eosinophilic, nuclei are located centrally in the secretory cells and the acini small in diameter are surrounded by a relatively dense stroma. The lateral lobe Figure 51 D consists of small to large glandular lumina filled with eosinophilic secretion with very little infoldings and basally located nuclei.

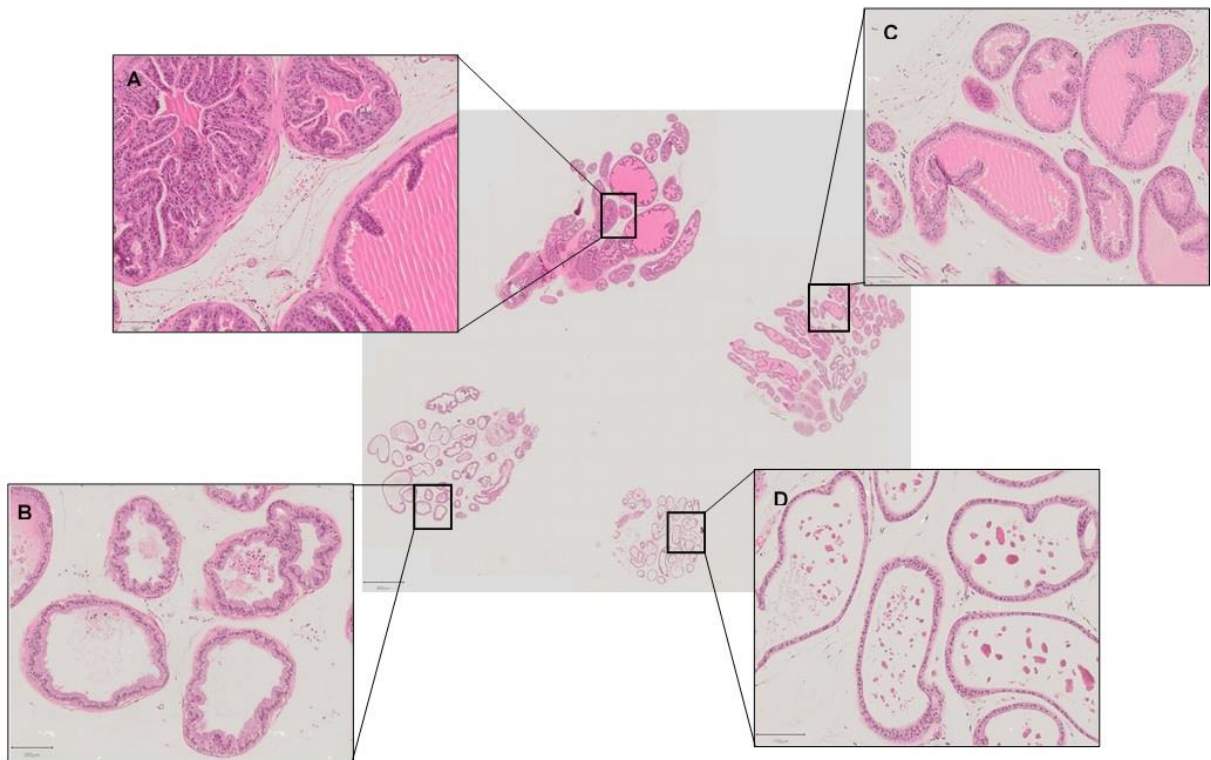


Figure 51: Histological features and differences between the 4 mouse lobes: A is the Anterior lobe, B the Ventral lobe, C the Dorsal lobe and D the Lateral lobe

Table 2: Categorization for lobe annotation

	Anterior	Dorsal	Lateral	Ventral
Secretion	Homogenous, strong	Homogenous, strong	fragmented	Homogenous, pale
Acini Size	Very Large	Small - medium	Varying	Varying
Infolding	very much	very much	very little	very little
Tufting	occasional	occasional	very little	very much
Cell shape	cuboidal to columnar	cuboidal	cuboidal	cuboidal to columnar
Nuclei localization	central	central	basal	basal
Smooth Muscle cells	Typically strong	Normal	Normal	Normal



Figure 52: Example of the annotated version as seen on the IKOSA platform

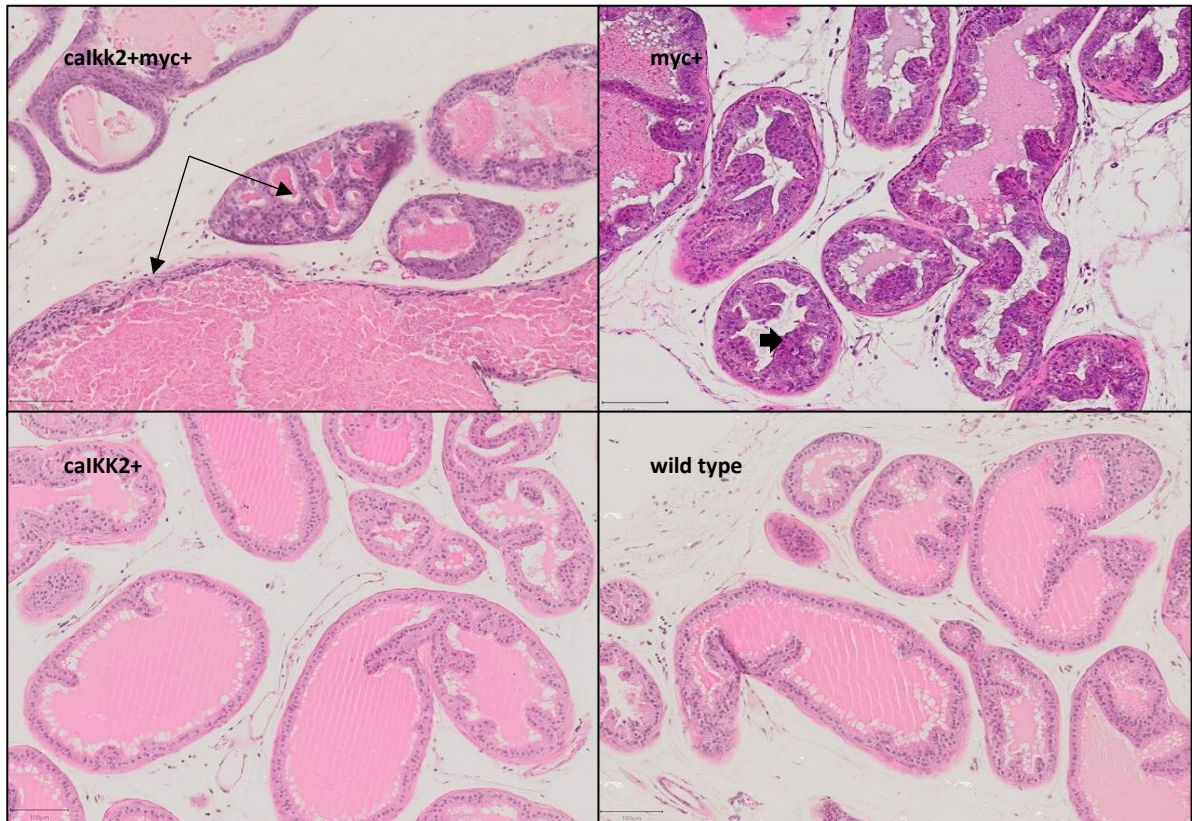


Figure 53: The different dorsal lobes of all 4 genotypes:

calKK2+ which reflects the inflammatory phenotype shows nearly no difference to wild type which is the healthy dorsal lobe. In contrast to the cancerous *myc+* lobe, which looks completely different in terms of nuclei density and budding of cells (arrow). And also the *calKK2+myc+* genotype lacks in typical lobe characteristics seen as loss of monolayer, eosinophilic secretion differentiation and irregular ducts (black arrows).

4.4 qPCR Results

qRT-PCR reactions were performed in triplicate and $2^{-\Delta\Delta CT}$ were used to calculate the relative expression level of the target genes (IKK1, IKK2, c-Myc, AR, RelA, TF, p63) compared to RWPE (epithelial cells derived from histologically normal adult human prostate) with GAPDH as a normalization control.

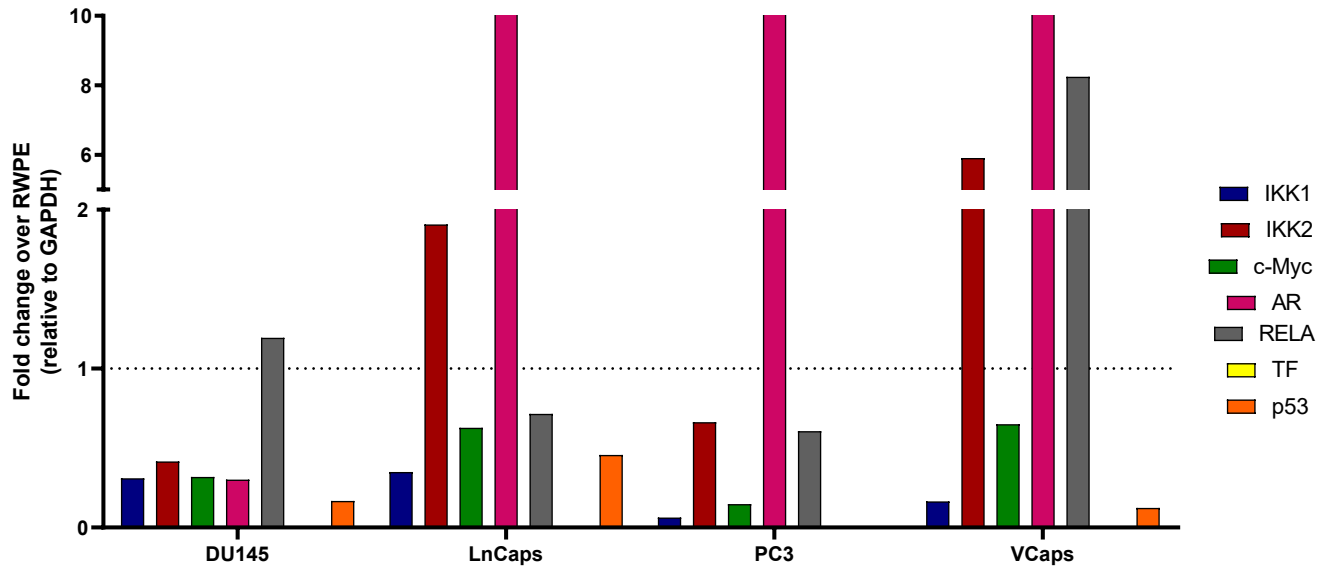


Figure 54: RNA expression in prostate cancer cell lines relative to RWPE a non-cancerous human prostate cell line. We see that IKK2, AR and RelA have a clearly higher expression pattern than RWPE showing the connection between cancer and inflammation. In confirmation with our multistainings we see the IKKB upregulation in PCa cells.

5 Discussion

The first of our aims was to characterize mouse prostate cancer models regarding their inflammatory and cancerous phenotype. We used three different mouse models, which overexpress either inflammatory calKK2 or cancerous c-Myc or both specifically in the epithelial cells of the prostate and compared them to wild type. Therefore, we tested various antibodies used in cancer and inflammatory research in two antigen retrieval buffers and different concentrations.

Based on reliable staining outputs we chose two stains with multiple markers, one with up to five and one with just two targets. The following antibodies: RelA, AR, IKK1, TNF α , IKK2 together with nuclear stain DAPI are used in the multistain 1 and performed very well, with one exception, which is the androgen receptor antibody. Instead of expression in the nucleus as seen in the literature (proteintlas.org) the androgen receptor antibody stained the epithelial cells seen in Figure 25. We first suggest that the used mouse was castrated, but that was not the case. More control stains in different genotypes as well as an antibody validation with western blot would be needed to evaluate this discrepancy. For the multistain 2 we used Dapi, IKK1 and c-Myc to clarify their expression pattern in the different genotypes. Both overexpression models could clearly be seen in our results as demonstrated by higher c-Myc or IKK2 expression respectively.

While in bright field microscopy quantification of images is hardly achievable, fluorescence-based microscopy even allows the quantification of multi-labelled images due to linear unmixing spectral deconvolution. Multiple band-pass filters enable the elimination of unspecific signal and autofluorescence simplifying the unmixing of fluorescent signals. A series of different emission wavelengths are collected to a lambda stack which is very helpful for multi-indicator imaging, but also represents a very time and data intensive method. Microscopy always requires compromises between photobleaching, image resolution, illumination intensity and speed. With the laser scanning microscope software of our institute, it was not possible to spectral scan large images pixel by pixel with all laser one after the other, instead every time just one laser scanned the whole slide followed by the next one. This created large images with pixel-shifts that were impossible to analyze. In addition, large images have the big disadvantage of very high data volumes, which need high performance processors and big data storage capacities. To solve this problem, instead of whole slide images we selected three regions of interest of the prostate lobes trying to facilitate an average signal acquisition. Analyzing and quantification was done with the freeware ImageJ/FIJI. We thoroughly tested

three different spectral unmixing routines, only one of those allowed a satisfying spectral deconvolution in a fully automated manner.

In the next step we tried to overcome difficulties in intensity quantification. First, we thought that the dilated DAPI channel defines the regions we were interested in, but this can be used only for certain lobe regions. To create a more flexible use for all our images we created a detection mask for average intensities and adjusted it to the epithelial, nuclei and cytosol threshold. The analyzed intensities of the whole area, nuclear and cytosol regions were plotted and visualized with histograms. Our complex experimental settings, where we have four different genotypes, five mice per strain, two different immunohistochemistry stains from which three regions were selected each, made statistical analysis highly complex and it will require more development in the future. However, with the aid of the generated boxplots and histograms we can already visualize the distribution and recognize interesting trends. The most interesting outcome of all correlations we set up, is the negative correlation of IKK1 with IKK2 in calKK2 mice. This antagonistic effect may result from a feedback loop initiated and progressed in response to inflammatory stress, where the high abundance of one IKK subunit directly or indirectly influences the other. Maybe the inhibition of one of these kinases can have positive effects on PCa patients dealing with chronic inflammation. This finding is consistent with our in vitro experiment in human prostate cancer cell lines, where IKK2 was upregulated in most of our prostate cancer cell lines compared to a normal (non-malignant) prostate cell line. Our results show that targeting the NF- κ B pathway with focus on the IKK2 protein kinase can have attractive therapeutic effects for advanced cancer treatments, which is in accordance with the findings by Zhang et al. 2016.

In multistain 2 we see the correlation of IKK1 with Myc additionally demonstrating the strong connection of inflammation and cancer. Consistent with Nakai and Nonomura 2013 we show the association between prostate inflammation and increased risk of PCa. We give evidence that combination therapies with NF- κ B pathway inhibitors represent a potent and novel regimen for the treatment of PCa on the one hand. On the other hand, we demonstrate that multifactorial imaging can help to improve diagnostic decisions in precision medicine due to the simultaneous evaluation of protein expression, confirmed by Salto-Tellez et al. 2018.

Next steps towards precision diagnostics would be the automated analysis of cell structures, compartments and identities for the discrimination of normal and cancerous tissue. Optimization and validation of multistains with a basal cell marker would also improve fluorescence intensity and cell structure analysis, which will be done in the continuing project.

Up to now, there exist no freely available databases where mouse prostates have been classified and clustered for cancer and inflammation. H&E stains have always been used for histological observations of cell structure and identity. Therefore, we performed a batch of whole slide scans, having 20 H&E images of each genotype uploaded to the IKOSA® platform. For the establishment of an algorithm, that cluster and correlate the genotypes, images first must be annotated. Identifying and labelling the four different lobes was constricting, because of the fact that in most publications just one small lobe or just a distinct region instead of whole prostate lobe images with defined structures were available. We established a mouse prostate databank including all our genotypes by uploading large images on the IKOSA® platform which will be analyzed with trained algorithms. We hope to provide this database for free to the scientific community in the future. Personalized cancer care is needed more and more as well as aids and improvements in therapy decision that can be applied by accurate biomarker evaluation and quantitative histopathology. Next step towards precision pathology might be artificial intelligence and other “big data” approaches, that alleviate the inter- and intra-observer variability problems, reduce pathology workload and provide regions with pathologic expertise where it is unavailable. Or as Salto-Pelez et al 2018 argue “Artificial intelligence- the third revolution in pathology”. But trained networks as diagnostic tool or help with higher specificity and sensitivity are still awaited for the full implementation in the PCa diagnosis pipeline. Which is good in terms of adequate training data and consistent labelling as algorithms will also learn from human mistakes.

"It is our duty to ensure that we're using AI as another tool at our disposal—not the other way around" (Khullar 2019).

6 Summary- English

One of nine men will be diagnosed with prostate cancer during his lifetime. Incidences differ between continents and populations and are especially high in African Americans. Prostate cancer is very often diagnosed in advanced stages due to the minor symptoms that accompany it in earlier stages.

Tissue biopsy remains the gold standard for diagnosis. A pathologist correlates the tissue sample to the Gleason grading system according to the presence and microscopic architecture of neoplastic cells. The high heterogeneity between patients, the subjectivity of each pathologist, and the imprecise sampling procedure can often result in undergrading. In order to provide a better diagnostic toolset for pathology and histology, the microscopic examination of tissue samples must evolve from the traditional visual examination of the tissue and cell structure further towards a more detailed quantitative analysis of different biomarkers via immunohistological staining, which is evaluated by digital image analysis.

In our study, we utilized three mouse models: One overexpressing the proto-oncogene c-Myc, one overexpressing constitutively active IKK2, thereby reflecting a chronically inflammatory phenotype, and one that expresses both in order to investigate the effects of inflammation and cancer co-dependently. The overexpression is restricted to prostate epithelial cells via a Probasin promoter.

We applied different staining methods in order to investigate these genotypes on a macro- and microscopic level. A large number of classical hematoxylin and eosin stains were obtained and full-slide scans were performed to obtain a large data-base of the respective prostate architecture. These slides were entered into the IKOSA platform, which will later allow the development of machine learning and AI-powered evaluation routines.

Additionally, we applied fluorescent stainings of specific molecular targets. For this, a variety of different antibodies aimed at immunologically relevant proteins was tested and optimized for the use in mouse prostate tissues. These antibodies contained different fluorescent labels and were subsequently combined for multi stainings, thereby providing a comprehensive immunological profile within a single stain. The evaluation of these required the development of special evaluation routines to handle the large data volumes and separate the different labels spectrally, which was done in the free image evaluation software ImageJ/FIJI.

From the sum of results, we could clearly distinguish the different genotypes and could determine important differences and similarities between them.

In order to better understand the role of our targets in different prostate cancer types, we additionally compared mRNA of our targets in 4 typical prostate cancer cell lines with a non-metastatic prostate cell line via qPCR.

As part of an ongoing project, this work did not obtain a large amount of final conclusions but provides a solid basis for the detailed analysis of the interplay between inflammation and cancer within the prostate on a state-of-the-art level.

7 Summary- German

Bei einem von neun Männern wird zu Lebzeiten Prostatakrebs diagnostiziert. Die Inzidenzen unterscheiden sich zwischen Kontinenten und Bevölkerungsgruppen und sind bei Afroamerikanern besonders hoch. Prostatakrebs wird sehr häufig in fortgeschrittenen Stadien diagnostiziert, da in früheren Stadien nur geringfügige Symptome auftreten.

Die Nadelbiopsie bleibt der Goldstandard für die Diagnose. Ein Pathologe korreliert die Gewebeprobe mit dem Gleason-Wertungssystem entsprechend dem Vorhandensein und der mikroskopischen Architektur neoplastischer Zellen. Die hohe Heterogenität zwischen den Patienten, die Subjektivität jedes Pathologen und das nicht standardisierte Probeverfahren können häufig zu einer zu niedrigen Bewertung führen. Um ein besseres diagnostisches Instrumentarium für Pathologie und Histologie bereitzustellen, muss sich die mikroskopische Untersuchung von Gewebeproben von der traditionellen visuellen Untersuchung der Gewebe- und Zellstruktur zu einer detaillierteren quantitativen Analyse verschiedener Biomarker mittels immunhistologischer Färbung entwickeln, die via digitale Bildanalyse evaluiert wird.

In unserer Studie verwendeten wir drei Mausmodelle: eines, das das Protoonkogen c-Myc überexprimiert, eines, das konstitutiv aktives IKK2 überexprimiert und damit einen chronisch entzündlichen Phänotyp widerspiegelt, und eines, das beide exprimiert, um die Auswirkungen von Entzündungen und Krebs co-abhängig zu untersuchen. Die Überexpression ist über einen Probasin-Promotor auf Prostataepithelzellen beschränkt.

Wir haben verschiedene Färbemethoden angewendet, um diese Genotypen auf makro- und mikroskopischer Ebene zu untersuchen. Eine große Anzahl klassischer Hämatoxylin- und Eosin-Färbungen wurde erhalten, und es wurden Großaufnahmen durchgeführt, um eine große Datenbank der jeweiligen Prostata-Architektur zu erhalten. Diese Bilder wurden in die IKOSA-Plattform hochgeladen, die später die Entwicklung von Routinen für maschinelles Lernen und AI-basierte Evaluierung ermöglichen wird.

Zusätzlich haben wir fluoreszierende Färbungen spezifischer molekularer Targets angewendet. Zu diesem Zweck wurde eine Vielzahl verschiedener Antikörper gegen immunologisch relevante Proteine getestet und für die Verwendung in Prostatageweben von Mäusen optimiert. Diese Antikörper enthielten verschiedene fluoreszierende Markierungen und wurden anschließend für Mehrfachfärbungen kombiniert, wodurch ein umfassendes immunologisches Profil innerhalb einer einzelnen Färbung bereitgestellt wurde. Die Auswertung dieser erforderte die Entwicklung spezieller Auswertungsroutinen, um die großen

Datenmengen zu bewältigen und die verschiedenen Marker spektral zu trennen, was in der kostenlosen Bildauswertungssoftware ImageJ / FIJI durchgeführt wurde.

Aus der Summe der Ergebnisse konnten wir die verschiedenen Genotypen klar unterscheiden und wichtige Unterschiede und Ähnlichkeiten zwischen ihnen feststellen.

Um die Rolle unserer Protein-Targtes bei verschiedenen Prostatakrebsarten besser zu verstehen, haben wir zusätzlich die mRNA unserer Targets in 4 typischen Prostatakrebszelllinien mit einer nicht metastatischen Prostatazelllinie über qPCR verglichen. Im Rahmen eines laufenden Projekts wurden in dieser Arbeit nicht viele endgültige Schlussfolgerungen gezogen, sondern es wurde eine solide Grundlage für die detaillierte Analyse des Zusammenspiels von Entzündung und Krebs in der Prostata auf dem neuesten Stand der Technik geschaffen.

8 References

- Abdulkadir, S. A., Carvalhal, G. F., Kaleem, Z., Kisiel, W., Humphrey, P. A., Catalona, W. J., Milbrandt, J. 2000. Tissue factor expression and angiogenesis in human prostate carcinoma. *Human Pathology*, 31(4): 443–447. <https://doi.org/10.1053/hp.2000.6547>
- Acs, B., Rantalainen, M., Hartman, J. 2020. Artificial intelligence as the next step towards precision pathology. *Journal of Internal Medicine*,. <https://doi.org/10.1111/joim.13030>
- Ahmed, H. U., El-Shater Bosaily, A., Brown, L. C., Gabe, R., Kaplan, R., Parmar, M. K., Collaco-Moraes, Y., Ward, K., Hindley, R. G., Freeman, A., Kirkham, A. P., Oldroyd, R., Parker, C., Emberton, M. 2017. Diagnostic accuracy of multi-parametric MRI and TRUS biopsy in prostate cancer (PROMIS): a paired validating confirmatory study. *The Lancet*, 389(10071): 815–822. [https://doi.org/10.1016/S0140-6736\(16\)32401-1](https://doi.org/10.1016/S0140-6736(16)32401-1)
- Akashi, T., Furuya, Y., Ohta, S., Fuse, H. 2003. Tissue factor expression and prognosis in patients with metastatic prostate cancer. *Urology*, 62(6): 1078–1082. [https://doi.org/10.1016/S0090-4295\(03\)00768-4](https://doi.org/10.1016/S0090-4295(03)00768-4)
- Albert, T. 2019. *Country-specific, Incidence Cancer, Austrian Method, Registry Country-specific, Mortality*. 915: 2018–2019.
- Ballentine Carter, H., Albertsen, Peter, C., Barry, Michael, J., Etzioni, R., Freedland, Stephen, J., Lynn Greene, K., Holmberg, L., Kantoff, P., Konety, B. R., Murad, M. H., Penson, David, F., Zietman, Anthony, L. 2013. Early Detection of Prostate Cancer: AUA Guideline. *J Urol.*, 190(2): 419–426. <https://doi.org/10.1038/jid.2014.371>
- Barfeld, S. J., Urbanucci, A., Itkonen, H. M., Fazli, L., Hicks, J. L., Thiede, B., Rennie, P. S., Yegnasubramanian, S., DeMarzo, A. M., Mills, I. G. 2017. c-Myc Antagonises the Transcriptional Activity of the Androgen Receptor in Prostate Cancer Affecting Key Gene Networks. *EBioMedicine*, 18: 83–93. <https://doi.org/10.1016/j.ebiom.2017.04.006>
- Birbach, A. 2013. *Use of PB-Cre4 Mice for Mosaic Gene Deletion*. 8(1): 1–7. <https://doi.org/10.1371/journal.pone.0053501>
- Birbach, A., Eisenbarth, D., Kozakowski, N., Ladenhauf, E., Schmidt-Supprian, M., Schmid, J. A. 2011. Persistent inflammation leads to proliferative neoplasia and loss of smooth muscle cells in a prostate tumor model. *Neoplasia*, 13(8): 692–703. <https://doi.org/10.1593/neo.11524>
- Bostwick, D. G., Cheng, L. 2014. Neoplasms of the prostate. In *Urologic Surgical Pathology* (3rd ed., pp. 442–579). <https://doi.org/10.1016/b978-0-323-01970-5.50011-7>
- Bray, F., Ferlay, J., Soerjomataram, I., Siegel, R. L., Torre, L. A., Jemal, A. 2018. Global cancer

- statistics 2018: GLOBOCAN estimates of incidence and mortality worldwide for 36 cancers in 185 countries. *CA: A Cancer Journal for Clinicians*, 68(6): 394–424. <https://doi.org/10.3322/caac.21492>
- Chen, H., Liu, H., Qing, G. 2018. Targeting oncogenic Myc as a strategy for cancer treatment. *Signal Transduction and Targeted Therapy*, 3(1): 1–7. <https://doi.org/10.1038/s41392-018-0008-7>
- Chopra, D. P., Menard, R. E., Januszewski, J., Mattingly, R. R. 2004. TNF- α -mediated apoptosis in normal human prostate epithelial cells and tumor cell lines. *Cancer Letters*, 203(2): 145–154. <https://doi.org/10.1016/j.canlet.2003.09.016>
- Comp erat, E. 2019. Evolution of prostate cancer histopathology. *Current Opinion in Urology*, 29(6): 587–592. <https://doi.org/10.1097/MOU.0000000000000669>
- Denis Semwogerere, E. R. W. 2005. Separating blue whiting (*Micromesistius poutassou* Risso , 1826) from myctophid targets using multi-frequency methods. *Encyclopedia of Biomaterial and Biomedical Engineering*, 97. <https://doi.org/10.1081/E-EBBE-120024153>
- Dhillon, P. K., Barry, M., Stampfer, M. J., Perner, S., Fiorentino, M., Fornari, A., Jing, M., Fleet, J., Kurth, T., Rubin, M. A., Mucci, L. A. 2009. Aberrant cytoplasmic expression of p63 and prostate cancer mortality. *Cancer Epidemiology Biomarkers and Prevention*, 18(2): 595–600. <https://doi.org/10.1158/1055-9965.EPI-08-0785>
- Donin, N. M., Reiter, R. E. 2018. Why targeting PSMA is a game changer in the management of prostate cancer. *Journal of Nuclear Medicine*, 59(2): 177–182. <https://doi.org/10.2967/jnumed.117.191874>
- Ellwood-Yen, K., Graeber, T. G., Wongvipat, J., Iruela-Arispe, M. L., Zhang, J. F., Matusik, R., Thomas, G. V., Sawyers, C. L. 2003. Myc-driven murine prostate cancer shares molecular features with human prostate tumors. *Cancer Cell*, 4(3): 223–238. [https://doi.org/10.1016/S1535-6108\(03\)00197-1](https://doi.org/10.1016/S1535-6108(03)00197-1)
- Epstein, J. I., Allsbrook, W. C., Amin, M. B., Egevad, L. L., Bastacky, S., L pez Beltr n, A., Berner, A., Billis, A., Boccon-Gibod, L., Cheng, L., Civantos, F., Cohen, C., Cohen, M. B., Datta, M., Davis, C., Delahunt, B., Delprado, W., Eble, J. N., Foster, C. S., ... Young, R. H. 2005. The 2005 International Society of Urological Pathology (ISUP) consensus conference on Gleason grading of prostatic carcinoma. *American Journal of Surgical Pathology*, 29(9): 1228–1242. <https://doi.org/10.1097/01.pas.0000173646.99337.b1>
- Epstein, J. I., Egevad, L., Amin, M. B., Delahunt, B., Srigley, J. R., Humphrey, P. A. 2016. The 2014 international society of urological pathology (ISUP) consensus conference on gleason grading of prostatic carcinoma definition of grading patterns and proposal for a

- new grading system. *American Journal of Surgical Pathology*, 40(2): 244–252. <https://doi.org/10.1097/PAS.0000000000000530>
- Gleason, D. F. 1992. Histologic grading of prostate cancer: A perspective. *Human Pathology*, 23(3): 273–279. [https://doi.org/10.1016/0046-8177\(92\)90108-F](https://doi.org/10.1016/0046-8177(92)90108-F)
- Goldenberg, S. L., Nir, G., Salcudean, S. E. 2019. A new era: artificial intelligence and machine learning in prostate cancer. *Nature Reviews Urology*, 16(7): 391–403. <https://doi.org/10.1038/s41585-019-0193-3>
- Gorris, M. A. J., Halilovic, A., Rabold, K., van Duffelen, A., Wickramasinghe, I. N., Verweij, D., Wortel, I. M. N., Textor, J. C., de Vries, I. J. M., Figdor, C. G. 2018. Eight-Color Multiplex Immunohistochemistry for Simultaneous Detection of Multiple Immune Checkpoint Molecules within the Tumor Microenvironment. *The Journal of Immunology*, 200(1): 347–354. <https://doi.org/10.4049/jimmunol.1701262>
- Guo, C. C., Epstein, J. I. 2006. Intraductal carcinoma of the prostate on needle biopsy: Histologic features and clinical significance. *Modern Pathology*, 19(12): 1528–1535. <https://doi.org/10.1038/modpathol.3800702>
- Haraguchi, T., Shimi, T., Koujin, T., Hashiguchi, N., Hiraoka, Y. 2002. Spectral imaging fluorescence microscopy. *Genes to Cells*, 7(9): 881–887. <https://doi.org/10.1046/j.1365-2443.2002.00575.x>
- Heinlein, C. A., Chang, C. 2004. Androgen receptor in prostate cancer. *Endocrine Reviews*, 25(2): 276–308. <https://doi.org/10.1210/er.2002-0032>
- Hoogland, A. M., Kweldam, C. F., Leenders, G. J. L. H. V. 2014. Prognostic Histopathological and Molecular Markers on Prostate Cancer Needle-Biopsies: A Review. *BioMed Research International*, 2014:. <https://doi.org/10.1155/2014/341324>
- Humphrey, P. A. 2017. Histopathology of prostate cancer. *Cold Spring Harbor Perspectives in Medicine*, 7(10): 1–21. <https://doi.org/10.1101/cshperspect.a030411>
- Kasivisvanathan, V., Jichi, F., Klotz, L., Villers, A., Taneja, S. S., Punwani, S., Freeman, A., Emberton, M., Moore, C. M. 2017. A multicentre randomised controlled trial assessing whether MRI-targeted biopsy is non-inferior to standard transrectal ultrasound guided biopsy for the diagnosis of clinically significant prostate cancer in men without prior biopsy: A study protocol. *BMJ Open*, 7(10):. <https://doi.org/10.1136/bmjopen-2017-017863>
- Khullar, D. 2019. A.I. Could Worsen Health Disparities. *The New York Times*.. <https://www.nytimes.com/2019/01/31/opinion/ai-bias-healthcare.html>
- Krzyzanowska, A., Lippolis, G., Helczynski, L., Anand, A., Peltola, M., Pettersson, K., Lilja, H.,

- Bjartell, A. 2016. Quantitative Time-Resolved Fluorescence Imaging of Androgen Receptor and Prostate-Specific Antigen in Prostate Tissue Sections. *Journal of Histochemistry and Cytochemistry*, 64(5): 311–322. <https://doi.org/10.1369/0022155416640466>
- Lessard, L., Bégin, L. R., Gleave, M. E., Mes-Masson, A. M., Saad, F. 2005. Nuclear localisation of nuclear factor-kappaB transcription factors in prostate cancer: An immunohistochemical study. *British Journal of Cancer*, 93(9): 1019–1023. <https://doi.org/10.1038/sj.bjc.6602796>
- Leyh-Bannurah, S. R., Kachanov, M., Beyersdorff, D., Tian, Z., Karakiewicz, P. I., Tilki, D., Fisch, M., Maurer, T., Graefen, M., Budäus, L. 2020. Minimum Magnetic Resonance Imaging-Ultrasound Fusion Targeted Biopsy Cores Needed for Prostate Cancer Detection: Multivariable Retrospective, Lesion Based Analyses of Patients Treated with Radical Prostatectomy. *The Journal of Urology*, 203(2): 299–303. <https://doi.org/10.1097/JU.0000000000000527>
- Lichtman, J. W., Conchello, J. A. 2005. Fluorescence microscopy. *Nature Methods*, 2(12): 910–919. <https://doi.org/10.1038/nmeth817>
- Litwin, M. S., Tan, H. J. 2017. The diagnosis and treatment of prostate cancer: A review. *JAMA - Journal of the American Medical Association*, 317(24): 2532–2542. <https://doi.org/10.1001/jama.2017.7248>
- Mahato, R., Qin, B., Cheng, K. 2011. Blocking IKK α expression inhibits prostate cancer invasiveness. *Pharmaceutical Research*, 28(6): 1357–1369. <https://doi.org/10.1007/s11095-010-0351-z>
- Mistry, K., Cable, G. 2003. Meta-analysis of prostate-specific antigen and digital rectal examination as screening tests for prostate carcinoma. *Journal of the American Board of Family Practice*, 16(2): 95–101. <https://doi.org/10.3122/jabfm.16.2.95>
- Nakai, Y., Nonomura, N. 2013. Inflammation and prostate carcinogenesis. *International Journal of Urology*, 20(2): 150–160. <https://doi.org/10.1111/j.1442-2042.2012.03101.x>
- Nguyen, D. P., Li, J., Yadav, S. S., Tewari, A. K. 2014. Recent insights into NF- κ B signalling pathways and the link between inflammation and prostate cancer. *BJU International*, 114(2): 168–176. <https://doi.org/10.1111/bju.12488>
- Oliveira, D. S. M., Dzinic, S., Bonfil, A. I., Saliganan, A. D., Sheng, S., Bonfil, R. D. 2016. The mouse prostate: A basic anatomical and histological guideline. *Bosnian Journal of Basic Medical Sciences*, 16(1): 8–13. <https://doi.org/10.17305/bjbms.2016.917>
- Paddock, S. 2001. *BiO Imaging Multi-Spectral Imaging and Linear Unmixing Add a Whole New*

Dimension to. 30(2): 1–5.

- Paner, G. P., Gandhi, J., Choy, B., Amin, M. B. 2019. Essential Updates in Grading, Morphotyping, Reporting, and Staging of Prostate Carcinoma for General Surgical Pathologists. *Archives of Pathology & Laboratory Medicine*, 143(5): 550–564. <https://doi.org/10.5858/arpa.2018-0334-RA>
- Pasparakis, M., Luedde, T., Schmidt-Supprian, M. 2006. Dissection of the NF- κ B signalling cascade in transgenic and knockout mice. *Cell Death and Differentiation*, 13(5): 861–872. <https://doi.org/10.1038/sj.cdd.4401870>
- Prensner, J. R., Rubin, M. A., Wei, J. T., Chinnaiyan, A. M. 2012. Beyond PSA: The next generation of prostate cancer biomarkers. *Science Translational Medicine*, 4(127):. <https://doi.org/10.1126/scitranslmed.3003180>
- Ramon, J., Denis, J., L. 2007. Prostate Cancer. In *Springer-Verlag Berlin Heidelberg* (1st ed., Vol. 175). <https://doi.org/10.1017/CBO9781107415324.004>
- Rawla, P. 2019. Epidemiology of Prostate Cancer. *World J Oncol.*, 10(2): 63–89. <https://doi.org/10.1159/000423644>
- Rojo, M. G., Bueno, G., Slodkowska, J. 2009. Review of imaging solutions for integrated quantitative immunohistochemistry in the Pathology daily practice. *Folia Histochemica et Cytobiologica*, 47(3): 349–354. <https://doi.org/10.2478/v10042-008-0114-4>
- Salto-Tellez, M., Maxwell, P., Hamilton, Peter, W. 2018. Artificial Intelligence - The Third Revolution in Pathology. *Histopathology*,. <https://doi.org/10.1111/his.13760>
- Sanderson, Michael, J., Smith, I., Parker, I., Bootman, Martin, D. 2016. Fluorescence Microscopy. *Cold Spring Harb Protoc.*, 10: 139–148. <https://doi.org/10.1016/j.physbeh.2017.03.040>
- Seo, S. Il, Song, S. Y., Kang, M. R., Kim, M. S., Oh, J. E., Kim, Y. R., Lee, J. Y., Yoo, N. J., Lee, S. H. 2009. Immunohistochemical analysis of NF- κ B signaling proteins IKK η , p50/p105, p52/p100 and RelA in prostate cancers. *Apmis*, 117(8): 623–628. <https://doi.org/10.1111/j.1600-0463.2009.02506.x>
- Shappell, S. B., Thomas, G. V., Roberts, R. L., Herbert, R., Ittmann, M. M., Rubin, M. A., Humphrey, P. A., Sundberg, J. P., Rozengurt, N., Barrios, R., Ward, J. M., Cardiff, R. D. 2004. Prostate Pathology of Genetically Engineered Mice: Definitions and Classification. The Consensus Report from the Bar Harbor Meeting of the Mouse Models of Human Cancer Consortium Prostate Pathology Committee. *Cancer Research*, 64(6): 2270–2305. <https://doi.org/10.1158/0008-5472.CAN-03-0946>
- Shi, J., Chen, J., Serradji, N., Xu, X., Zhou, H., Ma, Y., Sun, Z., Jiang, P., Du, Y., Yang, J.,

- Dong, C., Wang, Q. 2013. PMS1077 Sensitizes TNF- α Induced Apoptosis in Human Prostate Cancer Cells by Blocking NF- κ B Signaling Pathway. *PLoS ONE*, 8(4): 1–11. <https://doi.org/10.1371/journal.pone.0061132>
- Siegel, R. L., Miller, K. D., Jemal, A. 2020. Cancer statistics, 2020. *CA: A Cancer Journal for Clinicians*, 70(1): 7–30. <https://doi.org/10.3322/caac.21590>
- Situ, J., Zhang, H., Lu, L., Li, K., Hu, C., Wang, D. J. 2017. Clinical significance of PSMA, TERT and PDEF in malignant tumors of the prostate. *European Review for Medical and Pharmacological Sciences*, 21(15): 3347–3352.
- St Croix, C. M., Shand, S. H., Watkins, S. C. 2005. Confocal microscopy: comparisons, applications, and problems. *BioTechniques*, 39(6 Suppl): <https://doi.org/10.2144/000112089>
- Staal, J., Beyaert, R. 2018. Inflammation and NF- κ B Signaling in Prostate Cancer: Mechanisms and Clinical Implications. *Cells*, 7(9): 122. <https://doi.org/10.3390/cells7090122>
- Statistik Austria*. 2020. https://www.statistik.at/web_de/statistiken/menschen_und_gesellschaft/gesundheit/krebskrankungen/index.html, Last Accessed 02.04.2020
- Streicher, J., Meyerson, B. L., Karivedu, V., Sidana, A. 2019. A review of optimal prostate biopsy: indications and techniques. *Therapeutic Advances in Urology*, 11: 175628721987007. <https://doi.org/10.1177/1756287219870074>
- Trabzonlu, L., Kulac, I., Zheng, Q., Hicks, J. L., Haffner, M. C., Nelson, W. G., Sfanos, K. S., Ertunc, O., Lotan, T. L., Heaphy, C. M., Meeker, A. K., Yegnasubramanian, S., De Marzo, A. M. 2019. Molecular pathology of high-grade prostatic intraepithelial neoplasia: Challenges and opportunities. *Cold Spring Harbor Perspectives in Medicine*, 9(4): 1–20. <https://doi.org/10.1101/cshperspect.a030403>
- Van Leenders, G. J. L. H., Aalders, T. W., Hulsbergen-van de Kaa, C. A., Ruiters, D. J., Schalken, J. A. 2001. Expression of basal cell keratins in human prostate cancer metastases and cell lines. *Journal of Pathology*, 195(5): 563–570. <https://doi.org/10.1002/path.993>
- Waldron, N., Chowdhury, S. 2020. Prostate cancer. *Medicine (United Kingdom)*, 48(2): 119–122. <https://doi.org/10.1016/j.mpmed.2019.11.010>
- Wu, X., Wu, J., Huang, J., Powell, W. C., Zhang, J., Matusik, R. J., Sangiorgi, F. O., Maxson, R. E., Sucov, H. M., Roy-burman, P. 2000. Generation of a prostate epithelial cell-specific Cre transgenic mouse model for tissue-specific gene ablation. *Elsevier Science Ireland*,

101(2001): 61–69.

- Yang, Y., Hao, J., Liu, X., Dalkin, B., Nagle, R. B. 1997. Differential expression of cytokeratin mRNA and protein in normal prostate, prostatic intraepithelial neoplasia, and invasive carcinoma. *American Journal of Pathology*, 150(2): 693–704.
- Zhang, Y., Lapidus, Rena, G., Liu, P., Yong Choi, E., Adediran, S., Hussain, A., Wang, X., Lui, X., Dan, Han, C. 2016. Targeting I κ B kinase β /NF- κ B signaling in human prostate cancer by a novel I κ B kinase β inhibitor CmpdA. *Mol Cancer*, 15(7): 1504–1514. <https://doi.org/10.1016/j.physbeh.2017.03.040>
- Zimmermann, T. 2005. Spectral imaging and linear unmixing in light microscopy. *Advances in Biochemical Engineering/Biotechnology*, 95: 245–265. <https://doi.org/10.1007/b102216>

9 List of Figures

Figure 1: Evolution of the Gleason grading system (Paner et al. 2019).	5
Figure 2: HGPIN patterns: (A) Tufting (B) Micropapillary (C) Cribriform (D) Flat pattern (Bostwick and Cheng 2014)	6
Figure 3: model of retrograde glandular colonization or post invasive intraepithelial carcinoma (Trabzonlu et al., 2019).	7
Figure 4: overview of human and mouse prostate anatomy (Toivanen & Shen, 2017)	8
Figure 5: human vs mouse prostate histology: AP (Anterior Prostate), DP (Dorsal Prostate), VP (Ventral Prostate), LP (Lateral Prostate)	9
Figure 6: excitation emission principle (Bernhard Hochreiter)	15
Figure 7: Optical configuration of a laser scanning microscope	17
Figure 8: handgrafted feature-based ML versus DL (Goldenberg et al., 2019)	19
Figure 9: floxed calKK2 probasin cre, c-Myc and calKK2+c-Myc+ mouse model	26
Figure10: https://www.proteinatlas.org/ENSG00000136997-MYC/pathology/prostate+cancer#img shows the myc expression in the basal layer as well as in some ducts	31
Figure 11: myc+, pH6, 1:1000 → we can see c-myc that is clearly expressed in the basal layer	31
Figure12: https://www.proteinatlas.org/ENSG00000104365-IKBKB/pathology/prostate+cancer#img show IKK2 expression in the epithelial cells, but also small amounts in the stroma	32
Figure 13: myc+, pH9, 1:500 → left you see the mosaic expression in calKK2+myc+ mice compared to myc	32
Figure14: https://www.proteinatlas.org/ENSG00000213341-CHUK/pathology/prostate+cancer#img especially the epithelial cells are stained	33
Figure 15: calKK2+myc+, pH9, 1:50 → we see the high abundance in the epithelial cells	33
Figure16: https://www.proteinatlas.org/ENSG00000186847-KRT14/pathology/prostate+cancer#img there is strong cytoplasmic immunoreactivity in squamous cell carcinomas compared to benign tissues	34
Figure 17: myc+, pH9, 1:50 → we see the green fluorescence of CTK14 in the epithelial cell layer	34

Figure18:	https://www.proteinatlas.org/ENSG00000073282-TP63/pathology/prostate+cancer#img show the expression in the nuclei of basal regenerative cells of epithelial tissue	35
Figure 19:	upper: myc+, pH6, 1:10→ we did not observe the nuclear staining in basal cells	35
Figure 20:	myc+ pH9, 1:200 → the PTEN expression is clearly seen around the epithelial nuclei	36
Figure21:	https://www.proteinatlas.org/ENSG00000171862-PTEN/pathology/prostate+cancer#img show low PTEN abundancy in epithelial cells spacing the nuclei	36
Figure 22:	In ERG positive mice ERG seems to associate the blood vessel within the stroma seen in light red	37
Figure23:	https://www.proteinatlas.org/ENSG00000157554-ERG/pathology/prostate+cancer#img show the heterogeneous expression of ERG through the tissue	37
Figure 24:	calKK2+myc+, pH6, 1:50→ the nuclear expression can not be seen	38
Figure25:	https://www.proteinatlas.org/ENSG00000169083-AR/pathology/prostate+cancer#img show clearly the AR expression in the nucleus	38
Figure26:	https://www.proteinatlas.org/ENSG00000086205-FOLH1/pathology/prostate+cancer#img show epithelial cell expression of PSMA	39
Figure 27:	myc+, pH 6, 1:100→ the epithelial expression is clearly seen	39
Figure28:	https://www.proteinatlas.org/ENSG00000148773-MKI67/pathology/prostate+cancer#img show the specifically labelled proliferating nuclei	40
Figure 29:	Myc+, pH9, 1:500→ the proliferating nuclei can not be seen maybe due to lack of cancerous tissue	40
Figure30:	https://www.proteinatlas.org/ENSG00000173039-RELA/pathology/prostate+cancer#img show strong cytoplasmic immunoreactivity	41
Figure 31:	Myc+, pH9 1:1000→ The clearly seen difference between Dapi (dark blue) and RelA (light green), (this is a spectral scan to see the difference)	41
Figure32:	https://www.proteinatlas.org/ENSG00000117525-F3/pathology/prostate+cancer#img show highly heterogeneous expression through the tissue	42
Figure 33:	calKK2+myc+, pH6, 1:500→ we see the heterogeneous expression through the tissue	42

Figure34:	https://www.proteinatlas.org/ENSG00000242110-AMACR/pathology/prostate+cancer#img show the high abundance in carcinomas	43
Figure 35:	myc+, pH9, 1:20→ AMACR is expressed only in certain tumours, which makes it hard to get a positive control, we see high background.....	43
Figure36:	https://www.proteinatlas.org/ENSG00000109079-TNFAIP1/pathology/prostate+cancer#img show expression in cytoplasmic/ membranous tissue	44
Figure 37:	calKK2+myc+, pH6, 1:50→ we see the expression in epithelial cells as well as the nuclei	44
Figure 38:	excitation and emission spectra of Multistain 1 and 2.....	45
Figure 39:	At the top you see the whole slide scan with the DAPI channel. Then a selection of three ROIs for spectral scan capturing of a myc+ sample. All four lasers give a lambda stack with different numbers of channels. Thereby we generate 12 spectral scans for one multistain on one slide.	46
Figure 40:	ImageJ Macro Workflow with a myc+ genotype example	47
Figure 41:	All 6 molecular markers spectrally differentiated with different intensity bars in a wild-type mouse.....	48
Figure 42:	All 6 molecular markers spectrally differentiated with different intensity bars in a calKK2+ mouse	48
Figure 43:	All 6 molecular markers spectrally differentiated with different intensity bars in a myc+ mouse	49
Figure 44:	All 6 molecular marker spectrally differentiated with different intensity bars in a calKK2+myc+ mouse.....	49
Figure 45:	We see the expected higher expression of IKK2 in calKK2+ mice and the unpredictable strongly elevated expression in calKK2+myc+. Especially in calKK2+ mice we observed a strong negative correlation of IKK2 and IKK1, that can be better seen when only cre+ dots are blotted. Indicating that when IKK2 is highly expressed IKK1 expression is low and the other way around.	50
Figure 46:	RelA expression did not vary much between the genotypes and show a low correlation with IKK2.....	50
Figure 47:	TNFa expression is evenly distributed through all genotypes. The highest expression is observed in calKK2+ confirming connections of TNFa to inflammation. We see the lighty L-shaped correlation with IKK2 in calKK2+ and calKK2+myc+ genotypes, revealing a moderate correlation of TNFa with inflammation and cancer.....	51

Figure 48: IKK1 expression is as expected upregulated in calKK2+ mice, but not as high as IKK2 in calKK2+myc+ genotypes. Contrary to expectation the expression of IKK1 is higher in myc+ mice than in calKK2+myc+. IKK1 seem to have low to no correlation with RelA.....	51
Figure 49: spectral unmixed fluorescence intensities of a wildtype vs. calKK2, Myc and calKK2+myc+ genotype→ as expected myc+ mice have a clearly higher intensity bar for IKK1 and Myc. Especially in the myc+ mice we see the specific Myc stain in the nuclei compared to the others, where the fluorophore intensity is more evenly distributed. In calKK2 mice the Myc intensity bar show lower expression than in wild-type mice. The high IKK1 expression in calKK2+myc+ mice is giving first hints for a positive correlation to cancer.	52
Figure 50: There are no tremendous differences of IKK1 expression between the genotypes. Confirming the mouse model Myc expression is clearly higher in myc+ mice compared to the other genotypes. Myc expression seems to be distributed more evenly than IKK1 seen in the histograms. The correlation between the Myc and IKK1 specially in myc+ and calKK2+myc+ samples show a positive trend. This is giving evidence for the role of inflammation in cancer.	53
Figure 51: Histological features and differences between the 4 mouse lobes: A is the Anterior lobe, B the Ventral lobe, C the Dorsal lobe and D the Lateral lobe.....	54
Figure 52: Example of the annotated version as seen on the IKOSA platform	55
Figure 53: The different dorsal lobes of all 4 genotypes:	56
Figure 54: RNA expression in prostate cancer cell lines relative to RWPE a non-cancerous human prostate cell line. We see that IKK2, AR and RelA have a clearly higher expression pattern than RWPE showing the connection between cancer and inflammation. In confirmation with our multistainings we see the IKKB upregulation in PCa cells.....	57

10 List of Tables

Table 1: Primer list with Sequences and Size all primers are ordered from biomers.net	24
Table 2: Categorization for lobe annotation.....	55
Table 3: Detailed list of used Ab	1

Secondary Ab							
DaRb650	Rabbit	Donkey	Dylight 650	polyclonal	IgG	Abcam	1:500
GaC488	Goat	Chicken	Alexa 488	polyclonal	IgG	Invitrogen	1:500

Macro for stack combination

```

//Combination macro for spectral scans
//Bernhard Hochreiter 12.12.2019 v1.0
// run and then open the first of four separate images,
containing "001"

folderMode=true;

#####
###

setBatchMode(true);

print(time()+"combination macro STARTED- please wait until
finished");

if(folderMode==true){
    dir=getDirectory("Choose a Directory");
    files=getFileList(dir);
    n=0;

    for(f=0;f<files.length;f++){
        if (indexOf(files[f], "001") >= 0) {
            n++;
        }
    }
    print(time()+n+" files found");

    m=0;

    for(f=0;f<files.length;f++){
        if (indexOf(files[f], "001") >= 0) {
            open(files[f]);
            combine();
            m++;
            print(time()+m+" of "+n+" files
processed");
        }
    }
}

```

```

}
else{
    run("Open...");
    combine();
}

print(time()+"combination macro FINISHED");

#####

function combine() {

title1=getTitle();
dir=getDirectory("image");

title2=replace(title1,"001","002");
title3=replace(title1,"001","003");
title4=replace(title1,"001","004");
title=replace(title1,"001.nd2","");
titlecomb=replace(title1,"001.nd2","_combined");

x=415;
setSlice(1);
for(i=0;i<32;i++){
run("Set Label...", "label=ex405-em"+x+"-"+x+10);
x=x+10;
run("Next Slice [>]");
}
run("Stack to Images");
print(time()+"combination of: '"+title+"' finished 25%");

open(dir+title2);
x=495;
setSlice(1);
for(i=0;i<24;i++){
run("Set Label...", "label=ex488-em"+x+"-"+x+10);
x=x+10;
run("Next Slice [>]");
}
run("Stack to Images");

```

```

print(time()+"combination of: '"+title+"' finished 50%");

open(dir+title3);
x=575;
setSlice(1);
for(i=0;i<16;i++){
run("Set Label...", "label=ex561-em"+x+"-"+x+10);
x=x+10;
run("Next Slice [>]");
}
run("Stack to Images");
print(time()+"combination of: '"+title+"' finished 75%");

open(dir+title4);
x=655;
setSlice(1);
for(i=0;i<8;i++){
run("Set Label...", "label=ex640-em"+x+"-"+x+10);
x=x+10;
run("Next Slice [>]");
}
run("Stack to Images");

run("Images to Stack", "name=Stack title=[] use");

```

Macro for spectral unmixing with arrays

```

//Spectral unmixing macro Version alpha 0.2 - 29.04.2020
//created by Bernhard Hochreiter
//bernhard.hochreiter@meduniwien.ac.at

MasterArray=newArray(

//to create the Master Array, please name each channel,
followed by their respective relative (0-1) spectrum
over all channels.
//To de-activate channels, write "/" in the beginning
of their respective line
//If the number of channels is not consistent with the
used image, the macro will not work

```

```

rename(titlecomb);
print(time()+"combination of: '"+title+"' finished 100%");

saveAs("tiff",dir+titlecomb+".tif");

print(time()+"combination of: '"+title+"' saved");

close();
}

function time(){
    getDateAndTime(year, month, dayOfWeek, dayOfMonth, hour,
minute, second, msec);
    if (hour<10) {TimeString = "0";}
    else{TimeString="";}
    TimeString = TimeString+hour+":";
    if (minute<10) {TimeString = TimeString+"0";}
    TimeString = TimeString+minute+":";
    if (second<10) {TimeString = TimeString+"0";}
    TimeString = TimeString+second+" - ";
    return TimeString;
}

```

```

//Do not delete the commas further down

"DAPI",0.008,0.084,0.266,0.434,0.71,0.873,0.842,0.047,
0.906,1,0.876,0.779,0.634,0.531,0.038,0.164,0.28,0.235,0.168,
0.126,0.089,0.043,0.002,0.021,0.038,0.021,0.025,0.015,0.008,0
.008,0.005,0.004,0.001,0.01,0.018,0.01,0.008,0.004,0.005,0.00
3,0.004,0.003,0.001,0.001,0.001,0.001,0.001,0.001,0.001,0.001
,0.001,0.001,0,0,0,0,0.001,0.002,0.003,0.001,0.001,0.001,0.00
1,0.001,0.002,0.001,0,0,0,0.001,0.001,0.003,0.004,0.004,0.002
,0.002,0.001,0.002,0.001,
"RelA(405)",0.358,0.983,1,0.715,0.537,0.336,0.247,0.00
6,0.115,0.075,0.034,0.022,0.01,0.011,0.001,0.003,0.003,0.002,
0.001,0.001,0.001,0,0,0,0,0,0,0,0,0,0,0,0,0.004,0.007,0.004,0

```



```

        if (indexOf(files[f], ImageSelection) >= 0) {
            open(files[f]);
            close("\\Others");
            getDimensions(width, height, channels,
slices, frames);
            if(channels*slices*frames==nChannels){
                unmix();
                m++;
                print(time()+files[f]+"
processed");
                print(time()+m+" of "+n+" files
processed");
                close("*");
            }
            else{
                print(time()+"ERROR: '"+files[f]+" is
not compatible with the MasterArray (wrong channel count).");
                close("*");
            }
        }
        print(time()+"Spectral unmixing macro finished. Thank
you.");
        exit("Spectral unmixing macro finished. Thank you.");
    }
    else{
        getDimensions(width, height, channels, slices, frames);
        if(channels*slices*frames==nChannels){
            close("\\Others");
            waitForUser("Unmixing Macro is now starting. DO
NOT touch your computer until finished.");
            unmix();
            print(time()+"Spectral unmixing macro finished.
Thank you.");
            exit("Spectral unmixing macro finished. Thank
you.");
        }
        else{
            exit("Error: Image is not compatible with
MasterArray(wrong channel count).")
        }
    }
}

```

```

#####
#####
function unmix(){
    close("\\Others");
    getDimensions(width0, height0, channels0, slices0, frames0);
    dir=getDirectory("image");
    title0=getTitle();
    title1=replace(title0, " ", "_");
    rename(title1);

    //generate spectral identifiers
    for(i=0;i<nColors;i++){
        newImage(NameArray[i], "16-bit", 256, 256, nChannels);
        makeRectangle(64, 64, 128, 128);
        run("Add...", "value=4095 stack");
        run("Select None");
        for (j = 0; j < nChannels; j++) {
            setSlice(j+1);
            run("Multiply...",
"value="+MasterArray[i*(nChannels+1)+j+1]+" slice");
        }
    }

    titles = newArray(nImages());
    for (i=1; i<=nImages(); i++) {
        selectImage(i);
        titles[i-1] = getTitle();
    }

    run("Combine...", "stack1="+titles[1]+" stack2="+titles[2]+"
combine");

    for (i = 3; i < titles.length; i++) {
        run("Combine...", "stack1=[Combined Stacks]
stack2="+titles[i]+" combine");
    }
    run("Combine...", "stack1="+title1+" stack2=[Combined
Stacks]");

    run("Z Project...", "projection=[Max Intensity]");
    run("Concatenate...", "image1=[MAX_Combined Stacks]
image2=[Combined Stacks]");
}

```

```

rename(title0);

    //Run unmixing algorithm

getDimensions(width1, height1, channels1, slices1, frames1);
n=round(height1/256);

if(isOpen("Spectral Unmixing")==1){
    selectWindow("Spectral Unmixing");
    run("Close");
}
run("Spectral Unmixing");
selectWindow("Spectral Unmixing");
setLocation(0, 0);

for(i=0;i<n;i++){
    makeRectangle(width1-190, (i*256)+66, 124, 124);
    getStatistics(area, mean, min, max, std, histogram);
    if(mean>1){
        selectWindow("Spectral Unmixing");
        run("IJ Robot", "order=Left_Click x_point=200
y_point=50 delay=0 keypress=[]");
        selectImage(title0);
    }
}
selectWindow("Spectral Unmixing");
run("IJ Robot", "order=Left_Click x_point=200 y_point=100
delay=0 keypress=[]");

run("IJ Robot", "order=Left_Click x_point=200 y_point=100
delay=0 keypress=[]");
wait(3000);
run("IJ Robot", "order=KeyPress keypress=!");

loop=0;
timer=0;
while(loop==0){
    if(isOpen("Residuals image open-predicted
open")==true){
        loop++;
    }
    wait(1000);

        timer++;
        if(timer>timelimit){exit("unmixing process timed out
(+"timelimit+"s)");}
    }

selectWindow("Spectral Unmixing");
run("Close");

    //crop and save resulting images

selectWindow("Residuals image open-predicted open");
makeRectangle(0, 0, width0, height0);
run("Crop");
titleres=replace(title0, ".tif", "_unmixed_residuals");
saveAs("tiff", dir+titleres);

selectWindow("Stacks of Luciferases");
makeRectangle(0, 0, width0, height0);
run("Crop");
titleunmix=replace(title0, ".tif", "_unmixed");

getDimensions(width, height, channels, slices, frames);
for(i=0;i<channels*slices*frames;i++){
    setSlice(i+1);
    setMetadata("Label", NameArray[i]);
}
setSlice(1);

saveAs("tiff", dir+titleunmix);
close(title0);

}

#####
#####

function time(){
    getDateAndTime(year, month, dayOfWeek, dayOfMonth, hour,
minute, second, msec);
    if (hour<10) {TimeString = "0";}
    else{TimeString="";}
    TimeString = TimeString+hour+":";
    if (minute<10) {TimeString = TimeString+"0";}
    TimeString = TimeString+minute+":";
}

```

```

    if (second<10) {TimeString = TimeString+"0";}
    TimeString = TimeString+second+" - ";
    return TimeString;
}

```

Macro for colorization

```

title=getTitle();
run("Stack to Images");
run("Merge Channels...", "c1=Myc(650) c2=IKK1(546) c3=DAPI create");

rename(title);

run("Enhance Contrast", "saturated=0.35");
run("Next Slice [>]");
run("Enhance Contrast", "saturated=0.35");
run("Next Slice [>]");
run("Enhance Contrast", "saturated=0.35");

```

Macro for intensity analysing

```

title=getTitle();
rename("image");
n=nResults;
run("Set Measurements...", " redirect=None decimal=3");

//clear roiManager
if(roiManager("count")>0){
    roiManager("Deselect");

```

```

        roiManager("Delete");
    }

//create regions
run("Z Project...", "projection=[Average Intensity]");
rename("detectionmask");
setAutoThreshold("Default dark");
run("Threshold...");

```

```

waitForUser("adjust epithelial threshold");
run("Convert to Mask");
run("Dilate");
run("Analyze Particles...", "size=10000-Infinity add");
roiManager("Combine");
run("Clear Outside");
roiManager("Delete");
run("Select None");

//detect nuclei
selectWindow("image");
setSlice(1);
setAutoThreshold("Default dark");
run("Threshold...");
waitForUser("adjust nuclei threshold");
run("Create Selection");
roiManager("Add");
roiManager("Deselect");
roiManager("Select", 0);
roiManager("Rename", "nuclei");
run("Select None");
resetThreshold();

//add cells
selectWindow("detectionmask");
run("Create Selection");
run("Make Inverse");
roiManager("Add");
roiManager("Deselect");

```

```

roiManager("Select", 1);
roiManager("Rename", "cells");

//add cytosol
roiManager("Select", 0);
run("Make Inverse");
roiManager("Add");
roiManager("Deselect");
roiManager("Select", newArray(1,2));
roiManager("AND");
roiManager("Add");

roiManager("Deselect");
roiManager("Select", 2);
roiManager("Delete");
roiManager("Deselect");
roiManager("Select", 2);
roiManager("Rename", "cytosol");

run("Select None");
run("Watershed");
run("Analyze Particles...", "size=1000-Infinity add");
close("detectionmask");

//analyze intensities
selectWindow("image");
run("Stack to Images");

```

```

titles = newArray(nImages());
for (i=1; i<=nImages(); i++) {
    selectImage(i);
    titles[i-1] = getTitle();
}

setBatchMode(true);
for (j = 0; j < titles.length; j++) {
    selectWindow(titles[j]);

    for (i = 3; i < roiManager("count"); i++) {
        row=n+i-3;
        setResult("title", row, title);
        setResult("ROI", row, i-2);

        roiManager("Deselect");
        roiManager("Select", i);
        getStatistics(area, mean, min, max, std,
histogram);
        setResult("area", row, area);
        setResult(titles[j], row, mean);

        roiManager("Deselect");
        roiManager("Select", newArray(0,i));
        roiManager("AND");

        getStatistics(area, mean, min, max, std,
histogram);
        setResult(titles[j]+"_nuc", row, mean);

        roiManager("Deselect");
        roiManager("Select", newArray(2,i));
        roiManager("AND");
        getStatistics(area, mean, min, max, std,
histogram);
        setResult(titles[j]+"_cyt", row, mean);

    }
}

setBatchMode(false);
run("Images to Stack", "name="+title+" title=[] use");

roiManager("Show None");
roiManager("Show All");
roiManager("Deselect");
roiManager("Select", 1);

```